MID-INFRARED QUANTUM CASCADE LASERS: THEORETICAL AND EXPERIMENTAL STUDIES ON TEMPERATURE-DRIVEN SCATTERING

DISSERTATION

zur Erlangung des akademischen Grades

doctor rerum naturalium

(Dr. rer. nat.)

im Fach Physik

eingereicht an der

Mathematisch-Naturwissenschaftlichen Fakultät

der Humboldt-Universität zu Berlin

von

M. Sc. Yuri Victorovich Flores

Präsident der Humboldt-Universität zu Berlin

Prof. Dr. Jan-Hendrik Olbertz

Dekan der Mathematisch-Naturwissenschaftlichen Fakultät

Prof. Dr. Elmar Kulke

Gutachter:

1. Prof. Dr. W. Ted Masselink
2. Prof. Dr. Henning Riechert
3. Prof. Dr. Dan Botez

Tag der Dissputation: 04.06.2015

Contents

Abstract

Two decades after their invention in 1994, quantum-cascade lasers (QCLs) become increasingly important in the global infrared optoelectronics market. Photoacoustic spectroscopy, environment monitoring, hot object simulation, and free-space communication systems are selected examples of the current and potential applications of QCLs. Record optical powers as large as 14 W and power-conversion efficiencies ranging between $15-35\%$ have been reported for MIR QCLs for temperatures $80-300$ K. Further improvement of these characteristics depends not only of aspects as heat management and chip-packaging, but also on improving the active-region design to reduce several leakage channels of charge carriers. However, mechanisms through which leakage of charge carriers affects QCLs performance have not been thoroughly researched. A better understanding of the several (non-radiative) scattering mechanisms involved in carrier transport in QCLs is needed to design new structures and optimize their performance.

This work provides a realistic description of charge carriers transport in QCLs. We discuss in particular carrier leakage from QCL quantum-well confined states into higher and lower states. The two main mechanisms for non-radiative intersubband scattering in MIR QCLs are electron-longitudinal-optical-phonon scattering and interface roughness-induced scattering. We present methods for the experimental determination of the leakage current in QCLs at and above laser threshold, which allowed us to estimate the sheet distributions of conduction band states and better understand the impact of temperature activated leakage on QCLs characteristics. We found that even at temperatures low enough to neglect ELO scattering, carriers leakage due to IFR becomes significant for devices operating at high electron temperatures. Altogether, this approach offers a straightforward method to analyze and troubleshoot new QCL active region designs and optimize their performance.

Zusammenfassung

Quantenkaskadenlaser (QCLs) wurden vor gerade zwanzig Jahren erfunden und haben seitdem stetig im weltweiten Markt der optoelektronischen Bauelemente für den Infrarot an Bedeutung gewonnen. Anwendungsbeispiele für aktuelle und potenzielle Einsatzgebiete von QCLs sind photoakustische Spektroskopie, Umweltüberwachung, Simulation von heißen Körpern, und optische Freiraumdatenübertragung. Rekord optische Leistungen von 14 W und Leistungseffizienzen zwischen $15-35\%$ wurden bei mittelinfraroten QCLs für Betriebstemperaturen zwischen $80-300$ K erreicht. Die weitere Verbesserung dieser Eigenschaften hängt nicht nur von Aspekten wie Wärmemanagement und Chip-Packaging ab, sondern auch von Verbesserungen im Laserdesign zwecks der Reduzierung des Ladungsträgerleckstroms. Dennoch sind die verschiedenen Mechanismen und Komponenten des Leckstroms in Quantenkaskadenlasern leider noch nicht gründlich untersucht worden.

Die vorliegende Arbeit liefert a realistische Beschreibung des Ladungsträgertransports in QCLs. Wir beschreiben unter anderem Leckströme vom Quantentopf- in höhere Zustände und diskutieren elastische und inelastische Streumechanismen von Ladungsträgern bei mittelinfraroten QCLs. Wir illustrieren außerdem die Notwendigkeit zur Berücksichtigung der Elektronentemperatur für eine vollständigere Analyse der Ladungsträgertransporteigenschaften von Quantenkaskadenlasern. Methoden zur experimentellen Ermittlung des temperaturabhängigen Leckstroms in Quantenkaskadenlasern werden präsentiert. Unser Ansatz liefert eine Methode zur effektiven Analyse von der QCL-Leistung und Vereinfacht die Optimierung von QCL aktive Regionen.

List of symbols and abbreviations

Used symbols:

Symbol	Definition	Units	Page
a	unstrained lattice constant	Å	15
$a_{\parallel}$	substrate lattice parameter	Å	15
a_C	conduction band deformation potential	eV	17
a_V	valence band deformation potential	eV	17
α_L	electron-lattice coupling factor	$\mathrm{Kcm^2A^{-1}}$	26
α_m	mirror loss	$\mathrm{cm^{-1}}$	38
α_w	waveguide loss	$\mathrm{cm^{-1}}$	38
β	duty cycle	unitless	43
c	speed of light in vacuum	$\mathrm{cm\ s^{-1}}$	34
C_{th}	thermal conductance	$\mathrm{WK^{-1}cm^{-2}}$	43
dP/dI	differential slope efficiency	$\mathrm{WA^{-1}}$	38
$\delta\Omega/\Omega$	fractional volume change	unitless	17
$\delta U(z_l)$	conduction band offset at the interface l of a QCL structure	eV	82
δ_z	step length	Å	19
D^{2D}	two-dimensional density of states	$\mathrm{eV^{-1}cm^{-2}}$	24
Δ	average rms interface roughness height	nm	82
e	elementary charge	C	34
$e_{\parallel}$	strain component parallel to the direction of growth	unitless	16
$e_{\perp}$	strain component perpendicular to the direction of growth	unitless	16
ε	dielectric function	$\mathrm{CV^{-1}m^{-1}}$	76
ε_0	vacuum permittivity	$\mathrm{CV^{-1}m^{-1}}$	34
η_d	external differential quantum efficiency per cascade	unitless	38
η_f	facet efficiency	unitless	38
η_i	internal efficiency	unitless	38
η_{inj}	injection efficiency	unitless	38
η_t	transition efficiency	unitless	41
η_w	power efficiency	unitless	44
E	electron energy	eV	13
E_0	electric field amplitude	$\mathrm{kVcm^{-1}}$	40
E_C	conduction band potential (energy)	V (eV)	12
E_F^i	quasi Fermi level of subband i	eV	24
E_g	energy bandgap	eV	9
E_i	energy minimum of subband i	eV	19
E_{ij}	energy difference between subband minima of states i and j	meV	82

Symbol	Definition	Units	Page
E_{LO}	longitudinal-optical phonon energy	meV	79
E_{so}	split-off energy	eV	14
$\overline{E_V}$	average energy value of the three uppermost valence bands at the Γ-point	eV	17
f^{FD}	Fermi-Dirac probability function	unitless	24
$f(\vec{r})$	component of a Bloch function. It is a plane wave for a bulk semiconductor and a combination of a plane wave and an envelope function for a heterostructure.	$nm^{-3/2}$	14
g_c	modal gain coefficient	cmA^{-1}	36
2γ	radiative transition broadening	meV	34
G	laser gain	cm^{-1}	33
$G_{ij}(q_z)$	form factor for ELO interaction / electron-phonon coupling function	unitless	77
G_{th}	laser gain at threshold	cm^{-1}	58
Γ_c	confinement factor	unitless	33
$\widetilde{H}^{LO}$	ELO interaction hamiltonian	unitless	77
$\hbar$	reduced Planck constant	eVs	12
i	imaginary unit	unitless	12
I	electrical current	A	38
I_{th}	threshold current	A	44
J	current density	$kAcm^{-2}$	26
J_{leak}	leakage current density	$kAcm^{-2}$	38
J_{leak}^{IFR}	leakage current density due to IFR scattering	$kAcm^{-2}$	94
J_{leak}^{ELO}	leakage current density due to ELO scattering	$kAcm^{-2}$	94
J_{th}	threshold current density	$kAcm^{-2}$	38
J_{th}^{0}	threshold current density for zero carriers leakage	$kAcm^{-2}$	93
k	magnitude of crystal momentum vector	nm^{-1}	12
$\vec{k}$	crystal momentum vector	unitless	14
$\vec{k}_{\perp}$	plane wave propagation vector perpendicular to the direction of growth	unitless	15
k_B	Boltzmann constant	eVK^{-1}	24
λ	QCL emission wavelength	μm	30
L	length of a QCL stripe	mm	39
L_p	length of a QCL period	nm	34
Λ	interface roughness lateral size	nm	82
m_0^*	electron effective mass	$MeVc^{-2}$	13
m_e	free electron mass	$MeVc^{-2}$	12
n_{eff}	refractive index of the gain material	unitless	34
n_i	sheet concentration in subband i	cm^{-2}	25
n_p	doping density per period	cm^{-2}	30

Symbol	Definition	Units	Page
N_p	number of cascades	unitless	38
N_{ph}	steady-state number of photons	unitless	40
n_{LO}	phonon number	unitless	77
ω	QCL frequency of emitted light	s^{-1}	34
$\phi(\vec{r})$	phonon-induced potential	V	76
$\psi(\vec{r})$	electron wavefunction	$nm^{-3/2}$	12
P_{av}	average optical power	W	44
Φ	laser beam intensity	Wm^{-2}	33
Π	Poisson ratio	unitless	16
$\vec{q}$	phonon momentum vector	unitless	74
q_{ij}	magnitude of the two-dimensional vector involved in IFR scattering	nm^{-1}	82
$\vec{q}_{\perp}$	phonon momentum component perpendicular to the direction of growth	unitless	77
$\vec{q}_z$	phonon momentum component parallel to the direction of growth	cm^{-1}	77
$\vec{r}$	position vector	unitless	12
$\vec{r}_{\perp}$	position vector component perpendicular to the direction of growth	unitless	77
$\rho(q)$	normalization coefficient for phonon-induced potential	V	76
$\vec{R}$	crystal lattice vector	unitless	12
R_f	facet reflectivity	unitless	39
R_{th}	thermal resistance	KW^{-1}	49
σ	transition cross section	cm	33
S	laser stripe cross section	cm^2	43
t	time	s	12
τ_{eff}	"effective" upper laser level lifetime	ps	36
τ_{ij}	lifetime for non-radiative scattering between states i and j	ps	35
τ_{ij}^{LO}	ELO scattering time between states i and j	ps	77
τ_{ij}^{rad}	lifetime for radiative scattering between states i and j	ps	35
τ_{ph}	steady-state creation/absorption time for photons	A	39
T	heat sink temperature	K	26
T_{AR}	active region temperature	K	44
T_e	electron temperature	K	24
T_0	threshold current characteristic temperature	K	43/63
T_1	differential slope efficiency characteristic temperature	K	43/63

Symbol	Definition	Units	Page
$u(\vec{r})$	periodic function with the same periodicity as the crystal	unitless	14
U	total potential/bias	V	12/43
U_C	crystal potential	eV	12
U_S	scattering potential	eV	12
ς	non-parabolicity parameter	nm^2	13
V_{ol}	crystal volume	cm^3	76
w	width of a QCL stripe	μm	33
$\xi(z)$	envelope function	$nm^{-1/2}$	15
z	direction of epitaxial growth	nm	15
$\langle z_{32} \rangle$	dipole matrix element	nm	34

Abbreviations:

Abbreviation	Definition	Page
AR	active region	60
BH	buried-heterostructure	64
cw	continuous-wave	6
d.c.	duty cycle	62
DCXRD	double crystal X-ray diffraction	57
ELO	electron-longitudinal-optical-phonon (scattering)	76
FIR	far-infrared	3
FTIR	Fourier transform infrared spectroscopy	63
GSMBE	gas-source molecular-beam epitaxy	7/55
IFR	interface roughness	80
IR	infrared	1
LD	laser diode	1
LED	light-emitting diode	2
LO	longitudinal-optical	30
MIR	mid-infrared	3
MOVPE	metal-organic vapor-phase epitaxy	64
QCL	quantum-cascade laser	5
QW	quantum well	10
RHEED	high energy electron diffraction	55
rms	root mean square	82
RT	room temperature	6
SEM	Scanning electron microscope	60
UV	ultraviolet	1
VCSEL	vertical-cavity surface-emitting laser	3

1 Introduction

1.1 III-V compound semiconductors for optoelectronic applications

III-V compound semiconductors are obtained by combining group III elements (Al, Ga, In) with group V elements (N, P, As, Sb). The bandgap energy of III-V semiconductor compounds makes these materials suitable for applications based on interband radiative transitions. The correspondent emission energies range from the infrared (IR) to the ultraviolet (UV) region of the electromagnetic spectrum (Fig. 1.1).

III-V compound semiconductors are not found in nature; they were first postulated by Heinrich Welker in the early 1950s [1, 2]. Historically, the realization of optoelectronic devices based on these materials required the development of new theoretical and experimental methods including device modeling, epitaxial growth, and material doping. However, important milestones were continuously achieved by research groups worldwide involved in the realization of optoelectronic devices based on III-V compound semiconductors. Some of these milestones should be briefly mentioned.

Bulk growth of III-V compound gallium arsenide (GaAs) was first demonstrated in 1954 [3]. Less than ten years later, first GaAs-based laser diodes (LDs) emitting in the near infrared ($\sim 0.9\ \mu$m) were reported [4, 5, 6, 7]. The term "bandgap engineering", the ability to control the emission wavelength of an optoelectronic device using properties of quantum confinement [8], was developed, and the emission wavelength of LDs moved towards shorter values. In the following years, aluminum gallium arsenide (AlGaAs) and gallium arsenide phosphide (GaAsP)-based devices emitting visible red light were

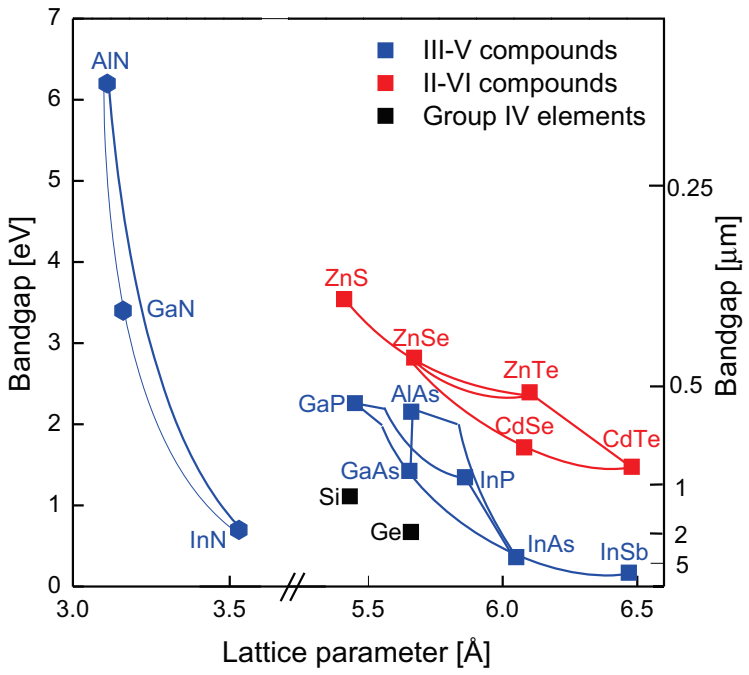

Figure 1.1: Bandgap energies for several semiconductor material compounds as a function of (unstrained) lattice parameter. Data correspond to a lattice temperature of 300 K. Group IV semiconductors are included. Solid lines represent ternary materials realized by compositions between two binaries. Squares (hexagons) represent materials crystallizing in the zincblende (wurtzite) structure. The lateral lattice parameter is considered for the three nitride materials. Data are taken from Ref. [9, 10, 11].

demonstrated [12, 13, 14, 15]. Emission of green light was achieved in GaP-based light emitting diodes (LEDs) doped with optically active impurities as oxygen (O) or nitrogen (N) [16]. By the end of the 1960s, several applications using red and green light-emitting LEDs were positioning in the market as light indicators on circuit boards and numerical displays in telephones, calculators, and watches.

In 1971, first observation of electroluminescence from gallium nitride (GaN) was reported and the possibility to realize blue light-emitting devices and color mixing applications seemed real [17]. The realization of such devices, however, required the development of suitable growth and doping methods for this particular material system. Only in the 1990s, GaN and InGaN/GaN-based devices emitting in the blue and UV regions were demonstrated [18, 19].

New concepts for nanometer-sized structures using III-V compounds as nanowires and quantum dots have been meanwhile demonstrated. Furthermore, research groups worldwide have been investigating the integration of III-V compound semiconductors with other material systems. The quantum efficiency of silicon (Si)-based solar cells, for example, has been increased above the Shockley-Queisser efficiency limit of $\sim 30\%$ using III-V compound semiconductor materials in a multi-junction device structure [20]. Another example here is the integration of III-V materials with graphene, an exciting research field which defines new potential applications for high speed electronics [21].

Today, III-V compound semiconductors play a key role in a wide spectrum of applications in modern optoelectronics industry. Selected application fields include lightning, sensing, environment monitoring, telecommunications, spectroscopy, and holography. Examples of mass-produced optoelectronic devices are LEDs, photodetectors, semiconductor laser diodes, and vertical-cavity surface-emitting lasers (VCSELs).

1.2 Laser sources for the mid- and far-infrared

Besides the visible and the UV regions of the electromagnetic spectrum, there are plenty of interesting applications for laser sources emitting in the mid- and far-infrared (MIR and FIR, respectively). Potential application fields for the FIR ($100-300\,\mu$m) are remote sensing, imaging, security screening, high-resolution spectroscopy, communications, and radioastronomy. Applications for the MIR ($3-24\,\mu$m) can be arranged in three groups: gas sensing, free-space optical communications, and hot objects simulation.

Gas sensing is the largest applications group for the MIR. Laser sources emitting in the MIR are able to target fundamental vibrational-rotational molecular absorption bands. Several gas sensing techniques using semiconductor lasers have been developed including photoacoustic spectroscopy, tunable diode laser absorption spectroscopy, laser-induced breakdown spectroscopy, and frequency comb spectroscopy. Application fields include pollution monitoring, breath analysis, atmospheric chemistry, and industrial process control [22, 23, 24, 25, 26, 27, 28].

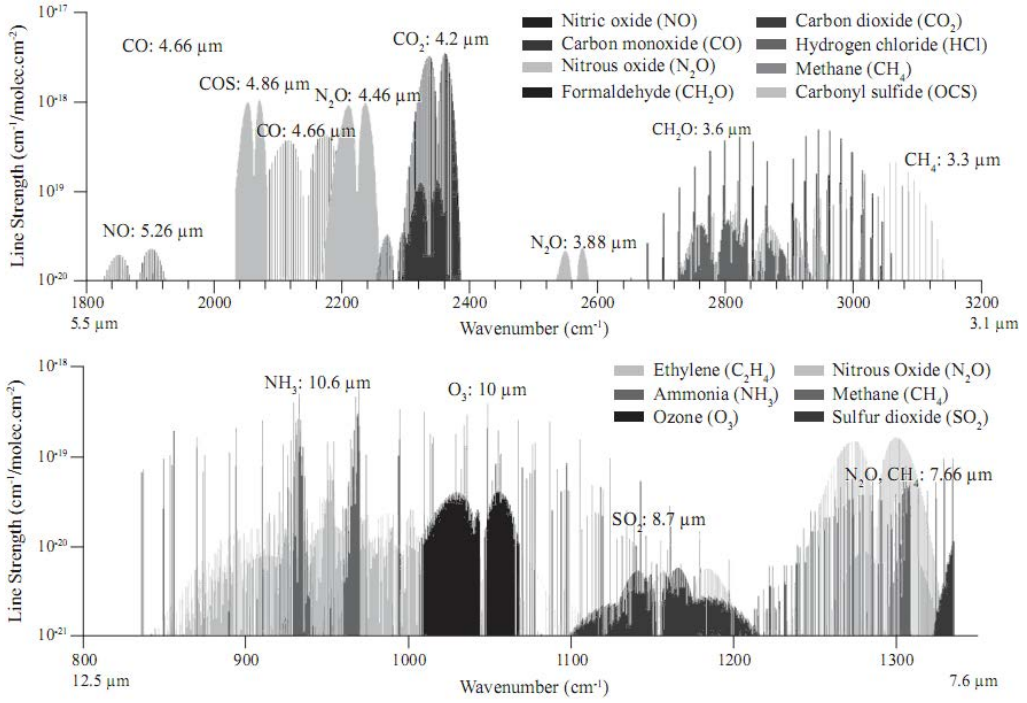

Figure 1.2: Simulated molecular absorption spectra within two MIR atmospheric transmission windows. With kind permission from John Wiley & Sons, Inc. (Ref. [27], Fig. 4.1).

Figure 1.2 shows absorption lines for several molecules in the MIR range. Some of these gases as ammonia (NH_3), nitric oxide (NO), and sulfur dioxide (SO_2) are typical and undesirable byproducts of industrial activities. Detection requirements lie typically in the order of 1 part per billion per volume (ppbv); being this even more critical in the case of hazardous chemicals like explosives, where applications are needed that detect even the smallest amount [24].

Table 1.1 summarizes available solid state laser sources for sensing and detection applications indicating the emission wavelength and typical light output power. We see from Tab. 1.1 that quantum-cascade lasers (QCLs) are unique light sources for the MIR with light output powers of the order of tens of W and showing room. State of the art terahertz (THz)-QCLs achieve tens of mW output power and operate up to a heat sink temperature of $\sim$200 K.

Another applications group for MIR lasers are free-space optical communication sys-

tems. The main idea here is to exploit the infrared transparency of the atmospheric windows between $3-5$ μm and $8-12$ μm. Intense research is motivated by potential applications as high speed internet and other communication systems. Firsts QCL-based free-space optical communication systems have been demonstrated [29, 30, 31, 32].

An additional application field of MIR laser sources is hot objects simulation. Recalling Wien's displacement law, the peak emission wavelength of a black body scales inversely with the object's surface temperature. Objects at room temperature, for example, have a peak emission wavelength at ~ 10 μm, and jet engines have peak emission wavelengths in the $2-5$ μm range. MIR laser sources are furthermore interesting for military applications: a properly designed infrared laser system could be used as a decoy to confuse an incoming heat-seeking missile, an idea known by the generic name of infrared countermeasures [31, 33]. In addition, MIR laser sources can be used to test and calibrate thermal cameras.

Despite the particular application of IR laser sources, they need to have a high degree of power efficiency. This is a major criteria, together with compactness, and low production and operation costs. Compactness and low operation costs imply also the avoidance of expensive equipment for cooling and temperature stabilization. Wavelength control and tuning is also important, then a narrow- or broadband emission spectrum is required depending on the particular application. Despite of QCLs, no other laser source offers all these characteristics in a small and compact device.

1.3 QCL research at the Humboldt University and the contribution of this work

The research group "Elementaranregungen und Transport in Festkörpern" from the Humboldt University Berlin is interested in the physics and applications of novel semiconductor heterostructures and nanostructures. An important component of the group's work is the growth and materials science of III-V heterostructures using gas-source molecular-

Laser type	**Emission wavelength**	**CW light output power**	**Temperature performance**
GaN-based LDs	UV ($0.3-0.48\ \mu$m)	tens of mW	RT-operation
AlGaAs-based LDs	NIR ($0.75-1.0\ \mu$m)	tens of mW	RT-operation
VCSELs	NIR or visible ($0.65-1.7\ \mu$m)	100 W	RT-operation
InGaAsP-based LDs	NIR ($1.2-2.0\ \mu$m)	tens of mW	RT-operation
Antimonide lasers	NIR to MIR ($2.0-4.0\ \mu$m)	<5 mW	RT-operation
QCLs	MIR ($3.0-24.0\ \mu$m)	Tens of W pulsed, hundreds of mW CW	RT-operation
Lead salt lasers	MIR ($3.0-30.0\ \mu$m)	1 mW	Cryogenic cooling required
THz QCLs	FIR ($100-300\ \mu$m)	tens of mW	Cryogenic cooling required

Table 1.1: Several solid state laser sources with the potential to be used in sensing and detection applications. "RT-operation" denotes that operation at room temperature is possible.

beam epitaxy (GSMBE).

Since 2000, a major focus of the group has been the physics and application of intersubband transitions in new strain-compensated material combinations, specially new materials and structures for QCLs. The intersubband research is currently concentrated on the optimization of high performance QCLs for the MIR, external cavity THz-QCLs including THz antireflective coatings, and growth of strain-compensated $In_xGa_{1-x}As/In_yGa_{1-y}As$ quantum well photovoltaic diodes on InP. Results are summarized in several publications[1] and in more than 15 patent disclosures, representing a total of 9 distinct inventions.

[1] For a selection see Ref. [34, 35, 36, 37, 38, 39, 40, 41, 42, 43, 44, 45, 46, 47, 48, 49, 50, 51, 52, 53, 54, 55, 56, 57, 58, 59, 60, 61, 62, 63, 64, 65, 66, 67].

In 2004, this group demonstrated a record-performance 3.8 μm-emitting QCL based on the composite barrier strain-compensated InGaAs/InAlAs-AlAs heterosystem on InP. This design approach led to a number of new active region designs [36, 44, 45, 46, 55, 57]. Strain-compensated structures incorporated large internal strains (e.g. AlAs barriers and InAs wells) into fully compensated structures and were used for the engineering of a record short wavelength (~ 3 μm emission wavelength) QCL [46].

Over the last 12 years QCL active region calculations were developed, achieving a very precise prediction of the emission wavelength. The growth process of QCLs is supported by standard characterization methods as double-crystal x-ray diffraction combined with simulation for structure analysis. The processing of laser wafers is done by means of wet chemical etching. The characterization of MIR QCLs is done in terms of current-voltage, light output power-current, beam quality, and emission wavelength over a wide temperature range ($80 - 400$ K).

The contributions of these work to QCL research are diverse. This work is primarily experimental, but with a large theoretical component. Through an analysis of rate equations at and above threshold, we proposed and demonstrated a method to quantify the effect of charge carriers leakage on QCLs performance. For this purpose we carried out quantum-mechanical calculations of how several mechanisms should influence lasers performance and compared them to experimental data.

We also investigated the impact of non-ideal interfaces within the crystal structure on the laser performance. In particular, we demonstrated the effect of rough interfaces on the QCL quantum efficiency and designed a new intersubband laser structure which takes advantage of the effect of rough interfaces in order to improve laser performance.

Finally, but not less important, we demonstrated the first continuous-wave (cw) operation of a buried-heterostructure QCL using InP:Fe regrown by GSMBE. This result is very significant, since it allows the fabrication of buried-heterostructure QCLs using active region designs with a high degree of internal strain.

Results presented in this work have been published in scientific journals including the Applied Physics Letters, the Journal of Applied Physics, and the Journal of Crystal

Growth. They were also presented in several scientific and technical meetings including, in two occasions, the "Photonics West" conference, one of the world's leading conferences for photonics and optoelectronics.

2 Quantum confinement in two-dimensional systems

In this chapter we review basic terminology related to electron states in semiconductor heterostructures. After introducing the concept of a heterostructure we discuss the Schrödinger equation for conduction band states. We further discuss the envelope function and the effective mass approximations, together with band non-parabolicity and strain-induced energy shifts to the conduction band profile. We describe furthermore the shooting method for finding envelope functions and eigenenergies and illustrate it using a single quantum well system. Finally, we review two-dimensional carrier statistics and describe the impact of increased electron temperatures on the subband distribution.

2.1 Semiconductor heterojunctions

A semiconductor heterojunction is the interface that occurs between two layers of different semiconductor materials. Opposed to a homojunction, semiconducting materials defining a heterojunction have unequal energy bandgaps. The combination of multiple semiconductor heterojunctions together in a device is called a semiconductor heterostructure. The birth of these concepts is closely related to the development of III-V semiconductor compounds and epitaxial growth technologies.

Depending on the alignment of the energy bands at the interface, semiconductor heterojunctions can be organized into three types: straddling gap (type I), staggered gap (type II), and broken gap (type III). These types are represented in Fig. 2.1. Type I heterojunctions occur when the energy bandgap E_g of one semiconductor (M2) is com-

pletely contained within the bandgap of the other one (M1) as occurs, for example, in the GaAs/AlGaAs heterosystem. In type II interfaces (e.g. InP/InSb) both the conduction band edge and the valence band edge of one material (M2) are lower than the correspondent band edges of the other material (M1). This effect is more pronounced in broken gap or type III heterojunctions, where the conduction band of one material (M2) overlaps with the valence band of the other material (M1). An example of broken gap heterojunction is the InAs/GaSb material system. For the purposes of this work we concentrate in the following only on type I heterojunctions.

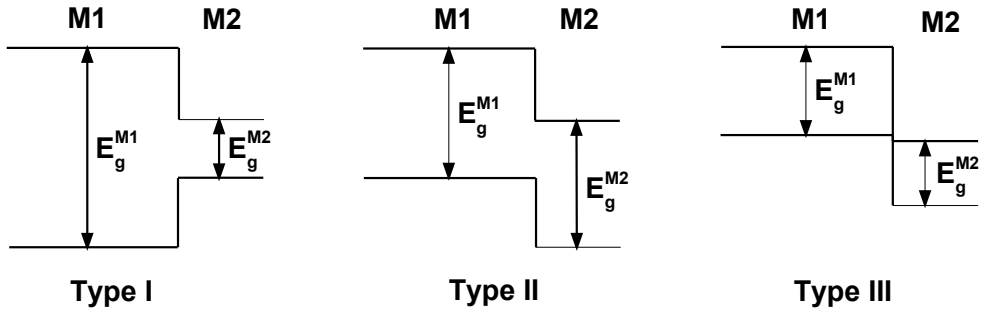

Figure 2.1: Semiconductor heterojunctions classified by band alignment.

Several heterostructure configurations can be realized sandwiching a narrow (some hundreds of meV) energy bandgap semiconductor material (M2) between two layers of a wider energy bandgap (some eV) semiconductor (M1). The most representative configurations are recollected in Fig. 2.2. If layer M2 is sufficiently thin (tens of nm), the heterostructure system is called a quantum well (QW). In this case, carriers injected into the system will occupy QW states and have a much larger spatial distribution in material M2 than in M1 (Fig. 2.2).

A stepped quantum well is realized including an alloy between materials M1 and M2. Modern epitaxial growth techniques allow also the realization of more complex structures as symmetric and asymmetric quantum well systems. Multiple quantum well systems and superlattices are realized alternating layers of materials M1 and M2.

Modern optoelectronic devices integrate different heterostructure types into one com-

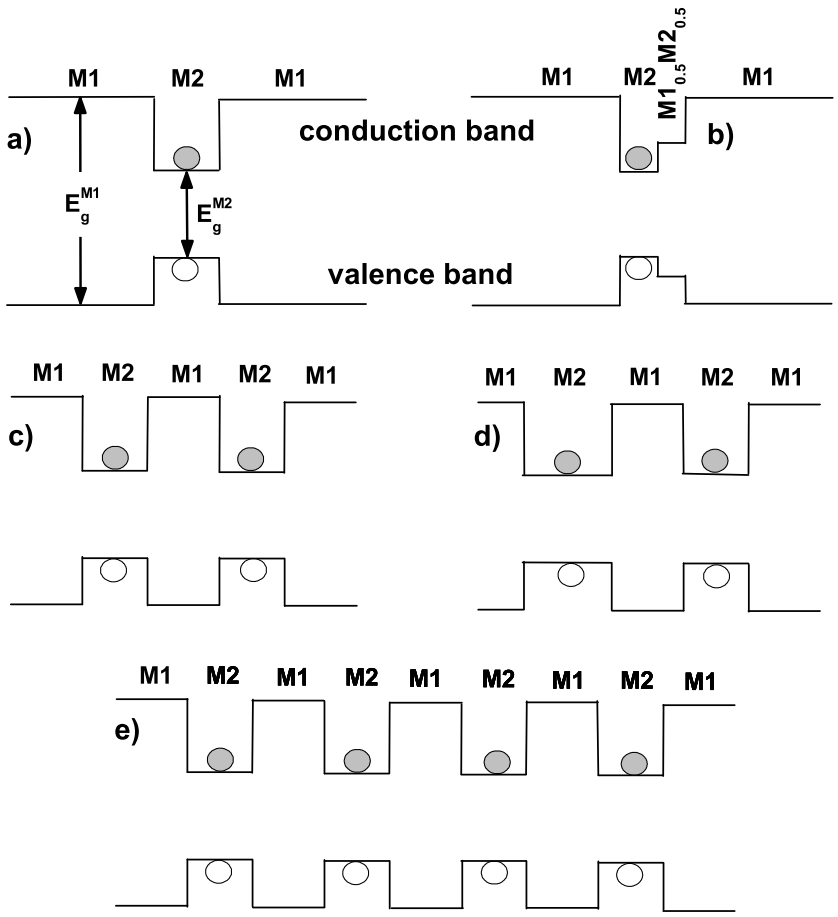

Figure 2.2: Heterostructure configurations for type I heterojunctions: single quantum well (a), stepped quantum well (b), symmetric (c) and asymmetric (d) double quantum wells, and (e) a multiple quantum well system. Solid (open) dots represent electron (hole) confined states. Based on Ref. [68].

plex structure. An example here is the quantum-cascade laser (QCL), which uses superlattices of asymmetric, single, and stepped QWs. Modern QCL structures include typically $\sim 10^3$ layers of alternating semiconductor materials.

2.2 Electron states in semiconductor heterostructures

The design and optimization of optoelectronic devices based on semiconductor heterostructures (e.g. QCLs) is possible by means of band structure engineering. This concept is inherently bounded to the early days of III-V semiconductors research and

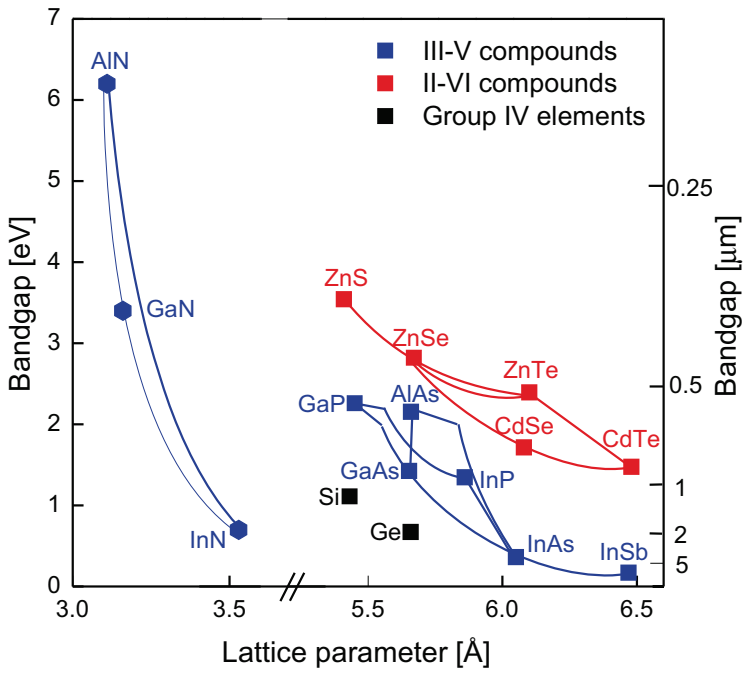

Figure 1.1: Bandgap energies for several semiconductor material compounds as a function of (unstrained) lattice parameter. Data correspond to a lattice temperature of 300 K. Group IV semiconductors are included. Solid lines represent ternary materials realized by compositions between two binaries. Squares (hexagons) represent materials crystallizing in the zincblende (wurtzite) structure. The lateral lattice parameter is considered for the three nitride materials. Data are taken from Ref. [9, 10, 11].

demonstrated [12, 13, 14, 15]. Emission of green light was achieved in GaP-based light emitting diodes (LEDs) doped with optically active impurities as oxygen (O) or nitrogen (N) [16]. By the end of the 1960s, several applications using red and green light-emitting LEDs were positioning in the market as light indicators on circuit boards and numerical displays in telephones, calculators, and watches.

In 1971, first observation of electroluminescence from gallium nitride (GaN) was reported and the possibility to realize blue light-emitting devices and color mixing applications seemed real [17]. The realization of such devices, however, required the development of suitable growth and doping methods for this particular material system. Only in the 1990s, GaN and InGaN/GaN-based devices emitting in the blue and UV regions were demonstrated [18, 19].

$$E(k) = \sum_{l=0}^{\infty} a_{2l} \cdot k^{2l} \,, \tag{2.3}$$

with real coefficients a_{2l}. The zero-order coefficient a_0 is the band minimum and is set for all practical purposes to zero. The next order of expansion results in $E(k) \sim k^2$; this approach is called the parabolic approximation. At this point we introduce the concept of the effective mass. The idea here is to allow a simple description of carriers transport in solids by replacing the electron mass by an "effective mass" which is in, in general terms, a tensor in k-space:

$$\frac{1}{m^*_{ij}} = \frac{1}{\hbar^2} \frac{\partial^2 E(k)}{\partial k_i \partial k_j} \,. \tag{2.4}$$

Often however, due to symmetry, the effective mass tensor is reduced to a longitudinal and a transverse component (e.g. Si) or even to one single parameter (e.g. GaAs).

The parabolic approximation leads to a constant effective mass. In this case, the energy function reads

$$E(k) = \frac{\hbar^2 k^2}{2m^*_0} \,, \tag{2.5}$$

which is a good approximation at low wavenumbers (Fig. 2.3).

The next expansion order of Eq. 2.3 leads to

$$E(k) = \frac{\hbar^2 k^2}{2m^*_0} \left(1 - \varsigma k^2\right) \,, \tag{2.6}$$

which is the first extension to band non-parabolicity [69]. Here, the energy function is described using two parameters: the (constant) effective mass within the parabolic approximation, m^*_0, and a material-dependent quantity ς called the non-parabolicity parameter. Applying the definition of the effective mass to Eq. 2.6 we see that m^* remains a function of the crystal momentum and, therefore, a function of energy. A characteristic result for non-parabolicity is then an energy dependent effective mass $m^*(E)$. An alternative way to describe this is using

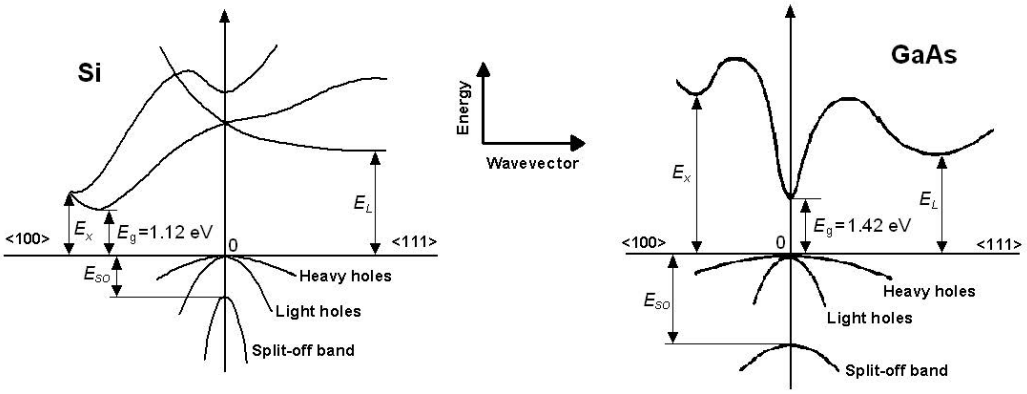

Figure 2.3: Band structures for Si (left) and GaAs (right). Parabolic-like energy dispersion regions can be recognized. The transverse effective mass for Si ($m_X^* = 0.19m_e$) is much smaller than the longitudinal effective mass ($m_L^* = 0.98m_e$). The effective mass for GaAs is $m_\Gamma^* = 0.067m_e$. Based on Ref. [70].

$$m^*(E) = m_0^*(1+\alpha\cdot E)\,, \tag{2.7}$$

where the energy E is measured from the conduction band edge, and the parameter α is given in terms of the electron mass and the energy bandgap [71, 72]:

$$\alpha = (1-m_0^*/m_e)^2/E_g\,. \tag{2.8}$$

2.2.2 Envelope function approximation

Charge carriers in a (periodic) crystal potential are described using the Bloch function

$$\psi(\vec{r}) = u(\vec{r})f(\vec{r})\,, \tag{2.9}$$

which has two components. The first one, u, is a rapidly varying function reproducing the periodicity of the crystal lattice. (For a lattice vector $\vec{R}$ we have $u(\vec{r}+\vec{R}) = u(\vec{r})$.) The second function, $f(\vec{r})$, varies only slowly within the interatomic length scale.

In bulk materials, the function $f(\vec{r})$ is a plane wave $\exp(i\vec{k}\cdot\vec{r})$ propagating within the material with a direction given by $\vec{k}$ and periodicity $2\pi/|\vec{k}|$. The plane wave can propagate

in all 3 spatial dimensions due to the crystal potential symmetry. For carriers within a semiconductor heterostructure however there is usually a confinement direction defined by the direction of epitaxial growth (z). In this case, the function $f(\vec{r})$ is written as a product of a plane wave propagating perpendicular to direction of confinement and an envelope function $\xi(z)$ parallel to this direction:

$$f(\vec{r}) = \frac{1}{\sqrt{S}} \exp(i\vec{k}_\perp \cdot \vec{r}_\perp)\xi(z) \; . \tag{2.10}$$

The term $1/\sqrt{S}$ is a normalization factor for the plane wave with propagation vector $\vec{k}_\perp = \vec{k}_x + \vec{k}_y$. Figure 2.4 illustrates the Bloch wave function decomposition for an electron in a single quantum well.

The envelope function approximation states that an analysis of the envelope function is sufficient in order to derive physical properties of charge carriers in semiconductor heterostructures. A series of arguments have been developed supporting this idea, for example by Bastard [73, 74] and Burt [75]. Although the scope and validity of the envelope function approximation approximation is still discussed, its simplification power and the advantages for heterostructure analysis are immense. This approximation is therefore very popular among device designers and researchers.

2.3 Strain-induced energy shifts

Heterostructures are usually grown over substrates which might have a similar crystallographic structure as the heterostructure yet different lattice parameters. Since the substrates are much thicker than the heterolayers, this results in an in-plane lattice parameter, which remains the same throughout the interface (pseudomorphic growth). Local strain appears, both compressive (negative strain) and tensile (positive strain). These strain components are written in terms of the substrate lattice parameter $a_\parallel$ and the (unstrained) lattice constant a of the material layer. Assuming ideal interfaces (without dislocations or impurities), the strain components parallel and perpendicular to the direction of growth

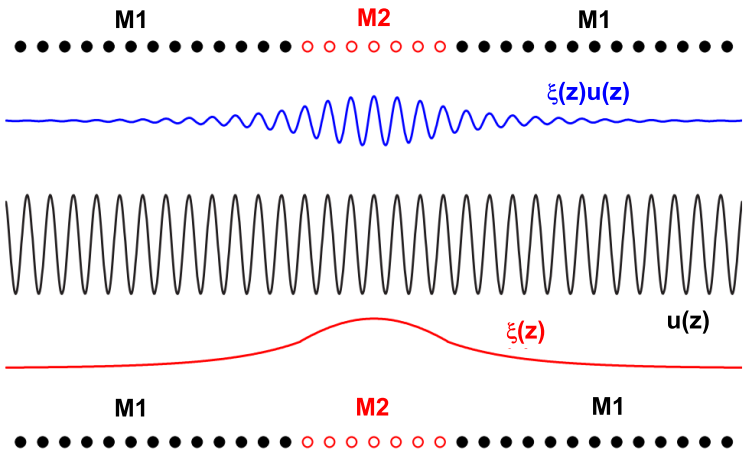

Figure 2.4: Wavefunction components for an electron in the ground state of a single quantum well. Solid (open) dots represent atom positions for the wider (narrower) bandgap material M1 (M2). $\xi(z)u(z)$ is the z-component of the total electron wavefunction. $\xi(z)$ is the envelope function in the direction of confinement. Based on Ref. [76].

are:

$$e_{\parallel} = \frac{a_{\parallel}}{a} - 1 \,, \quad e_{\perp} = -\frac{e_{\parallel}}{\Pi} \,, \tag{2.11}$$

where Π is the Poisson ratio, which depends both on the elastic stiffness constants c_{ij} and the crystallographic orientation. For the (001)-orientation, for example, we have $\Pi^{(001)} = c_{11}/(2c_{12})$.

Strain management is very important when designing QCLs, specially for applications in the MIR. Lattice matched QCL structures reduce local strains to a minimum and allow lasing action down to a wavelength of $\sim 5\ \mu$m. Shorter (up to $\sim 3\ \mu$m) wavelength QCL structures have been demonstrated using the $In_{0.73}Ga_{0.27}As$/AlAs heterosystem. Relatively large local strains of the order of $\sim 3\%$ are induced by the epitaxial growth of this heterosystem on InP, which arise from the different in-plane lattice constants. Balancing compressive with tensile strains however we are able to design strain-compensated structures, where the net stress (force per unit area due to strain) is kept at or about zero [37].

An important consequence of lattice mismatched pseudomorphic growth are correc-

tions of the order of ~ 0.1 eV to the conduction and valence band profiles. By known strain components, these corrections are nicely formulated using the model-solid theory of Van de Walle [77].

Following Van de Walle's notations, we write the corrections to the conduction and valence bands respect to a reference value, $\overline{E_V}$, which is the average energy value of the three uppermost valence bands at the Γ-point:

$$\Delta E_C = a_C \frac{\delta\Omega}{\Omega} , \tag{2.12a}$$

$$\Delta \overline{E_V} = a_V \frac{\delta\Omega}{\Omega} , \tag{2.12b}$$

where a_C (a_V) is the conduction (valence) band deformation potential. Deformations potentials represent the energy shift per unit fractional volume change $\delta\Omega/\Omega$, which is the trace of the strain tensor. For epitaxial growth on a (001) substrate we have

$$\frac{\delta\Omega}{\Omega} = \mathrm{Tr}\begin{pmatrix} e_\parallel & 0 & 0 \\ 0 & e_\parallel & 0 \\ 0 & 0 & e_\perp \end{pmatrix} = 2e_\parallel \left(1 - \frac{c_{12}}{c_{11}}\right) . \tag{2.13}$$

The strained conduction band energy in the model-solid is given by

$$E_C = \overline{E_V} + E_{so}/3 + E_g + \Delta E_C, \tag{2.14}$$

where E_{so} is the split-off energy and E_g is the energy bandgap [77]. Similar expressions are found for each component of the valence band (heavy and light holes, and the split-off band). For detailed expressions see the works of Van de Walle [77], Krijn [78], and Pollak [79]. Values for $\overline{E_V}$, a_C and a_V for specific semiconductors are calculated within the model-solid approach and are found elsewhere in the literature [10, 77].

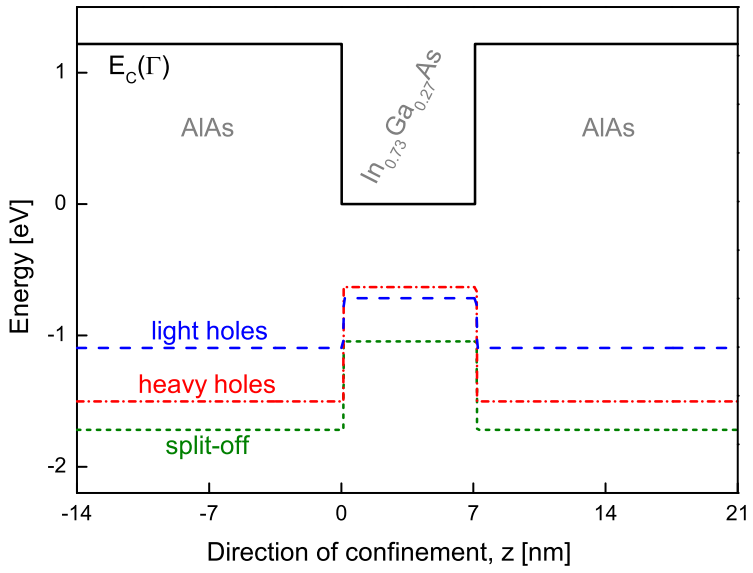

Figure 2.5: Calculated energy band profile for a 7 nm-thick $In_{0.73}Ga_{0.27}As$ quantum well surrounded by 14 nm-thick AlAs barriers. Pseudomorphic growth on InP is assumed. Local strains as large as 3.7% for $In_{0.73}Ga_{0.27}As$ and -3.2% for AlAs are calculated.

Figure 2.5 shows the resulting energy band profile for a $In_{0.73}Ga_{0.27}As$ quantum well with AlAs barriers. We assume here pseudomorphic growth on InP, resulting in compressive strain for the $In_{0.73}Ga_{0.27}As$ and tensile strain for the AlAs layers. We calculate local strains as large as 3.7% for $In_{0.73}Ga_{0.27}As$ and -3.2% for AlAs.

QCL designs using strain-compensated heterolayers can by found in Ref. [36, 37, 38, 44, 45, 46, 55, 57].

2.4 Calculation of wavefunctions and confinement energies

The Schrödinger equation (Eq. 2.1) is rewritten in a more convenient form using the effective mass and the envelope function approaches. The calculation of confinement energies and wavefunctions in heterosystems is further supported by two following considerations:

- The effective mass is written as a function of growth direction ($m^* = m^*(z)$) [80].

- Boundary conditions across a heterojunction are used [81, 82]. The most popular boundary conditions on envelope function solutions are the Ben Daniel-Duke conditions, which state that

$$\text{both} \quad \xi(z) \quad \text{and} \quad \frac{1}{m^*(z)}\frac{\partial}{\partial z}\xi(z) \quad \text{are continuous} \tag{2.15}$$

  across a heterojunction [83]. This is incorporated into our analysis of the Schrödinger equation through the kinetic energy operator, which is rewritten for this purpose as

$$-\frac{\hbar^2}{2m^*(z)}\frac{\partial^2}{\partial z^2} = -\frac{\hbar^2}{2}\frac{\partial}{\partial z}\frac{1}{m^*(z)}\frac{\partial}{\partial z}\,. \tag{2.16}$$

With these considerations the stationary Schrödinger equation for conduction band electron states in a heterosystem reads

$$\left(-\frac{\hbar^2}{2}\frac{\partial}{\partial z}\frac{1}{m^*(E_i,z)}\frac{\partial}{\partial z} + E_C(z)\right)\xi_i(z) = E_i\xi_i(z)\,, \tag{2.17}$$

where E_C is the conduction band potential including strain-induced energy shifts and externally applied potentials, and E_i (ξ_i) is the eigenenergy (envelope function) of i-th order.

Solutions to the Schrödinger equation are found numerically using the shooting method, which discretizes Eq. 2.17 and approximates iteratively the correspondent solutions (envelope functions and eigenenergies). For this purpose, we parametrize the z-coordinate through a small[1] step length δ_z, resulting in

[1] The step length is usually $\delta_z = 1\mathring{A}$. For more details on the discretization of the Schrödinger equation see for example the work of P. Harrison [68].

$$\frac{\xi_i(z+\delta_z)}{m^*(E_i,z+\delta_z)} = \xi_i(z)\left(\frac{2\delta_z^2}{\hbar^2}(E_C(z)-E_i)+\frac{1}{m^*(E_i,z+\delta_z/2)}+\frac{1}{m^*(E_i,z-\delta_z/2)}\right) - \frac{\xi_i(z-\delta_z)}{m^*(E_i,z-\delta_z/2)}\,. \tag{2.18}$$

For each quantum number i, the shooting equation 2.18 allows the reconstruction of the entire envelope function $\xi_i(z)$ in small steps of length δ_z. That means, by known ξ_i at $z-\delta_z$ and z, we calculate the value of ξ_i at $z+\delta_z$. As next, this value is used to calculate ξ_i at $z+2\delta_z$, and so, iteratively, the entire envelope function. Two initial values are however needed to start off this procedure. If the definition range of z is $z_{\min}-z_{\max}$ with $z_{\max} \gg \delta_z$, then the starting conditions

$$\xi_i(z_{\min}) = 0, \quad \xi_i(z_{\min}+\delta_z) = 1 \tag{2.19}$$

can be used.

The first expression in Eq. 2.19 states that the wavefunction extinguishes at the boundaries of the confinement potential. The second expression states that the envelope function has a finite value at $z_{\min}+\delta_z$. The exactly magnitude of ξ_i at $z_{\min}+\delta_z$ is not important due to the linear character of the Schrödinger equation. Furthermore, after the calculation of ξ_i over the definition range of z, $z_{\min}-z_{\max}$, a normalization procedure is executed in order to get normalized functions.

The iterative method described above assumes a known eigenenergy E_i for each quantum number i. This energy is however unknown and needs also to be determined. For this purpose, the shooting method usually starts using an arbitrary (some meV) value for E_i. Then, the optimal value (up to some level of accuracy) for E_i is found evaluating if $\xi(E_i, z_{\max}) = 0$. Again, this condition states that the wavefunction should extinguish at the boundary of the confinement potential. If this condition is not fulfilled, a new value of E_i is generated and a new function $\xi_i(z)$ is calculated. Finding the root of $\xi_i(E_i, z_{\max})$ with respect to E_i is further accelerated generating E_i values using the Newton-Raphson

method [84, 85].

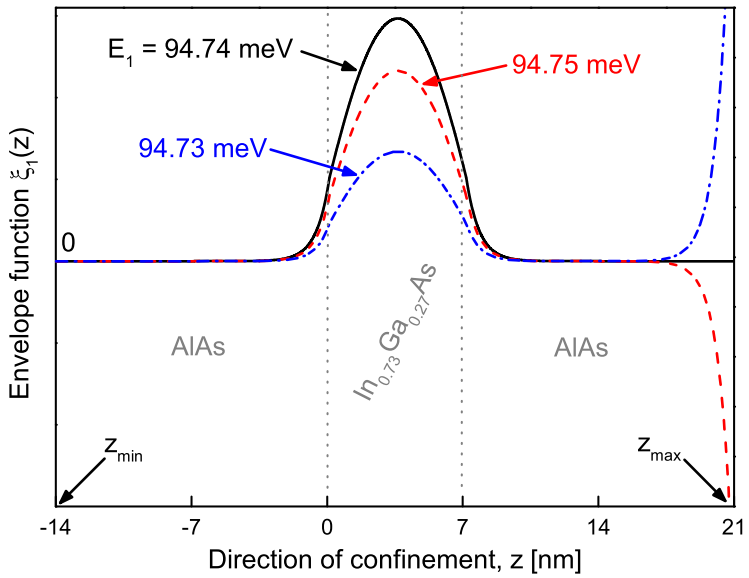

Figure 2.6: Calculated solutions $\xi_1(z)$ for the electron ground state of a 7 nm-thick $In_{0.73}Ga_{0.27}As$ quantum well surrounded by 14 nm-thick AlAs barriers. The solid line represents the optimal solution for the eigenenergy of $E_1 = 94.74$ meV. Deviations from this value lead to divergent values of ξ_1 at the boundary z_{max}. Energies are given relative to the conduction band edge of $In_{0.73}Ga_{0.27}As$.

Figure 2.6 illustrates the process of finding optimal eigenenergies. We represent here a single quantum well consisting on a thin $In_{0.73}Ga_{0.27}As$ layer sandwiched between two wide layers of AlAs. We assume pseudomorphic growth on InP. Application of the shooting method to find the ground state solution for a conduction band electron leads to the characteristic shape represented by the solid line in Fig. 2.6. The correspondent eigenenergy is calculated to $E_1 = 94.74$ meV. Small deviations from this value lead to divergent values of ξ_1 at the boundary $z_{max} = 21$ nm. The correct eigenenergy lies between values for E_1, at which $\xi_1(z_{max})$ changes its sign.

Figure 2.7 shows calculated envelope functions squared for the single quantum well (QW) of Fig. 2.5. For graphical representation purposes, we shift the $|\xi_i(z)|^2$ values in the energy axis up to the correspondent eigenenergy E_i. We see that the shape of the envelope functions squared is similar to analytic solutions for electron states confined in

an infinitely deep QW, which have the form $\sin^2(\pi iz/l_w)$ with l_w the well width.

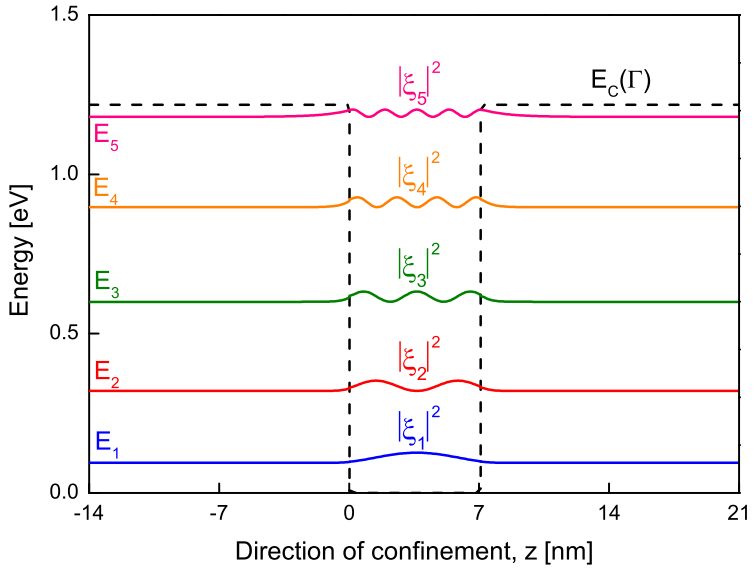

Figure 2.7: Calculated conduction band solutions for the quantum well system of Fig. 2.5.

Figure 2.8a illustrates the effect of varying the quantum well width. The confinement energies are pushed down (up) as the QW becomes wider (narrower). These calculations take into consideration strain-induced energy shifts as well as band non-parabolicity. Neglection of band non-parabolicity would led to an energy shift of the order of few tens of meV (Fig. 2.8b).

The accurate calculation of envelope functions and confinement energies for electrons in semiconductor heterostructures in very important for an effective device design process. Consider for example the active region of QCLs, which includes superlattices and multiple quantum wells. The correct calculation of energy levels is here, for example, crucial for the accurate prediction of the emission wavelength. Finally, envelope functions and confinement energies play an important role in several (radiative and non-radiative) scattering mechanisms of charge carriers in semiconductor heterostructures (chapter 5).

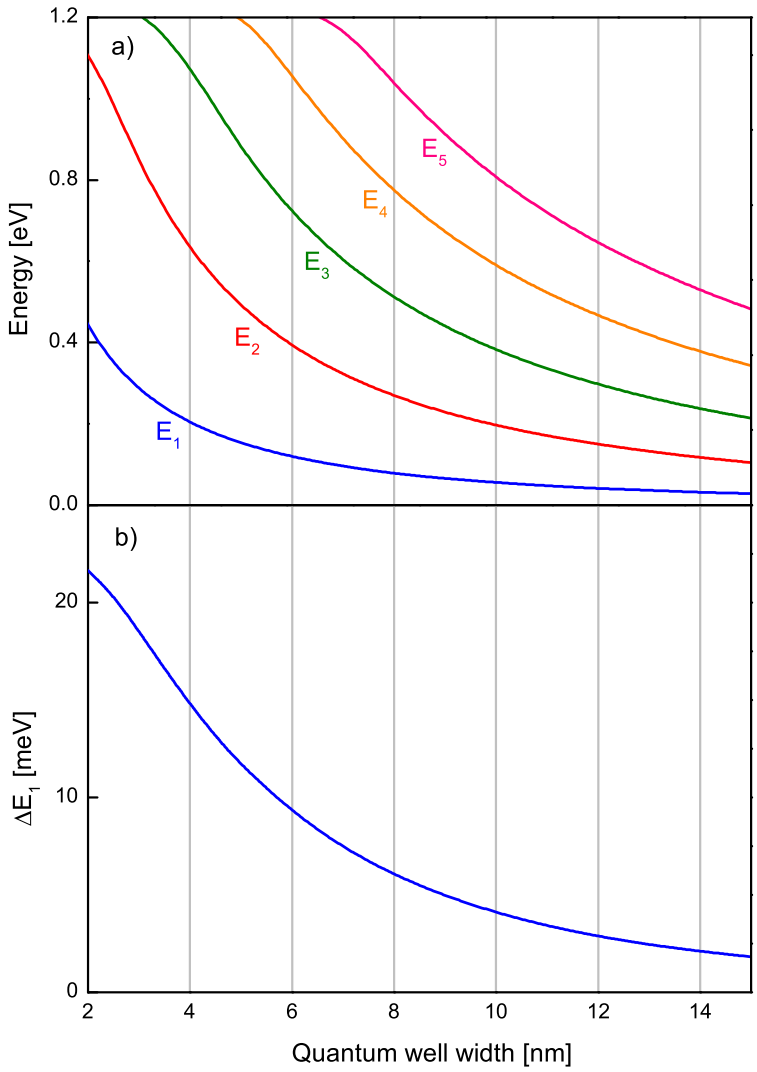

Figure 2.8: Calculated eigenenergies for the quantum well system of Fig. 2.7 as a function of well width (a). The lower panel (b) shows the calculated energy shift for the ground state eigenenergy when neglecting band non-parabolicity. $\Delta E_1 = E_1(\text{with non-parabolicity}) - E_1(\text{without non-parabolicity})$.

2.5 Carrier statistics and hot electrons

Confined electron states in semiconductor heterostructures are characterized by a quantization of the wavevector $\vec{k}$ in the direction of confinement (z) and a free electron-like dispersion for the components of $\vec{k}$ perpendicular to the heterolayers. Each of these subbands is characterized by an energy minimum E_i and by a constant density of states

$D^{2D} = m^*/\pi\hbar^2$. The total density of states at any particular energy E is the sum over all subbands up to that energy:

$$D^{2D}(E) = \sum_{i=1} \frac{m^*}{\pi\hbar^2}\Theta(E - E_i) \,, \tag{2.20}$$

with Θ the Heaviside step function [86].

Figure 2.9 shows D^{2D} for the single quantum well of Fig. 2.7. The shape of $D^{2D}(E)$ approximates roughly the form $\sqrt{E}$. This approximation becomes better when states are energetically more closer to each other, as in the case of a very wide quantum well (Fig. 2.8a). This effect corresponds namely to the transition from a two-dimensional into a three-dimensional system, where the density of states is proportional to $\sqrt{E}$.

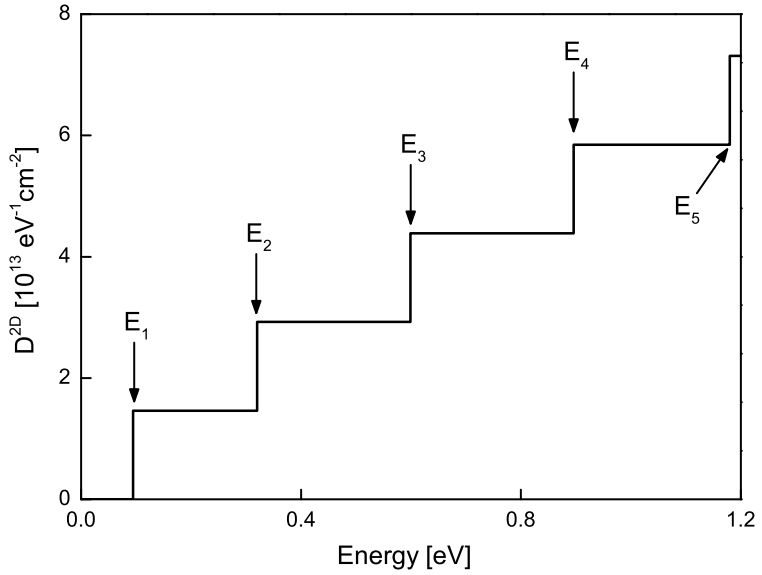

Figure 2.9: Calculated two-dimensional density of states as a function of energy for the single quantum well of Fig. 2.7.

The total electron concentration within a subband depends on the density of states D^{2D} and on the subband occupation probability. The later is given by the Fermi-Dirac probability function

$$f_i^{\mathrm{FD}}(E, T_e) = \frac{1}{\exp\left(\frac{E - E_F^i}{k_B T_e}\right) + 1} \,, \tag{2.21}$$

where E_F^i is the subband quasi Fermi level, T_e is the electron temperature, and k_B is the Boltzmann constant[2].

The quasi Fermi level E_F^i is determined by the total sheet concentration n_i through

$$n_i = \int_{E_i}^{\infty} f_i^{\mathrm{FD}}(E, T_e) D^{2D} \, \mathrm{d}E \; . \tag{2.22}$$

Figure 2.10 illustrates the effect of varying the sheet density and the electron temperature on the probability function f_i^{FD}. We consider here the ground state of Fig. 2.7. The chosen sheet densities are typical values for conduction band states in QCLs. We see that as the electron temperature increases the distribution function spreads in energy, which is a consequence of the reduction of E_F^1. Similarly, the increased occupation probabilities with increased values of n_1 results from the increased E_F^1.

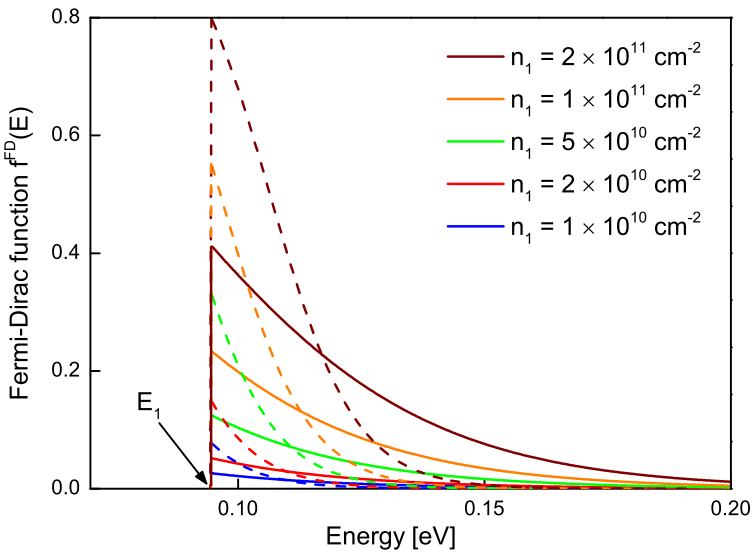

Figure 2.10: Calculated occupation probability for the ground state of Fig. 2.7 as a function of energy. Colors distinguish between different sheet concentrations. Solid (dashed) lines correspond to an electron temperature of 300 K (100 K).

Note that we describe the carriers distribution within a subband by a temperature, the electron temperature, which is larger than the lattice (or heat sink) temperature. This is the reason why those carriers are usually called "hot electrons" [87]. The relation

[2]For a simplified analysis we assume here equal electron temperatures for all subbands [88].

between electron T_e and lattice T temperatures is given by the phenomenological formula

$$T_e = T + \alpha_L J \,, \tag{2.23}$$

where J is the current density injected to the device and the proportionality factor α_L is called the electron-lattice coupling constant. This simple formula was derived from optical emission spectroscopy experiments [87] and has proven to be very useful for QCL analysis [59, 89, 90, 91, 92]. The factor α_L is material dependent and is derived from experiments; for InGaAs/InAlAs QCLs, for example, it has the value of $\alpha_L = 34.8$ Kcm^2/kA [91].

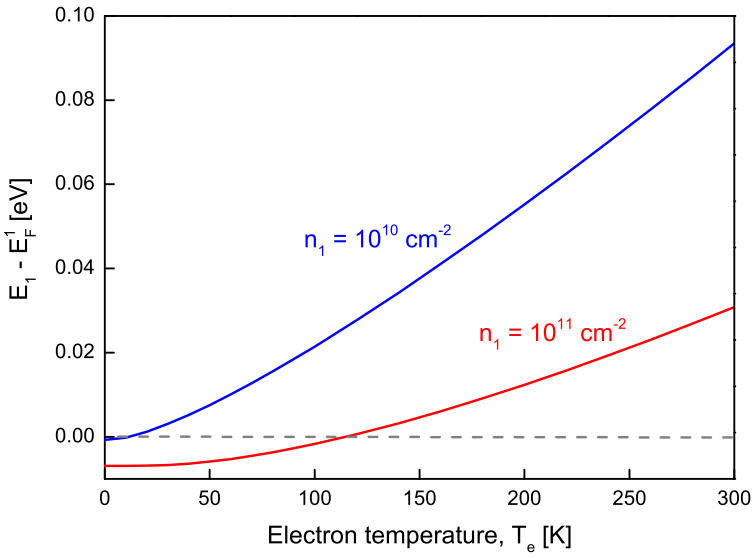

Figure 2.11: Calculated difference between the subband minimum and the quasi Fermi energy for the ground state of Fig. 2.7 as a function of electron temperature. Different colors correspond to different sheet densities. The horizontal line separates the region where E_F^1 lies above E_1 from the region where it lies below E_1.

Figure 2.11 shows the electron temperature-dependence of the quasi Fermi energy for the ground state of Fig. 2.7. We consider here two different sheet densities. We see here that for a given sheet density, the quasi Fermi energy decreases as the temperature increases. Figure 2.12 plots E_F^1 as a function of n_1 for two different values of T_e. We see here the increase of E_F^1 with increased sheet density.

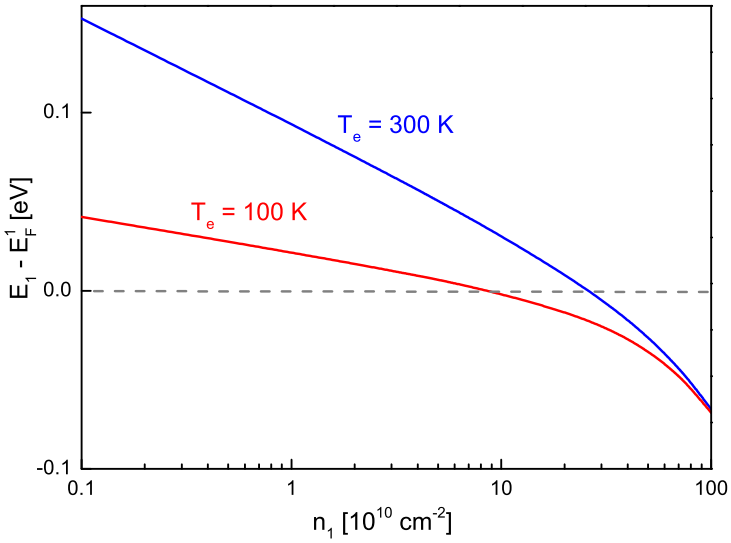

Figure 2.12: Calculated difference between the subband minimum and the quasi Fermi energy for the ground state of Fig. 2.7 as a function of sheet density. Different colors correspond to different electron temperatures. The horizontal line separates the region where E_F^1 lies above E_1 from the region where it lies below E_1.

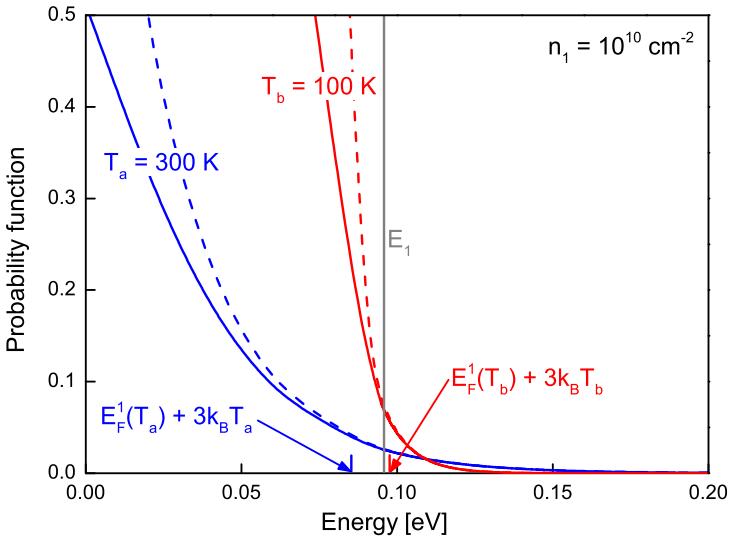

Figure 2.13: Fermi-Dirac (solid lines) and Maxwell-Boltzmann (dashed lines) occupation probability functions. The ground state of Fig. 2.7 with a sheet density of $n_1 = 10^{10}$ cm^{-2} is considered. The different colors correspond to different electron temperatures. The vertical line indicates the ground state energy E_1.

Finally, note that for typical QCL sheet densities ($10^{10} - 10^{11}$ cm^{-2}) the Fermi-Dirac probability function is well approximated by the Maxwell-Boltzmann function. Fig. 2.13 shows the Fermi-Dirac (Eq. 2.21) and the Maxwell-Boltzmann ($\exp[(E_{F,i} - E)/k_B T_e]$) functions as a function of energy for a constant sheet density and two different temperatures. We considered is here, again, the ground state of Fig. 2.7. The Maxwell-Boltzmann function approximates the Fermi-Dirac formula very well for energies $E > E_F + 3k_B T_e$. Those energy values lie usually below the subband minimum. Exceptions here occur at very low electron temperatures (< 100 K) and/or for very high sheet densities ($> 10^{12}$ cm^{-2}).

2.6 Summary

The understanding and management of quantum confinement in semiconductor heterostructures is a key issue for the design and optimization of QCLs. Solving the Schrödinger equation is supported by the envelope function and the effective mass approximations. The inclusion of band non-parabolicity as well as strain-induced energy shifts is necessary in order to find accurate solutions. Envelope functions and eigenenergies are found through iterative numerical methods. Subband distributions in QCLs are fairly described using Maxwell-Boltzmann statistics. Increased electron temperatures spread subband populations considerably.

3 Quantum Cascade Laser

In this chapter we start our analysis of MIR quantum-cascade lasers (QCLs). We discuss the general architecture and operation principle of QCLs, including aspects related to the engineering of the photon emission energy. We discuss the laser gain via an analysis of the rate equations, which leads to expressions for the threshold current density and the differential quantum efficiency. We analyze the impact of the injection efficiency and heat dissipation on laser performance. We present furthermore an useful modeling tool to simulate QCLs performance as a function of duty cycle.

3.1 General architecture and operation principle

The quantum-cascade laser (QCL), first realized in 1994 [93] and conceptually described already in 1971 [94], is a laser whose optical transitions occur between different subbands in the conduction band of a semiconductor heterostructure. Because only the conduction band is involved in this process, the laser is unipolar; further, the unipolar character allows the cascading of active regions in a straightforward manner, an ability not usually possible in p-n diode lasers.

Two-dimensional subbands in a QCL result from a spatial confinement in the direction perpendicular to the growth planes and have nearly the same $E(k)$ dependence, except that they have different constant energy offsets. This property results in a narrower spontaneous emission spectrum that from p-n diode lasers, but also much lower optical efficiency because optical phonon scattering can also scatter electrons from one subband to another without conserving k and without emitting a photon. Crucial to the operation of QCLs is how the electrons are removed from the lower laser level, transported to the next

cascade, and injected into its upper laser level. This principle of operation allows the generation of multiple photons per injected electron into the device and allows differential quantum efficiencies greater than unity.

Figure 3.1 shows a conduction band portion of a MIR QCL design using the $In_{0.73}Ga_{0.27}As/In_{0.52}Al_{0.48}As$-AlAs heterosystem. This QCL design uses tensiley strained $In_{0.52}Al_{0.48}As$ and AlAs barriers together with compressively strained $In_{0.73}Ga_{0.27}As$ layers in order to achieve a strain compensated structure. The photon emission energy is designed to 0.3 eV (emission wavelength $\lambda = 4.1$ μm). In general terms, a QCL period consists on an active region, defined by the quantum well and barriers that support upper and lower laser states, and the intermediate injector (relaxation) region. The external electric field applied to the device leads to the linear slope of the conduction band in Fig. 3.1. We include in this figure calculated moduli squared of envelope functions. Extrinsic electrons are supplied to the injector region, which is n-doped to a typical doping density per period of $n_p = 10^{11} - 10^{12}$ cm^{-2}.

Under an appropriate bias electrons tunnel from the injector region into the upper laser level (state 3 in Fig. 3.1). Ideally, these electrons will scatter down to the lower laser level (state 2 in Fig. 3.1) emitting a photon (vertical red arrows in Fig. 3.1). An electron in level 3 can scatter into states 2 or 1 through the emission of an longitudinal-optical (LO) phonon. Similarly, electrons in level 3 can scatter into higher states through LO-phonon absorption. An additional non-radiative scattering mechanism here is interface roughness-induced scattering. Typical non-radiative scattering rates lie in the ps range (see also chapter 5).

The total lifetime of level 3 is of the order of $\tau_3 \sim 1 - 3$ ps. In order to favor population inversion depopulation of the lower laser level 2 is enhanced through resonant LO-phonon emission, which means that the phonon emission rate is maximized approximating the energy E_{21} to the LO-phonon energy $E_{LO} \sim 30$ meV. This results in a short lifetime for the lower laser state of $\tau_2 \sim 0.1$ ps. With $\tau_3 > \tau_2$ we recognize the condition for population inversion and therefore for laser action. Electrons need only to be supplied fast enough into level 3 and need to exit from levels 2 and more so from level 1 into the

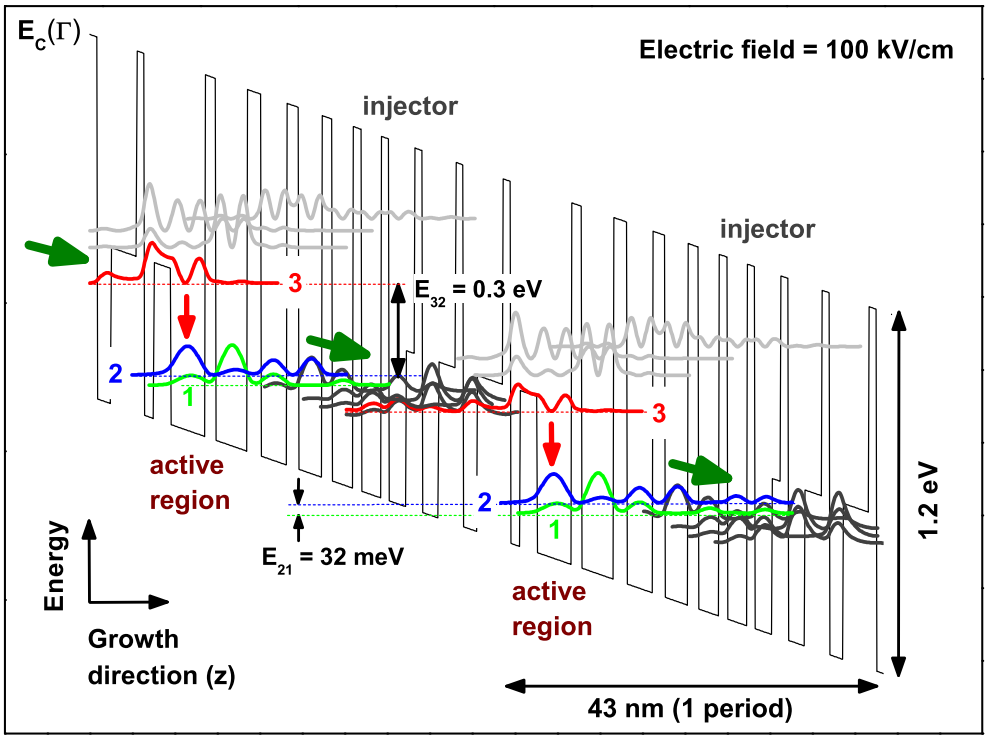

Figure 3.1: Calculated conduction band profile of a MIR QCL structure under an 100 kV/cm electric field. This structure uses $In_{0.73}Ga_{0.27}As$ for the quantum wells together with composite $In_{0.52}Al_{0.48}As$ and pure AlAs barriers. Solid lines represent the moduli-squared of relevant conduction band states. Red arrows represent radiative transitions occurring between upper (3) and lower (2) laser states, corresponding to an emission wavelength of $\lambda = 4.1$ μm. Green arrows represent carriers relaxation paths. The energy difference between levels 2 and 1, $E_{21} \sim E_{LO}$, approximates the LO-phonon energy in order to enhance depletion of state 2. Layers composition can be found in the original publication (Ref. [55]).

following downstream injector region at a high rate by tunneling. Inside the injector region, electrons relax non-radiatively into the following downstream active region. QCL structure contain typically $20-40$ periods (active and injector regions). Lasing has been demonstrated even for a single active region [95] and has been tested for as many as 200 periods [52].

After two decades of continuous development, QCLs are today the light sources of choice for a variety of applications including optical spectroscopy, gas sensing for both

medical and environmental applications, and infrared (IR) countermeasures. For all of these applications, QCLs emitting in the two atmospheric windows, 3-5 and 8-13 μm, are of special interest. In this wavelength range, peak optical powers as large as 14 W and power efficiencies ranging from 15% to 35% have been reported for a wide temperature range covering $80-300$ K [96]. Further improvement of these characteristics depends on various aspects, including heat management, chip-packaging and waveguide cladding [33, 61]. In addition, improvements of the active-region design in order to reduce several leakage channels of charge carriers is a crucial aspect to consider as well. Those aspects, i.e., the mechanisms through which leakage of charge carriers affects QCLs characteristics, however, have not been thoroughly studied. We discuss further details on QCLs charge carriers leakage in chapter 5.

To conclude we discuss some important aspects related to the engineering of the photon emission energy in MIR QCLs. The photon emission energy is the energy difference between the upper and lower laser states is determined by the details of the well and barrier widths, the effective mass describing the electrons in the heterostructure, and the relative energies of the wells and barriers. The photon emission energy is limited to the one hand to energies lower than the conduction band offset between wells and barriers and, as a closer analysis showed, to about 3/4 of this energy difference [37]. A limitation on the largest possible laser transition is scattering into the indirect valleys of the well material. In $In_{0.72}Ga_{0.28}As$ compressively strained to InP, the lowest X-valleys are about 640 meV above the Γ-valley. If the upper laser level is designed somewhat below these indirect valleys the lower laser level cannot be more than about 400 meV below the upper laser level, limiting lasers in this material to about ~ 3 μm [50]. On the other hand, the emission energy is also limited to wavelengths that lie outside of the Reststrahlband and we can consider a practical range of QCLs based on the InP substrate to be between 3 and 20 μm.

3.2 Laser gain

The laser (or propagation) gain is a quantity which characterizes the amplification that the laser beam intensity experiences as it propagates within the laser cavity. This definition is expressed by the following relation:

$$\Phi(x) = \Phi(0)\exp(Gx)\,, \tag{3.1}$$

where x is the beam propagation direction, $\Phi(x)$ is the beam intensity as a function of x, $\Phi(0)$ is a starting value, and G is the propagation gain. Based on the fact that the beam intensity within the laser cavity is directly proportional to a series of different quantities as, for example, the power density or, ultimately, the number of photons, the utility of the previous definition of the laser gain is evident as it applies to these quantities as well. Figure 3.2 shows schematically the laser beam propagation within a laser cavity.

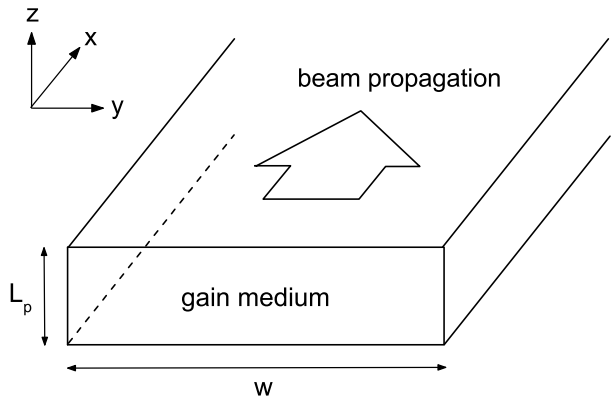

Figure 3.2: Schematic representation a laser beam propagating within a laser cavity. The beam propagation direction is $\vec{x}$.

The laser gain in QCLs is written as

$$G = \sigma\Gamma_c(n_3 - n_2)\,, \tag{3.2}$$

where σ is the transition cross section, Γ_c is the mode overlap within the active region or confinement factor (compare with Eq. 4.3), and $n_3 - n_2$ is the population inversion

between upper and lower laser states. The transition cross section σ is given by

$$\sigma = \frac{2e^2\langle z_{32}\rangle^2\omega}{\varepsilon_0 n_{\text{eff}} c(2\gamma)L_p}\,, \tag{3.3}$$

where e is the elementary charge, $\langle z_{32}\rangle$ is the dipole matrix element for the radiative transition of electrons from the upper laser level 3 into level 2, ω is the frequency of the emitted light, ε_0 is the vacuum permittivity, n_{eff} is the refractive index of the gain material, c is the speed of light in vacuum, (2γ) is the transition broadening, and L_p is the length of one QCL period. Equations 3.2 and 3.3 are obtained using Fermi's golden rule to calculate the transition probability for a radiative transition between levels 3 and 2 [74, 97, 98].

As next we write the relation between the current flowing through a QCL device and the induced laser gain. Knowing the relation between these two quantities, the device designer is able to optimize QCL structures in order to increase the general performance of devices and/or intentionally engineer some device characteristics in order to achieve specific goals. This has been recognized in the early days of QCLs development. As the group of Bell Labs published their famous paper in 1994 [93], reporting the first QCL, they suggested a three level model for describing the current dependence of the population inversion in QCLs[1]. This model has proved to be very successful for the first QCL devices which worked at helium and liquid nitrogen temperatures. However, as the QCL operating temperatures increase, several authors realize the limitations of the 3-level-approach and start to extend it in order to include temperature-driven charge carriers leakage [57, 58, 59, 92, 99, 100, 101, 102, 103].

3.2.1 Population inversion

Here we present a model to describe the population inversion in QCLs and its dependence on the current flowing through the device. This model can be used both in the low and high temperature range and it collapses under certain conditions to the standard 3-level-

[1] For a schematic representation of this model see the work of Sirtori and Teissier in Ref. [97].

approach.

Figure 3.3 shows schematically a QCL period under an appropriate bias, which is favorable for laser action. Injector-miniband states are labeled as g_i, and the upper and lower laser levels are labeled as 3 and 2, respectively. States in the excited miniband above state 3 are labeled as m_j. Solid arrows represent non-radiative scattering paths. The dashed line represents the radiative transition between states 3 and 2.

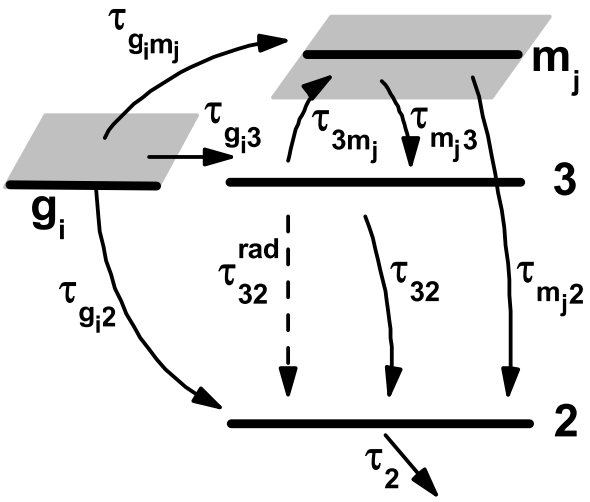

Figure 3.3: Schematic representation of a QCL period aligned under an appropriate bias. Injector-miniband states are labeled as g_i, the upper and lower laser levels are labeled as 3 and 2, respectively. States in the excited miniband above state 3 are labeled as m_j. Solid arrows represent non-radiative scattering paths. The dashed line represents the radiative transition between states 3 and 2.

Electrons in the injector miniband states g_i are injected directly into the upper laser level 3, scatter up into the excited miniband states m_j, or scatter down into the lower laser state 2. The majority of the electrons of the injector miniband are tunneled into state 3 by resonant tunneling. Nevertheless, at higher temperatures, a significant portion of these electrons are scattered up into the excited state miniband (details on this temperature-driven scattering are discussed in chapter 5).

At equilibrium, the sheet concentrations of the upper and lower laser levels are written

as:

$$n_3 = \tau_3 \left(\sum_i \frac{n_{g_i}}{\tau_{g_i 3}} + \sum_j \frac{n_{m_j}}{\tau_{m_j 3}} \right) , \tag{3.4a}$$

$$n_2 = \tau_2 \left(\sum_i \frac{n_{g_i}}{\tau_{g_i 2}} + \sum_j \frac{n_{m_j}}{\tau_{m_j 2}} + \frac{n_3}{\tau_{32}} \right) , \tag{3.4b}$$

where index i and j parametrize the states in the injector and excited miniband states, and τ_3 and τ_2 are the total lifetimes for the upper and lower laser levels. Charge carriers scattering from injector states into upper and lower laser states are considered in these equations, as well as scattering from the excited states miniband into the upper and lower laser levels.

The stimulated emission rate has been intentionally left aside in the equations above. This is expected to be a good approximation below- and at threshold, where the rate for stimulated emission is expected to be low, as typically concluded from radiative lifetime calculations [104]. Inserting Eq. 3.4a and 3.4b into Eq. 3.2, we write the laser gain G as

$$G = \sigma \Gamma_c (n_3 - n_2) = g_c \sum_i \frac{n_{g_i}}{\tau_{g_i 3}} . \tag{3.5}$$

The quantity g_c is the modal gain coefficient and is defined in

$$g_c = \sigma \Gamma_c \tau_{\text{eff}} . \tag{3.6}$$

The quantity τ_{eff} is called the "effective" lifetime of the upper laser level and is given by

$$\tau_{\text{eff}} = \tau_3 \left(1 - \frac{\tau_2}{\tau_{32}} \left[1 + \frac{\sum_j \frac{n_{m_j}}{\tau_{m_j 3}}}{\sum_i \frac{n_{g_i}}{\tau_{g_i 3}}} \right] - \frac{\tau_2}{\tau_3} \left[\frac{\sum_i \frac{n_{g_i}}{\tau_{g_i 2}} + \sum_j \frac{n_{m_j}}{\tau_{m_j 2}}}{\sum_i \frac{n_{g_i}}{\tau_{g_i 3}}} \right] \right) . \tag{3.7}$$

The denomination "effective" lifetime of the upper laser level for τ_{eff} has been used by some authors in order to describe the reduction of the upper laser level lifetime due to carriers leakage [92, 105, 106].

Consider following conditions, which are typically fulfilled in QCLs:

$$\tau_3 \gg \tau_2 \,, \tag{3.8a}$$

$$\sum_i \frac{n_{g_i}}{\tau_{g_i 3}} \gg \sum_j \frac{n_{m_j}}{\tau_{m_j 3}} \,, \tag{3.8b}$$

$$\sum_i \frac{n_{g_i}}{\tau_{g_i 3}} \gg \sum_i \frac{n_{g_i}}{\tau_{g_i 2}} + \sum_j \frac{n_{m_j}}{\tau_{m_j 2}} \,. \tag{3.8c}$$

$$\tag{3.8d}$$

Condition 3.8a is certainly satisfied due to the effective depopulation of the lower laser state, for example in devices using phonon-resonant designs [33]. Condition 3.8b is satisfied in QCLs with a high injection efficiency. In addition, the low concentration of electrons in the excited state miniband favors the fulfillment of this condition. Similarly, condition 3.8c is satisfied if considering the higher injection of electrons into level 3 compared to the injection into level 2. Altogether, considering 3.8a, 3.8b, and 3.8c, the "effective" lifetime of the upper laser level reduces to the expression:

$$\tau_{\text{eff}} \approx \tau_3 \left(1 - \tau_2/\tau_{32}\right) \,. \tag{3.9}$$

Equation 3.9 is the reduced version of Eq. 3.7. This expression (Eq. 3.9) has been successfully applied, for example to describe the wall-plug and and the quantum efficiency in QCLs [102, 105, 106]. However, it is useful to remember the general form of τ_{eff} as deviations from the reduced form may lead to some corrections in the analysis.

3.2.2 Threshold current density

At threshold, the current density J_{th} injected into the device must compensate the total (mirror and waveguide) loss as well as leakage currents. The condition for laser threshold is given by

$$\sum_i \frac{n_{g_i}}{\tau_{g_i 3}} = \underbrace{\sum_i \frac{n_{g_i}}{\tau_{g_i}}}_{J_{th}} - \underbrace{\sum_i n_{g_i} \left(\frac{1}{\tau_{g_i 2}} + \sum_j \frac{1}{\tau_{g_i m_j}} \right)}_{J_{leak}} = \frac{\alpha_m + \alpha_w}{g_c} \,. \tag{3.10}$$

The utility of this relation becomes evident as it can be used to measure the leakage current J_{leak} in QCLs, for example as a function of temperature (chapter 5). Furthermore, by known mirror loss α_m, Eq. 3.10 can be used to measure the modal gain coefficient g_c and the waveguide loss α_w [57].

An alternative way to write the threshold condition is introducing the injection efficiency

$$\eta_{inj} = \sum_i \frac{n_{g_i}}{\tau_{g_i 3}} \Big/ \sum_i \frac{n_{g_i}}{\tau_{g_i}} \,, \tag{3.11}$$

which leads to the relation:

$$J_{th} = \frac{1}{\eta_{inj}} \frac{\alpha_m + \alpha_w}{g_c} \,. \tag{3.12}$$

3.2.3 Differential quantum efficiency

The (external differential) quantum efficiency is a key quantity to characterize the performance of QCL-devices. This section discusses the parameters that play a role in the quantum efficiency, including material- and design-induced factors.

For currents somewhat above threshold, the external differential quantum efficiency per cascade, η_d, is written in terms of the differential slope efficiency dP/dI:

$$\frac{dP}{dI} = \frac{\hbar\omega}{e} N_p \eta_d \,, \quad \eta_d = \eta_f \cdot \eta_i \,, \tag{3.13}$$

where $\hbar\omega$ is photon energy of the emitted light, N_p is the number of cascades, and e is the electron charge. The external differential quantum efficiency η_d is the product of the facet efficiency η_f and the internal efficiency η_i.

The facet efficiency η_f is the fraction of the generated photons that are emitted from a facet and depends both on the waveguide loss α_w and the mirror loss α_m:

$$\eta_f = \alpha_m/(\alpha_m + \alpha_w) \; . \tag{3.14}$$

The mirror loss is calculated from the facet reflectivity R_f and the resonator length L. For a Fabry-Perót resonator with uncoated facets having each one the reflectivity R_f, the mirror loss is given by $\alpha_m = -\ln(R_f)/L$[2]; thus η_f is smaller for larger values of L (Fig. 3.4). Knowing the L-dependence of η_f one can calculate the waveguide loss α_w [107, 108].

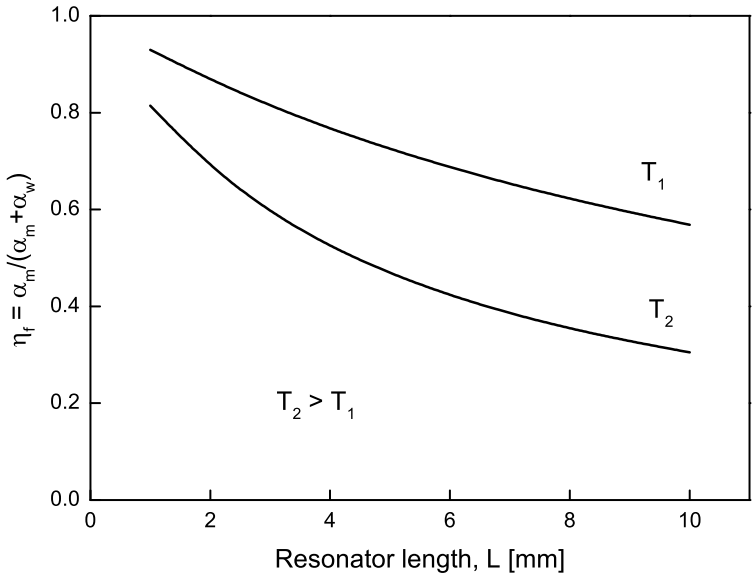

Figure 3.4: Calculated facet efficiency η_f as a function of resonator length L for a Fabry-Pérot resonator with uncoated facets each one having a reflectivity of $R_f = 0.26$. We consider for calculations typical values for the waveguide loss $\alpha_w(T_1) = 1.0$ cm^{-1} and $\alpha_w(T_2) = 3.0$ cm^{-1} for $T_1 = 80$ K and $T_2 = 300$ K, respectively.

The internal efficiency η_i gives the number of photons generated per injected electron per unit time per cascade:

$$\eta_i = \frac{1}{N_p} \frac{d(N_{ph}/\tau_{ph})}{d(I/e)} \; , \tag{3.15}$$

where N_p is the number of cascades, N_{ph} is the steady-state number of photons within the

[2]For a derivation of the expression for α_m see Eq. 4.2.

laser cavity, τ_{ph} is the steady-state creation/absorption time for photons, I is the current injected into the device, and e is the electronic charge. The quantity N_{ph}/τ_{ph} represents the steady-state rate for photons creation/absorption [106].

The particular value for η_i depends on the particular QCL design and the scattering mechanisms that charge carriers experience as they are injected into the device. Similarly as we did when deriving the gain in QCLs, an expression for η_i can be derived using the rate equations. Nonetheless, the rate equations as written in section 3.2.1 assumed that the creation/absorption rate for photons is negligible, which is an understandable assumption below- and at laser threshold. In order to derive the expression for η_i, we need to extend Eq. 3.4a and 3.4b to include stimulated emission and absorption of photons:

$$n_3 = \tau_3 \left(\sum_i \frac{n_{g_i}}{\tau_{g_i 3}} + \sum_j \frac{n_{m_j}}{\tau_{m_j 3}} - \frac{n_3}{\tau_{32}^{rad}} + \frac{n_2}{\tau_{23}^{rad}} \right) , \tag{3.16a}$$

$$n_2 = \tau_2 \left(\sum_i \frac{n_{g_i}}{\tau_{g_i 2}} + \sum_j \frac{n_{m_j}}{\tau_{m_j 2}} + n_3 \left[\frac{1}{\tau_{32}} + \frac{1}{\tau_{32}^{rad}} \right] - \frac{n_2}{\tau_{23}^{rad}} \right) , \tag{3.16b}$$

where $1/\tau_{32}^{rad}$ represents the scattering rate for stimulated emission from state 3 into 2, and $1/\tau_{23}^{rad}$ is the rate for stimulated absorption from state 2 into 3. These two rates are equal and are written in terms of the elementary charge e, the electric field amplitude E_0, the radiative dipole matrix element $\langle z_{if} \rangle$, the transition broadening γ, and the reduced Planck constant $\hbar$ as

$$\frac{1}{\tau_{32}^{rad}} = \frac{e^2 E_0^2 \langle z_{if} \rangle^2}{2\gamma\hbar} . \tag{3.17}$$

Furthermore, the steady state population of photons is given by

$$N_{ph} = \tau_{ph} \left(\frac{n_3 - n_2}{\tau_{32}^{rad}} \right) , \tag{3.18}$$

with τ_{ph} defined as in Eq. 3.15. Using Eq. 3.16a, 3.16b, and 3.18, the internal efficiency is written as a product of the injection efficiency η_{inj} (Eq. 3.11) and the transition efficiency

η_t [106]:

$$\eta_i = \eta_{inj} \cdot \eta_t \ , \tag{3.19}$$

where the transition efficiency,

$$\eta_t = \frac{\tau_{\text{eff}}}{\tau_{\text{eff}} + \tau_2} \ , \tag{3.20}$$

is given in terms of the "effective" upper laser level lifetime τ_{eff} (Eq. 3.9). The transition efficiency η_t lies in the $\eta_t = 0.6 - 0.9$ range and changes only slowly with temperature. This is because η_t depends rather on the ratio of the lifetimes of the involved states rather than on the absolute values [102].

The injection efficiency η_{inj} has then a direct impact on the quantum efficiency η_d. Smowton and Blood [109] included the injection efficiency when analyzing the differential efficiency of QW lasers and Botez *et. al.* [101, 103] proposed the inclusion of this term in the expression for η_d for QCLs. In chapter 5 we take advantage of this relation to measure the QCLs leakage current above threshold.

3.2.4 The crucial role of the injection efficiency

As next we use Eq. 3.12, 3.13 and 3.19 in order to illustrate the scaling of the differential slope efficiency dP/dI with J_{th}, the current density at threshold. The key idea here is to make use of the common dependence of these quantities on the injection efficiency η_{inj}. While dP/dI is directly proportional to η_{inj}, J_{th} is inversely proportional to this quantity (Fig. 3.5).

Considering that the injection efficiency at- and above threshold are similar, writing dP/dI as a function of J_{th} results in:

$$\frac{dP}{dI} \approx \left(N_p \frac{\hbar\omega}{e} \cdot \frac{\eta_t \alpha_m}{g_c} \right) \frac{1}{J_{th}} \approx \left(N_p \frac{(\hbar c)\varepsilon_0 n_{\text{eff}} \gamma \alpha_m L_p}{e^3 \Gamma_c \langle z_{32} \rangle^2} \cdot \frac{1/\tau_3}{1 + \frac{\tau_2}{\tau_3} - \frac{\tau_2}{\tau_{32}}} \right) \frac{1}{J_{th}} \ . \tag{3.21}$$

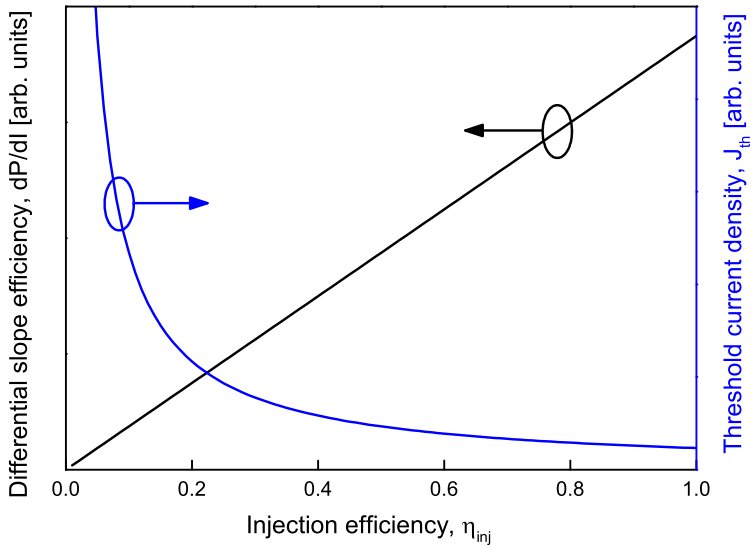

Figure 3.5: Illustrating the dependence of the differential slope efficiency and threshold current density on the injection efficiency.

Besides parameters as the emission wavelength and the laser cavity length, the scopes in Eq. 3.21 inclue quantities that lie in the same order of magnitude despite the particular QCL active region design. Considering this we reproduce dP/dI as a function of J_{th} using a set of typical parameters for short-wavelength MIR QCLs. The result is plotted in Fig. 3.6. The used parameters are indicated in this figure. We see in Fig. 3.6 that dP/dI achieves a maximum value of $(dP/dI)_{max} \sim 3.8$ W/A for $(J_{th})_{min} \sim 0.4$ kA/cm^2. This situation corresponds to an injection efficiency of unity. As η_{inj} reduces, J_{th} increases and dP/dI decreases. For $\eta_{inj} \sim 0.1$ we calculate a threshold current density of ~ 6 kA/cm^2, which corresponds to a slope efficiency of ~ 0.3 W/A.

Experimental data are also included in Fig. 3.6. Strictly speaking, each experimental point here corresponds to a different active design, and therefore it defines a unique set of scaling parameters (Eq. 3.21). Nevertheless, we recognize that the data follows the predicted trend using "typical" parameters for MIR QCLs. This fact illustrates the need of using the injection efficiency η_{inj} in the expressions for both J_{th} and dP/dI. It validates furthermore the assumption of similar η_{inj} at and (nearly) above threshold.

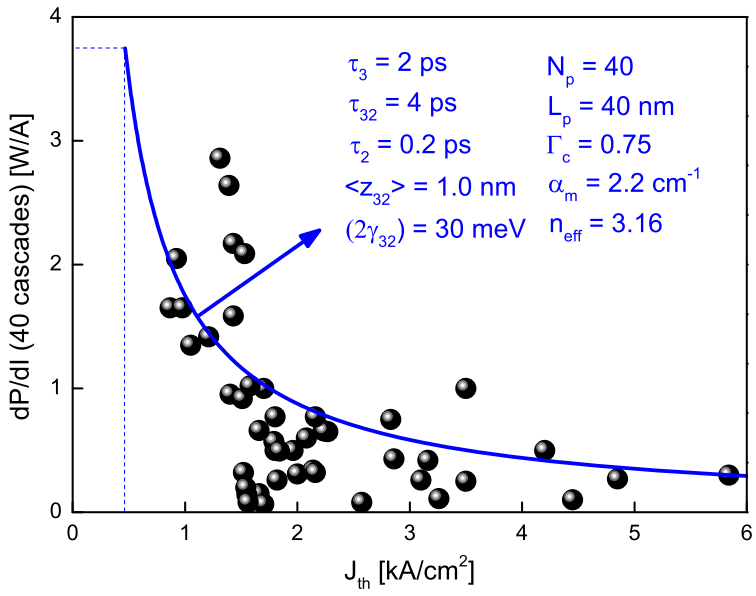

Figure 3.6: Calculated differential slope efficiency as a function of threshold current density for QCLs emitting between $3.6-5.8$ μm. Data correspond to devices grown by our research group and from Ref. [103, 110, 111, 112, 113, 114, 115, 116, 117, 118, 119, 120, 121, 122, 123, 124].

3.3 Impact of heat dissipation on the laser performance

Continuous wave (cw)-operation of QCLs depends on both extracting heat from the active region and on designing the laser to be relatively insensitive to the increased temperature of the active region. This is translated as the need of a large thermal conductance C_{th} and large characteristic temperatures T_0 and T_1[3].

Consider the increment of the active region temperature T_{AR} relative to the heat sink temperature T for a device operating in pulsed mode at a given duty cycle β:

$$T_{AR} = T + \frac{U \cdot J \cdot \beta \cdot (1-\eta_w)}{C_{th}}\,, \tag{3.22}$$

where U is the bias applied to the device, J is the injected current density, and η_w the power efficiency. The term $U \cdot J = U \cdot I/S$ with $S = Lw$ represents the electrical power per surface applied to the device. The power efficiency η_w gives the total efficiency for

[3]Details on the experimental determination of T_0 and T_1 can be found in section 4.3.

light conversion[4].

At low duty cycles, the active region temperature approximates the heat sink temperature and the temperature dependence of the J is described by the characteristic temperature T_0 and a reference value J_0 as:

$$J_{th} = J_0 \cdot \exp\left(T_{AR}/T_0\right) . \tag{3.23}$$

Using Eq. 3.23 and the analogous expression for the slope efficiency,

$$dP/dI = (\hbar\omega/e) N_p \eta_d , \quad \eta_d = \eta_d^0 \exp\left(-T_{AR}/T_1\right) , \tag{3.24}$$

we write the temperature dependence of the power efficiency η_w:

$$\eta_w = \frac{(dP/dI)(J - J_{th})}{UJ} , \tag{3.25}$$

The reciprocal dependence on temperature and on η_w of equations 3.25 and 3.22, respectively, makes evident the need of numerical methods to solve this equation system. However, typical MIR QCLs have a power efficiency ranging between $1 - 10$ %, which makes it reasonable to use the approximation $\eta_w \sim$ const. This approximation allows the investigation of several properties of QCL characteristics as a function of duty cycle in a simple but effective way. One of such characteristics is the average optical power P_{av}:

$$P_{av} = \beta \cdot (dP/dI) \cdot (I - I_{th}) , \tag{3.26}$$

which is the measured quantity in current-light output power measurements. We see from Eq. 3.23, 3.24, and 3.25, that P_{av} is directly related not only to the thermal conductance of the device, C_{th}, but also to several others material- and design-specific parameters as the photon energy $(\hbar\omega/e)$, the number of cascades N_p, and the parameters η_d^0, J_0, T_0, and T_1, which describe temperature-dependence.

The effect of temperature-driven carriers leakage is included in P_{av} principally via T_0

[4]Some authors call this term the wall-plug efficiency. This is the reason for using the index "w" in η_w.

and T_1, as these quantities are strongly affected by the injection efficiency. Large carriers leakage results in reduced values of T_0 and T_1 (chapter 5).

Figure 3.7 shows calculated values for the average optical power as a function of duty cycle for different values of T_0 and T_1. This calculation considers a MIR QCL ($\lambda = 4\,\mu$m) with $N_p = 40$ cascades, driven with $J = 1.5$ kA/cm^2 current pulses and at a constant heat sink temperature of $T = 250$ K. We assume an operation voltage of $U = 15$ V, a resonator length of $L = 4.0$ mm, a resonator width of $w = 25\,\mu$m, and a thermal conductance of $C_{th} = 100$ W/Kcm^2. The parameters $J_0 = 0.25$ kA/cm^2 and $\eta_d^0 = 0.32$ are taken, which lead to a power efficiency of $\eta_w = 2.6$ %. We use than this value to calculate the active region temperature using Eq. 3.22.

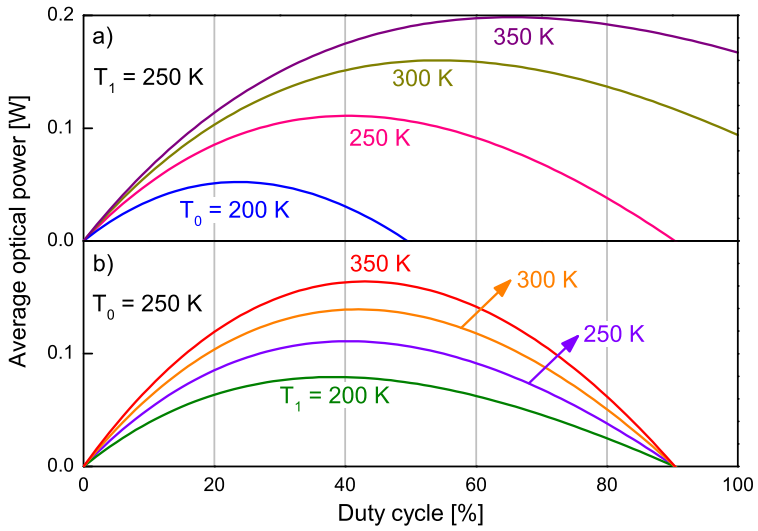

Figure 3.7: Average optical power as a function of duty cycle calculated using Eq. 3.26 for a typical MIR QCL. The upper panel (a) shows calculated values for a fixed $T_1 = 250$ K and different values of T_0. Similarly, panel (b) assumes a fixed $T_0 = 250$ K and different values for T_1. A heat sink temperature of $T = 250$ K is assumed in all cases.

Inspection of Fig. 3.7 reveals the important role of T_0 for achieving cw operation. Large values of T_0 reduce the heating of the QCL active region, maintaining leakage currents low and allowing laser operation at higher duty cycles. Similarly, larger values of T_1 ensure the achievement of larger output powers; yet not reducing the active region

temperature at threshold, which is controlled by T_0.

3.3.1 Maximum duty cycle

We investigate as next the relation between the maximum duty cycle $\beta_{\max}$ and the characteristic temperature T_0. $\beta_{\max}$ is written using Eq. 3.26, which results in [61]:

$$\beta_{\max} = \frac{C_{th} \cdot T_0 \cdot \ln(J/J_0) - T}{U \cdot J \cdot (1 - \eta_w)} \tag{3.27a}$$

$$= \frac{C_{th} \cdot T_0 \cdot \ln(J/J_0)}{U \cdot (J/J_{th}^{\text{pulse}}) J_{th}^{\text{pulse}} \cdot (1 - \eta_w)} , \tag{3.27b}$$

where $J_{th}^{\text{pulse}} = J_0 \cdot \exp(T/T_0)$ represents the low duty cycle limit ($\beta \to 0$) of the threshold current density. For a fixed injection current and heat sink temperature, Eq. 3.27b predicts a linear dependence of $\beta_{\max}$ on T_0. Furthermore, increased values of C_{th} led to a large $\beta_{\max}$ (Fig. 3.8).

Equation 3.27b allows a detailed analysis of the dependence of $\beta_{\max}$ on the injection current. For a constant ratio of J/J_{th}^{pulse}, $\beta_{\max}$ scales inversely with J. Fig. 3.9 shows the variation of $\beta_{\max}$ with increased ratio J/J_{th}^{pulse} for several values of T_0. Inspection this figure shows that $\beta_{\max}$ increases rapidly with J for current densities up to a value of approximately:

$$J_{\text{optim}} \approx 1.5 \times J_{th}^{\text{pulse}} , \tag{3.28}$$

which we call the "optimum" (or recommended) injection current density for high duty cycle operation [61]. Although operating the device at a higher current leads to some increase of $\beta_{\max}$ (Fig. 3.9), it increments also the electrical power, heating the active region and affecting negatively the performance of the device. Furthermore, no increment of $\beta_{\max}$ at all is predicted for current density values larger than the roll-over value:

$$J_{\text{rollover}} = e \times J_{th}^{\text{pulse}} , \tag{3.29}$$

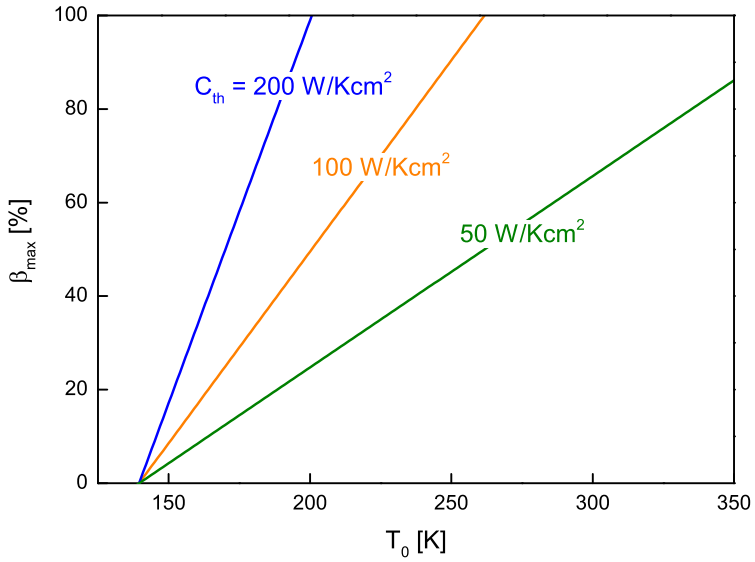

Figure 3.8: Calculated maximal duty cycle as a function of threshold current characteristic temperature T_0. Solid lines correspond to different values of C_{th} and are calculated using Eq. 3.27b. A heat sink temperature of $T = 250$ K, a constant injection current density of $J = 1.5$ kA/cm^2, and a power efficiency of $\eta_w = 0.026$ are assumed for calculations. Other parameters are $U = 15$ V and $J_0 = 0.25$ kA/cm^2.

where $e \approx 2.72$ is the Euler number. Current densities higher than J_{rollover} result in a significant heating of the active region, which leads to a decrease of the output power at higher duty cycles and, consequently, of β_{max}.

The effect of increased operation currents on the average optical power is illustrated in Fig. 3.10, which shows calculated values for the optical power as a function of duty cycle. The different lines correspond to calculated values for the optical power using equation 3.26 using different values for J/J_{th}^{pulsed}. As in our previous calculations, a heat sink temperature of $T = 250$ K is assumed. Further parameters are the same as used in Fig. 3.7.

The reduction of the maximum duty cycle for values $J > J_{\text{rollover}}$ is clearly recognized. This figure illustrates also the effect of increasing injection currents on the active region heating. As a matter of fact, an increment in current induces larger values of $\Delta T = T_{AR} - T$ for smaller duty cycles. Figure 3.10 shows also that the maximum av-

erage optical power increases with the injection current. This effect is discussed in more detail in the next section.

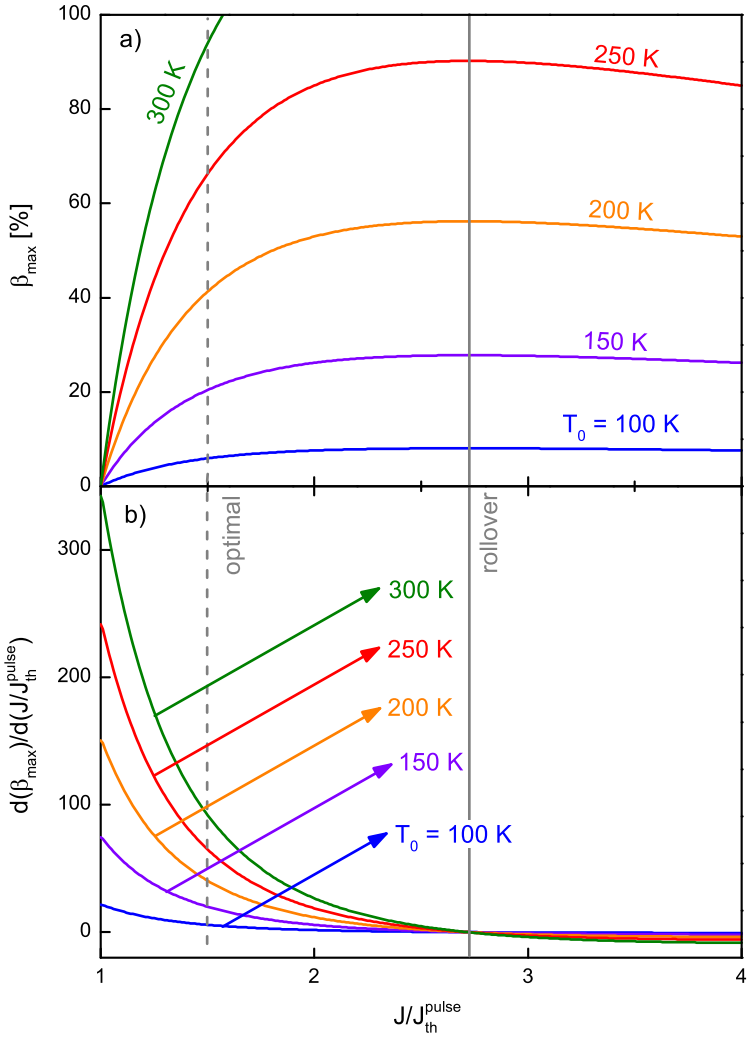

Figure 3.9: Calculated maximal duty cycle as a function of current density for different characteristic temperatures T_0 (a). A heat sink temperature of $T = 250$ K and a power efficiency of $\eta_w = 0.026$ are assumed. Other parameters are $U = 15$ V and $J_0 = 0.25$ kA/cm^2 and $C_{th} = 100$ W/Kcm^2. The lower panel (b) shows the correspondent derivative of $\beta_{\max}$ with respect to current density. The solid vertical line indicates the rollover position for $\beta_{\max}$ as given by Eq. 3.29. The dashed line serves as a guide for the eye indicating the region of the most rapid increase of $\beta_{\max}$: $1 < J \lesssim 1.5$ (Eq. 3.28).

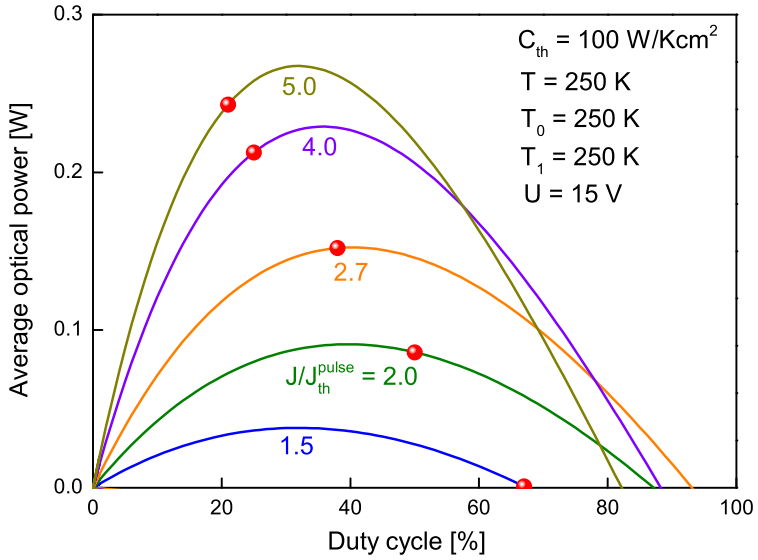

Figure 3.10: Calculated average optical power as a function of duty cycle for a MIR QCL ($\lambda = 4.0\,\mu$m). Different lines correspond to calculated values using Eq. 3.26 with different values of J/J_{th}^{pulsed}. A heat sink temperature of $T = 250$ K is assumed. Other parameters are the same as the used in Fig. 3.7; some of them are indicated. Solid dots mark the points where $\Delta T = T_{AR} - T = 100$ K.

3.3.2 Maximum average optical power

Continuing the discussion of the previous section, we explore in the following the factors driving the maximum average power of a QCL device. We have seen in Fig. 3.10 that driving the QCL device with higher currents leads to an initial increase in the average power. The maximum duty cycle reduces for ratios $J/J_{th}^{\text{pulse}} > 2.7$ (Eq. 3.29). Nevertheless, the maximum average optical power increases further, although it is achieved at lower duty cycles (Fig. 3.10).

A calculation of the maximum average power would imply to start from Eq. 3.26 and solve for the condition $\partial P_{av}/\partial\beta = 0$. This results in a transcendental equation for β, whose solution is not straightforward to find. However, it is possible to approximate the maximum average optical power as $P_{av}^{\max} \approx P_{av}(\beta_{\max}/2)$. Introducing the thermal resistance $R_{th} = 1/(C_{th} \cdot S)$, with $S = Lw$ the laser stripe cross section, this leads to [61]:

$$P_{av}^{\max} \approx P_{av}(\beta_{\max}/2) = \frac{\eta_1}{2}\left(J/J_{th}^{\text{pulse}} - \sqrt{J/J_{th}^{\text{pulse}}}\right)\left(\frac{T_0 \ln(J/J_{th}^{\text{pulse}})}{U(J/J_{th}^{\text{pulse}})R_{th}(1-\eta_w)}\right) \times \exp\left(-\frac{2T + T_0 \ln(J/J_{th}^{\text{pulse}})}{2T_1}\right). \tag{3.30}$$

This simplification becomes reasonable as one considers the nearly symmetric shape of $P_{av}(\beta)$ (Fig. 3.10). However, as the ratio J/J_{th}^{pulse} increases the symmetric shape is lost, and Eq. 3.30 becomes an inaccurate approximation of the maximum average optical power. Nevertheless, an analytical form like Eq. 3.30 allows a simplified analysis of $P_{av}^{\max}$ vs. the input parameters.

As next we study the dependence of $P_{av}^{\max}$ on the injection current J/J_{th}^{pulse} and on the characteristic temperatures T_0 and T_1. We further compare the results of using Eq. 3.30 with values obtained by numerical calculation.

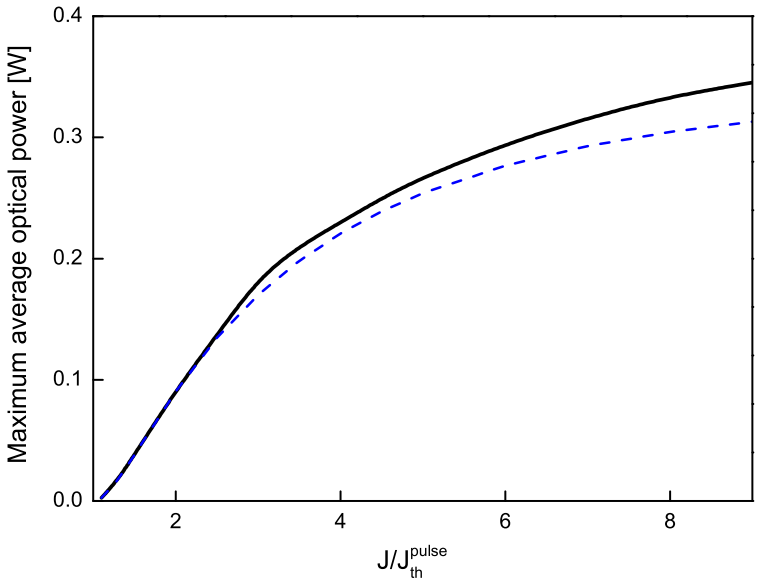

Figure 3.11: Calculated maximum average optical power as function of current density. The solid line results from a numerical analysis of Eq. 3.26. The dashed line represents calculated values using the approximation of Eq. 3.30. Following parameters are assumed: $T = 250$ K, $U = 15$ V, $J_0 = 0.25$ kA/cm^2, $\eta_1 = 2$ W/A, $T_0 = 250$ K, $T_1 = 250$ K, and $R_{th} = 10$ K/W.

Figure 3.11 shows the calculated maximum average optical optical power $P_{av}^{\max}$ as a function of injection current. The solid line shows values calculated numerically using Eq. 3.26 and the dashed line represents calculated values using the approximation of Eq. 3.30. We observe initially a rapid increase of $P_{av}^{\max}$, followed by a saturation behavior of $P_{av}^{\max}$ as a function of current. The saturation region starts at a value of $J/J_{th}^{\text{pulse}} \approx 2.7$. This value can then be considered as the recommended injection current in order to achieve high average optical power in pulsed mode[5]. Furthermore, up to the current ratio $J/J_{th}^{\text{pulse}} \approx 2.7$, very good agreement is achieved between values calculated analytically and following Eq. 3.30. This is related to the loss of symmetry in the shape of the $P_{av}(\beta)$ function, which is accelerated by a rapid active region heating beyond this point. Calculations show that this occurs when the active region temperature is increased above 100 K relative to the heat sink temperature (Fig. 3.10). The value of $\Delta T = T_{AR} - T = 100$ K can be then considered as a critical value for achieving high optical power. Currents within the range $J/J_{th}^{\text{pulse}} = 1 - 10$ are considered in Fig. 3.11, and we observe no decrease of $P_{av}^{\max}$ with increasing current. However, a decrease of $P_{av}^{\max}$ for much larger current densities is expected from the increased active region heating.

Figure 3.12a compares calculated values for the maximum average optical power $P_{av}^{\max}$ obtained numerically, and the ones calculated following Eq. 3.30, as a function of the characteristic temperature T_0. We see in this figure that good agreement between both approaches is achieved up to a ratio of $T_0/T \approx 2$. As in the case of Fig. 3.11, deviations between both approaches become more evident as the shape of the $P_{av}(\gamma)$ function loses its symmetry. Interestingly, practically no disagreement between both approaches is found when calculating $P_{av}^{\max}$ as a function of the characteristic temperature T_1 (Fig. 3.12b).

[5]Note that this value is approximately by a factor of 2 larger than the optimum current for high duty cycle operation (Eq. 3.28).

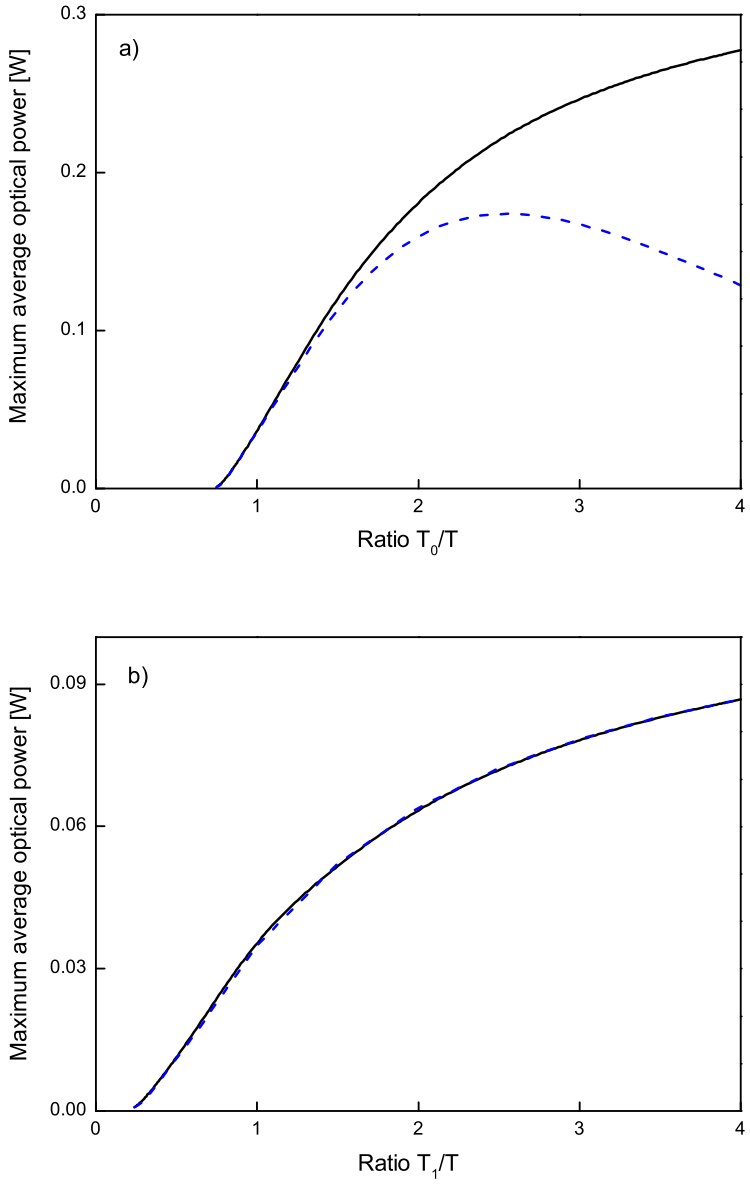

Figure 3.12: Calculated maximum average optical power as function of characteristic temperatures T_0 (a) and T_1 (b). The solid line results from a numerical analysis of Eq. 3.26. The dashed line represents calculated values using the approximation of Eq. 3.30. Following parameters are assumed: $T = 250$ K, $U = 15$ V, $J_0 = 0.25$ kA/cm^2, $\eta_1 = 2$ W/A, $J = 1$ kA/cm^2, T_1 = 250 K, and $R_{th} = 10$ K/W.

To summarize, for values up to $J/J_{th}^{\text{pulse}} \approx 2.7$, $T_0/T \approx 2$, and $T_1/T \approx 2$, the approach used in Eq. 3.30 offers values for $P_{av}^{\max}$, which are in good agreement with values obtained from a numerical analysis of Eq. 3.26. Despite of the injection current, the achievement

of high average optical power depends also on parameters as η_1, I_0, T_0, T_1, and C_{th}. Furthermore, following values are recommended for high optical power operation: $J \approx 2.7 \times I_0 \exp(T/T_0)$, $T_0 \approx 2 \times T$, and $T_1 \approx 2 \times T$.

3.4 Summary

Quantum-cascade lasers are semiconductor laser sources whose optical transitions are between different subbands of the conduction band of a semiconductor heterostructure. Because of their unipolar operation, active regions can be cascaded, allowing high output power even at long wavelengths. Furthermore, because of the parallel dispersion of the subbands, the gain spectrum of QCLs is narrow compared to the gain spectrum associated with interband transitions in semiconductor laser diodes. Expressions for the threshold current density and for the differential quantum efficiency are obtained from an analysis of the rate equations at and above threshold, and a strong impact of the injection efficiency in both of these quantities is found.

We proposed a method to model QCL performance. This method is used to estimate the thermal conductance of a device through a fit of the optical power with duty cycle at a fixed temperature. It allows furthermore the prediction of laser performance parameters as the maximum duty cycle and the maximum light output power. Such a straightforward method should prove very useful for rapid analysis strategies for laser performance optimization, particularly for maximizing the average power and for troubleshooting thermal management.

4 Fabrication and characterization of quantum cascade lasers

In this chapter we review relevant steps for QCL fabrication. We introduce the gas-source molecular beam epitaxy technique, which is a widely used growth method of semiconductor heterostructures. We review basic characteristics and fabrication steps of Fabry-Pérot resonators. We discuss laser mounting and standard characterization methods of MIR QCLs, and conclude this chapter presenting an improved growth sequence for the fabrication of buried-heterostructure QCLs with high thermal conductivity.

4.1 Gas-source molecular beam epitaxy

Molecular beam epitaxy (MBE) is a widely used growth method of semiconductor heterostructures. It was developed by the late 1960s at the Bell Telephone Laboratories by J. R. Arthur and Alfred Y. Cho. MBE growth is characterized by relatively slow growth rates (~ 10 nm/min), which allows a high thickness control (~ 5 $\AA$) of the deposited layers. The epitaxial growth ("epi" = surface, "taxis" = arrangement) requires ultra high vacuum with pressures as low as $\sim 10^{-9} - 10^{-12}$ mbar. This is because the species are provided by atomic or molecular beams directed toward the sample, which requires a minimization of residual species and mean free paths of ~ 1 m. The growth quality is controlled in-situ observing the diffraction pattern arising from high energy (~ 10 keV) electrons generated by an electron gun and directed towards the sample surface (RHEED).

Figure 4.1 illustrates schematically an MBE system equipped with three effusion (also

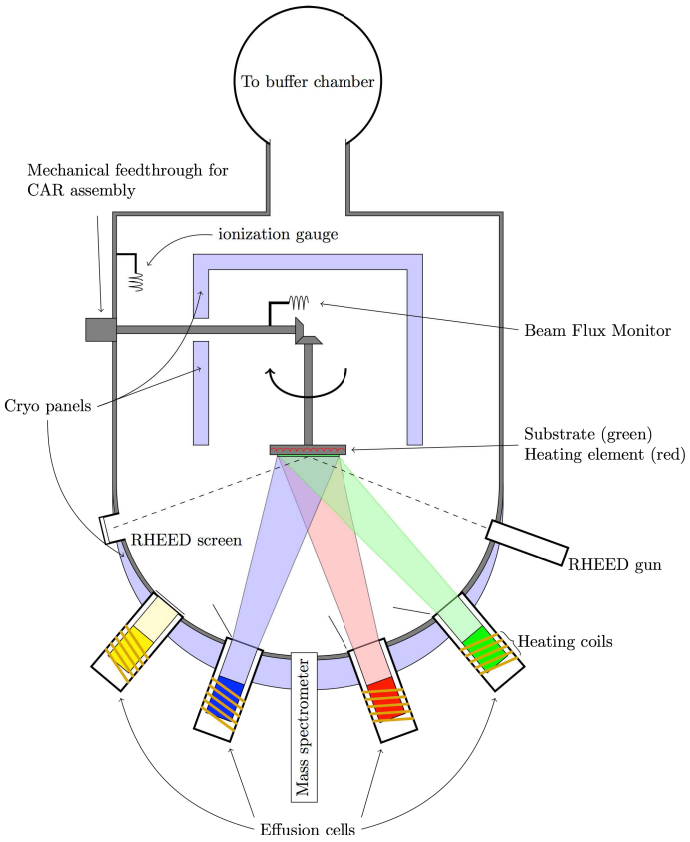

Figure 4.1: Simplified representation of a MBE system. (Source: Wikipedia.org)

Knudsen, or "K") cells, which, when heated, provide the species during the MBE growth. While many elements provide a beam of atoms when heated (e.g. group III elements), some evaporate as molecules instead. This is the cases of group V elements, which are provided by thermal cracking of hydride gas molecules. The epitaxial growth technique which uses a combination of solid elemental sources and gas molecules is called gas-source molecular beam epitaxy (GSMBE).

The growth of the laser structures presented in this work as well as the second growth (regrowth) for buried-heterostructure fabrication (section 4.4) were carried out in a Riber Compact 21 T MBE system. In, Ga, and Al are obtained from solid sources, while As ans P are supplied by pre-cracked arsine (AsH_3) and phosphine (PH_3). Si doping for the active region and Fe doping for the regrown insulator layers are supplied from solid sources as well.

After growth, the growth quality is controlled using double crystal X-ray diffraction (DCXRD). Through a direct comparison between simulated and measured data, this technique allows an efficient control over the real thicknesses and compositions of the grown layers (Fig. 4.2).

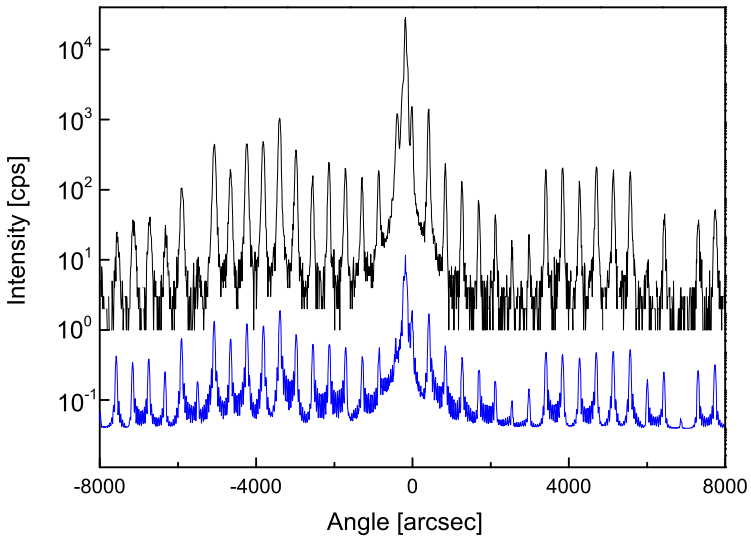

Figure 4.2: Measured (black) and simulated (blue) DCXRD rocking curves for a 40-period $In_{0.73}Ga_{0.27}As/In_{0.55}Al_{0.45}As$-AlAs QCL structure.

4.2 Fabrication of laser ridges

4.2.1 Fabry-Pérot geometry

After growth, the QCL wafer is processed into laser ridges in order to provide an optimum confinement of the laser mode and enhance stimulated emission. A simple device geometry here is the Fabry Pérot resonator [125, 126], where the gain medium is placed within a cavity terminated at the ends with partially reflecting mirrors (Fig. 4.3). Photons generated within the gain medium travel back and fort along the cavity. The total photon loss is given by waveguide and mirror losses, which are labeled by α_w and α_m, respectively.

The mirror loss α_m is a function of the facet reflectivity and, therefore, of the refractive

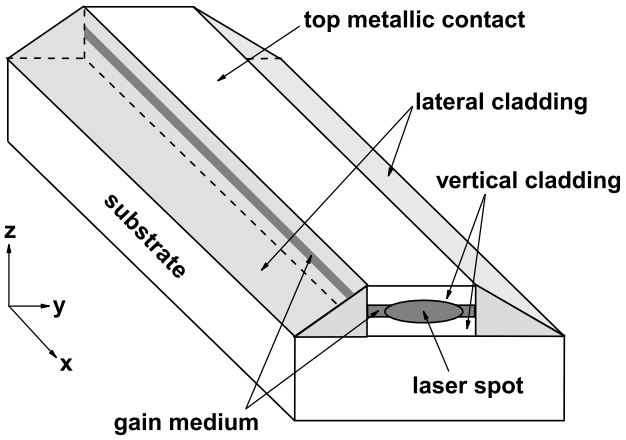

Figure 4.3: Schematic representation of a laser ridge waveguide (Fabry-Pérot resonator).

index for the correspondent photon energy. α_m changes only weakly with temperature in the range $100-300$ K. α_w, on the other hand, is dominated by free-carrier absorption and it increases somewhat with increasing temperature due to the decreasing electron mobility [127, 128, 129].

At threshold, the laser gain G_{th} in the active region is exactly balanced by the sum of all the losses experienced by the light in one round trip in the optical cavity [130]. Assuming equal reflectivities R_f on each facet this condition is written as

$$R_f^2 \cdot \exp(2G_{th}L)\exp(-2\alpha_w L) = 1\ , \tag{4.1}$$

with L the cavity length. Rearranging terms we write α_m as

$$G_{th} = \alpha_w - \frac{\ln(R_f)}{L} \quad \rightarrow \quad \alpha_m \equiv -\frac{\ln(R_f)}{L}\ . \tag{4.2}$$

We determine the mirror loss α_m from mode spacing measurements using a high-resolution spectrometer[1]. The waveguide loss is estimated using a phenomenological free-electron model extended to semiconductor heterostructures [129]. Calculated values from this model are in excellent agreement with measured values, e.g. from L-dependent

[1]Laser bars with short $L \sim 1$ mm cavity lengths are used for this purpose. A typical mode spacing for InGaAs/InAlAs MIR QCLs is ~ 1.5 cm^{-1}, which leads to an effective refractive index of $n_{\text{eff}} \sim 3.14$ and a facet reflectivity of $R_f = [(n_{\text{eff}}-1)/(n_{\text{eff}}+1)]^2 \sim 0.26$.

measurements of the threshold current density [57] and the differential slope efficiency [59].

4.2.2 Vertical and lateral confinement of the laser mode

The laser mode is confined along a specific direction using index-guiding, i.e., trapping the light in the region with the highest refractive index. In the direction perpendicular to the heterolayers, z-direction in Fig. 4.3, index-guiding is achieved using highly-doped materials as cladding layers. For InGaAs/InAlAs MIR QCLs, these layers consist on n-doped InGaAs with doping concentrations within $10^{17} - 10^{18}$ cm^{-3}. As the refractive index reduces with increasing doping concentration, the vertical confinement of the laser mode is enhanced. In addition, low doped, thin semiconductor layers are included between the active region and the cladding layers in order to increase the refractive index contrast and improve mode confinement further (Fig. 4.4).

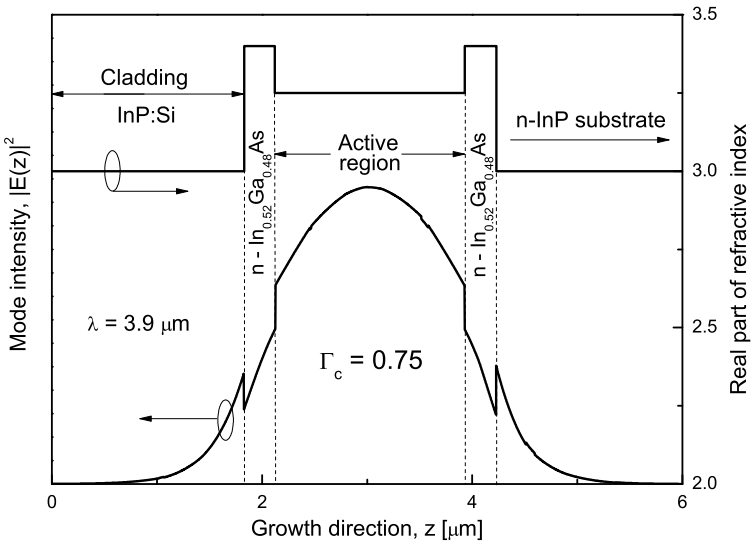

Figure 4.4: Calculated light intensity (left axis) for a short-wavelength ($\lambda \sim 3.9$ μm) QCL as a function of distance along the direction of growth. The calculated refractive index is included (right axis). The cladding and InP substrate layers are n-doped to $\sim 10^{17}$ cm^{-3}. Low-doped ($\sim 10^{16}$ cm^{-3}) $In_{0.52}Ga_{0.48}As$ layers are placed between active region and cladding layers in order to increase the refractive index contrast and the confinement efficiency of the laser mode. The calculated confinement factor is $\Gamma_c = 0.75$.

The confinement factor Γ_c quantifies the confinement of the laser mode along the vertical direction. It is defined as the mode overlap with the active region (AR) as

$$\Gamma_c = \frac{\int_{\mathrm{AR}} |E(z)|^2 dz}{\int_{-\infty}^{\infty} |E(z)|^2 dz}, \tag{4.3}$$

where $|E(z)|^2$ represents the electric field intensity. Typical values of Γ_c for MIR QCLs lie within the $0.5 - 0.9$ range.

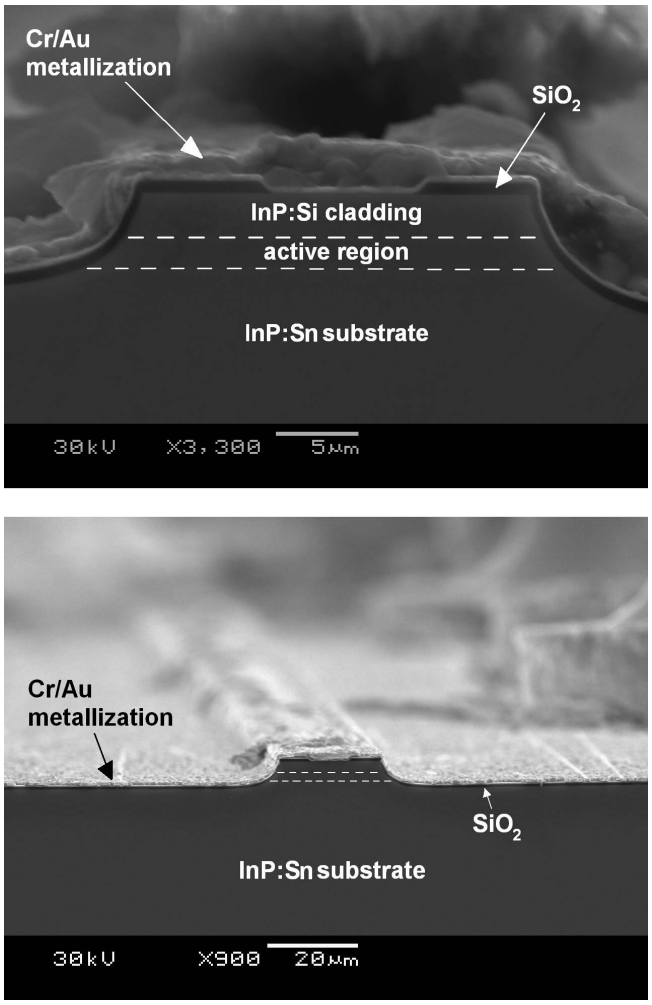

Figure 4.5: SEM captures of a QCL ridge facet. Active regions and cladding layers can be recognized. SiO_2 (500 nm-thick) is used for the lateral cladding. Metallization is done by thermal evaporation of Cr(20 nm)/Au(100 nm).

Similarly, along the lateral direction, *y*-direction in Fig. 4.3, mode confinement is achieved using low-refractive index materials, as for example SiO_2 or SiN for MIR QCLs. These materials are deposited by reactive magnetron sputtering and serve also as electrical insulators for the side walls. The waveguide fabrication itself is done by a combination of conventional optical lithography techniques and chemical selective etching. Metallization is done by thermal evaporation of Cr(20 nm)/Au(100 nm). Figure 4.5 shows a scanning electron microscope (SEM) pictures of a QCL laser ridge facet.

4.3 Device mounting and characterization

After metallization, laser bars of $1-6$ mm length are cleaved and mounted onto a submount, which serves as an extractor of heat generated during the laser operation. The submount material should have therefore a high thermal conductivity. In order to prevent the formation of dislocations and reduce mechanical stress, the submount material should furthermore have a similar thermal expansion coefficient as the laser chip. Typical submount materials for MIR QCLs are cooper (Cu), aluminium nitride (AlN), and diamond. After mounting, laser stripes are electrically contacted using a metallic wire-bonder. Figure 4.6 shows the SEM capture of a bonded QCL stripe. The mounted QCL chip containing several laser stripes is also shown.

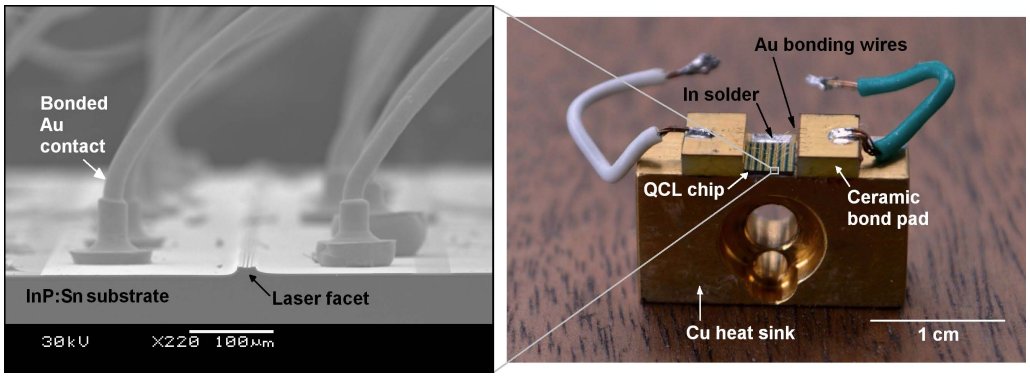

Figure 4.6: QCL mounted onto a Cu heat sink and ready for characterization. The amplification shows the SEM capture of a laser stripe.

For electrical characterization in pulsed operation mode use the Avtech AV-107C-B current source. Current pulses of 100 ns width and low duty cycles (0.01%) are used in order to avoid laser heating. The current and the voltage signals are monitored using an oscilloscope. The average output power is measured using a thermopile detector placed in front of the laser facet. The peak power is then calculated as the product of the average output power and the duty cycle.

Figure 4.7 shows typical measurement data for a short-wavelength QCL. Plotted here are the voltage U and the peak optical power P as a function of current I. The threshold current I_{th} and threshold voltage U_{th} are indicated. The differential quantum efficiency η_d is determined from the differential slope efficiency dP/dI, measured for the approximately linear $P(I)$ region between threshold and rollover.

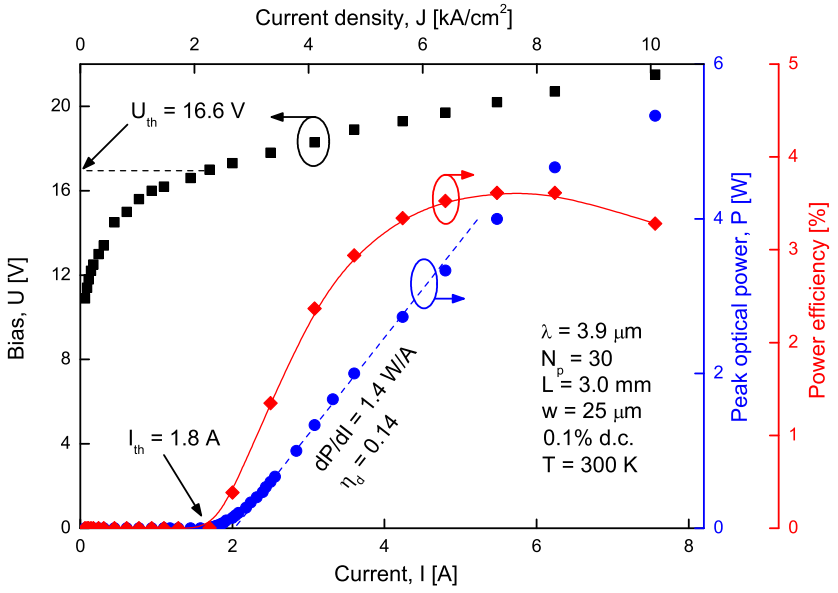

Figure 4.7: Standard electric and light-output characterization of a MIR QCL. The QCL active region contains $N_p = 30$ cascades. Considered is a stripe with $w = 25$ μm-width and $L = 3$ mm length. The data are collected in pulsed operation mode using 100 ns current pulses with 10 kHz repetition rate (0.1 % d.c.).

For temperature dependent measurements we mount the devices into a nitrogen gas flow cryostat. To monitor the heat sink temperature we use a Si-diode mounted close to the laser. In this way we are able to determine the threshold current and the slope effi-

ciency characteristic temperatures, T_0 and T_1, respectively. These quantities parametrize the increase (decrease) of the threshold current (differential slope efficiency) with increased temperature. Within a temperature range $\Delta T = T_{\max} - T_{\min}$, these temperature dependencies are written as:

$$J_{th}(T_{\min} + \Delta T) = J_{th}(T_{\min}) \exp(\Delta T / T_0) \tag{4.4a}$$

$$dP/dI(T_{\min} + \Delta T) = dP/dI(T_{\min}) \exp(-\Delta T / T_1)\,. \tag{4.4b}$$

Figure 4.8 shows the temperature dependence of J_{th} and dP/dI for the device of Fig. 4.7. Typical T_0 values in MIR QCLs lie within the $50-250$ K range (see also Fig. 5.19 in the next chapter). Reported T_1 values for MIR QCLs lie within $100-600$ K.

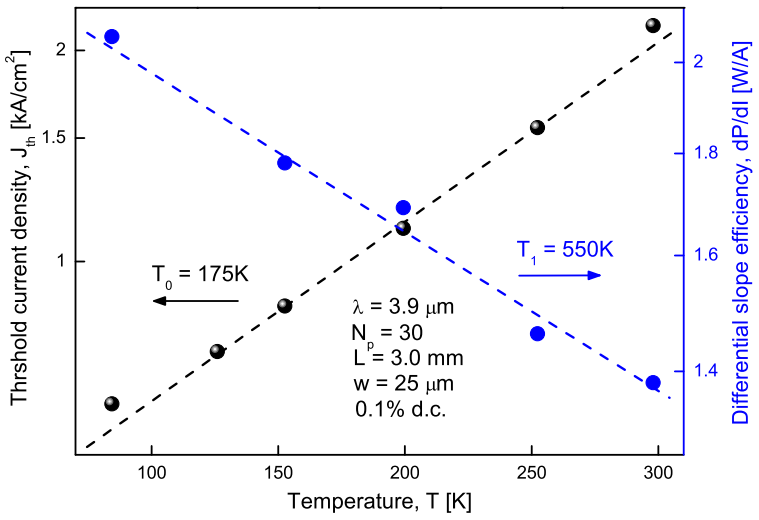

Figure 4.8: Threshold current density and differential slope efficiency as a function of temperature for the device of Fig. 4.7. Characteristic temperatures $T_0 = 175$ K and $T_1 = 550$ K are determined using equations 4.4a and 4.4b, respectively.

Further experimental methods are available for QCL characterization. Examples here are beam quality studies using near- and far-field measurements, and Fourier transform infrared spectroscopy (FTIR) for the determination of the laser emission spectrum.

4.4 Buried-heterostructure devices

The heat extraction capabilities of a MIR QCL device are considerably increased through the fabrication of a buried-heterostructure (BH), where the etched lateral ridge is overgrown with a semi-insulating, highly thermally conductive, semiconductor material. An ideal candidate here is iron doped indium-phosphide (InP:Fe).

The majority of buried-heterostructure quantum-cascade lasers (BH-QCLs) with InP:Fe lateral cladding use the metal-organic vapor-phase epitaxy (MOVPE) growth technique for the growth of both the QCL structure and the semi-insulating material [113, 118, 131]. Furthermore, the typical growth temperatures required for MOVPE ($\sim$650 °C) makes this technique unsuitable for the regrowth of InP:Fe in QCL structures with a high degree of internal strain [54]. A good example here are short-wavelength ($3-5$ μm) QCLs based on strain-compensation of $In_xGa_{1-x}As$ ($x = 0.7-1.0$) wells and $1-2$ nm-thick AlAs barriers to an InP-substrate. Experimental evidence indicates that the temperatures experienced during an MOVPE growth of these structures would lead do laser degradation due to strain-relaxation and strain-driven interdiffusion [54].

An alternative to this situation is the usage of GSMBE, which uses lower growth temperatures $<$600 °C than MOVPE, for growing both the laser core and the InP:Fe material [54, 64]. BH-QCL devices using InP:Fe regrown by GSMBE have been demonstrated for lattice-matched ($\lambda = 10.7$ μm) and also for strain-compensated ($\lambda = 3.9$ μm) QCLs [54, 64]. In none of the cases a deterioration of QCL characteristics after the InP:Fe regrowth was observed.

A number of void-like defects however appear when initiating the InP:Fe GSMBE-regrowth directly on the sides of the laser ridge, which are mostly located at the arsenide-phosphide interface between the active region and the regrown InP:Fe. The appearance of these void-like defects is reproducible and depends only weakly on the InP:Fe (re)growth temperature and PH_3 flux (Fig. 4.9).

Furthermore, electrical insulation capabilities of the InP:Fe are not affected by the presence of the void-like defects. (The laser threshold, for example, in QCLs with and

without the InP:Fe regrowth remains unchanged.) It is however expected that these defects will reduce lateral heat flow and affect the heat extraction capabilities of the BH device. As a matter of fact, no cw laser operation has been achieved by BH devices using GSMBE for the InP:Fe regrowth directly on the sides of the laser ridge [54, 64].

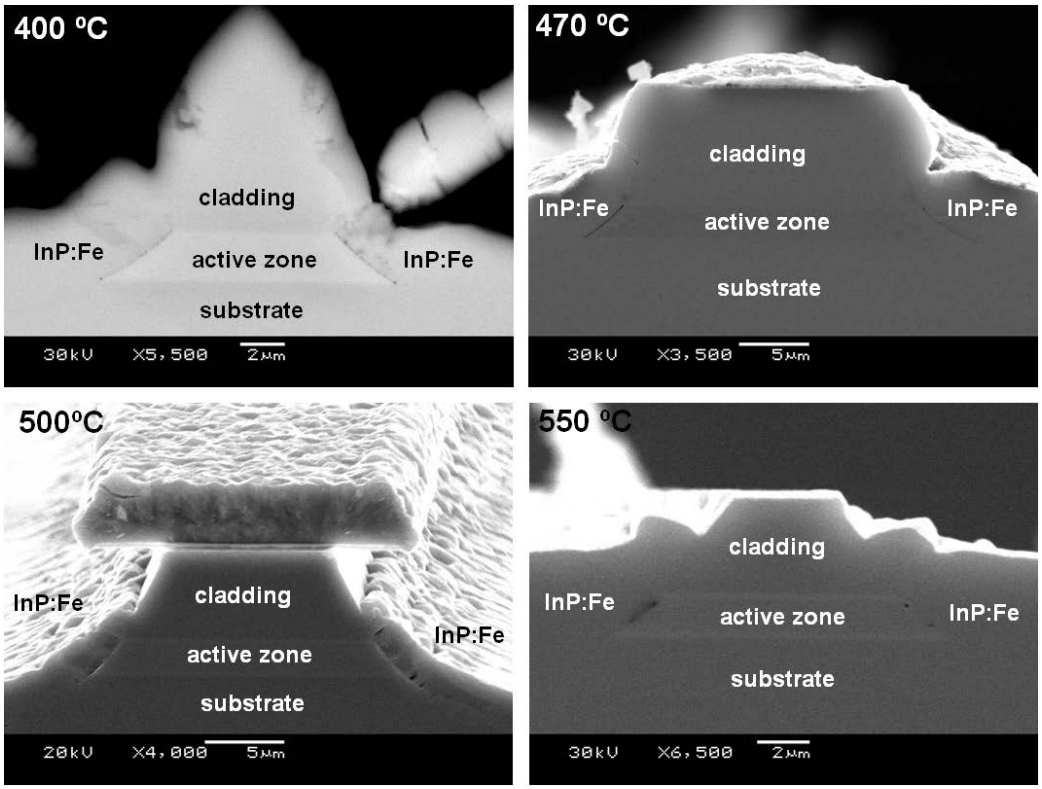

Figure 4.9: High-magnification SEM captures of BH-QCLs using InP:Fe overgrown by GSMBE. The presence of void-like defects on the interface between the active zone and the overgrowth material can be recognized. The temperature for the InP:Fe regrowth is indicated.

The thermal conductivity of BH-QCL devices using InP:Fe regrown by GSMBE is however significantly improved using a thin ($\sim$20 nm-thick) $In_{0.52}Al_{0.48}As$ spacer layer between the laser ridge sidewalls and the InP:Fe layers. This procedure preserves the crystal quality of the interface, maintains the high electrical resistivity of the InP:Fe material, and improves significantly heat extraction from the laser core.

We show in Fig. 4.10 further cleaved facets of QCL ridges overgrown by GSMBE. The used QCL active region in both panels is the same and uses the InGaAs/InAlAs-AlAs heterosystem strain compensated to InP [55, 92, 103, 120, 132, 133]. The waveguide fabrication is done by means of chemical selective etching, resulting in a narrow facet width ($\sim$7 μm). Panels (a) and (b) of this figure show the overgrown QCL ridge sidewalls for a reference (without the InAlAs spacer layer) and for the optimized (using the InAlAs spacer layer) BH-QCL, respectively. Both devices use $\sim$6 μm-thick InP:Fe regrown at 500 °C at the growth rate of 1 μm/hour.

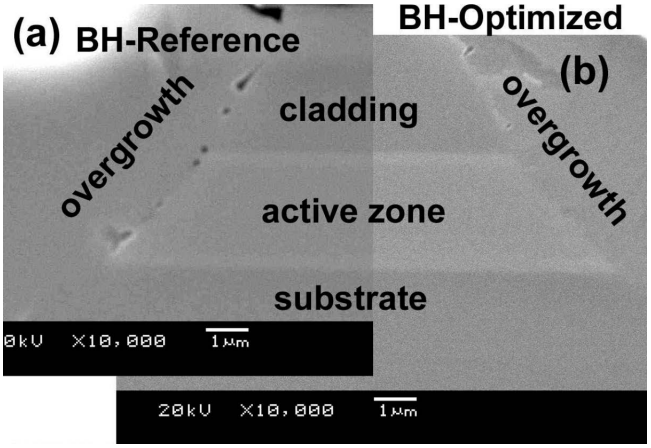

Figure 4.10: High-magnification SEM captures of BH-QCLs using InP:Fe overgrown by GSMBE. In (a) the InP:Fe overgrown starts directly on the etched sidewall of the laser core. In (b) the InP:Fe overgrown is done on the 20 nm-thick $In_{0.52}Al_{0.48}As$ spacer layer previously grown on the etched sidewall.

In the reference BH-QCL (Fig. 4.10a), the QCL wafer was heated under a PH_3 flux and the overgrowth of InP:Fe was done directly on the etched sidewall. In the optimized BH-QCL (Fig. 4.10b), the QCL wafer was heated in an AsH_3 flux, then the regrowth was started with the 20 nm-thickS $In_{0.52}Al_{0.48}As$ spacer layer. Immediately after, the gas flux was switched to PH_3 and the overgrowth continued with InP:Fe. The major difference between the overgrowth recipes in the two cases is that in the optimized recipe, Fig. 4.10b, the sidewalls of the active zone (consisting of strain-compensated InGaAs/InAlAs quantum wells) are never exposed to PH_3. The gas switching from AsH_3 to PH_3 is done

after the growth of the thin $In_{0.52}Al_{0.48}As$ lattice-matched to InP. We believe that the appearance of the voids is due to local side-wall surface corrugations, which arise due to P-As exchange at the exposed sides of InGaAs layers (both InGaAs spacers, and InGaAs quantum wells). The InAlAs surface is apparently not as sensitive to the P-As exchange, probably due to a lower surface mobility of the add-atoms.

The low-magnification capture of the optimized BH-QCL is shown in Fig. 4.11. Metallization is done by thermal evaporation of Cr/Au and by a thick ($4-5$ μm) galvanic Au layer, which improve thermal conductivity further. The dashed line in Fig. 4.11 represents the location of the $In_{0.52}Al_{0.48}As$ spacer layer.

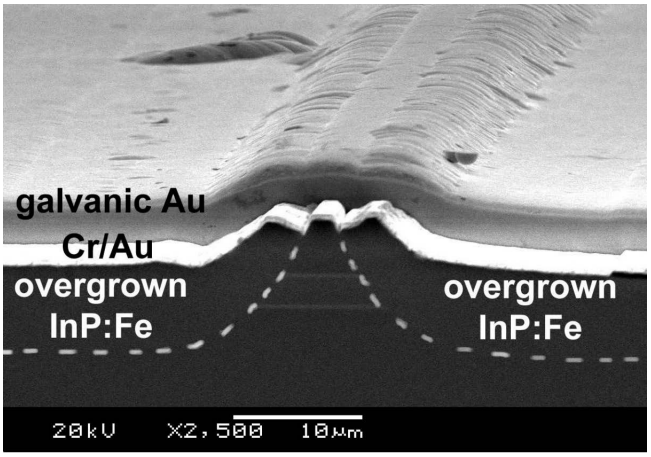

Figure 4.11: Low-magnification SEM capture of the BH-QCL with the optimized growth sequence. The dashed line marks the location of the $In_{0.52}Al_{0.48}As$ spacer layer.

4.4.1 Improved thermal conductivity and continuous wave operation

In order to improve heat dissipation, laser ridges of 7 μm-width were soldered epi-down onto an AlN submount using a close to eutectic Au:Sn (80:20) solder (Fig. 4.12).

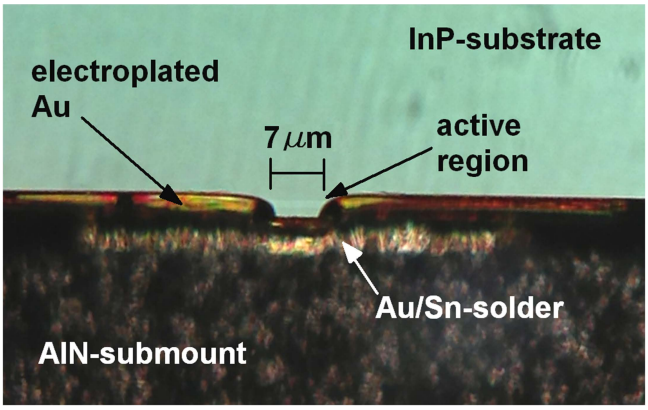

Figure 4.12: Facet of a BH-QCL soldered epi-down onto an AlN submount.

We measure the threshold current density J_{th} as a function of temperature for the optimized BH-QCL in both pulsed and cw operation modes. Results are shown in Fig. 4.13. A characteristic temperature of $T_0^{\mathrm{cw}} = 282$ K is measured in cw operation mode in the temperature range $100 - 180$ K. In this range, the threshold voltage reduces from 15.2 V to 14.0 V. For larger temperatures, J_{th} increases supra-exponentially achieving a value of 4.3 kA/cm^2 at 210 K. The maximum cw operating temperature is 210 K. Operating the same sample with 100 ns current pulses and a low duty cycle (0.01 %) leads to a value of $T_0^{\mathrm{puls},1} = 452$ K in the temperature range $100 - 220$ K, and $T_0^{\mathrm{puls},2} = 153$ K for the temperature range $250 - 340$ K.

We determine the thermal conductance as a function of temperature by comparing J_{th} values in cw and pulsed operation modes [134]. Results are summarized in Fig. 4.14. For $T = 127$ K, we measure a thermal conductance of $C_{th} = 1020$ W/Kcm^2, which decreases to 500 W/Kcm^2 for $T = 210$ K. These values for C_{th} allow efficient heat extraction from the laser core and make laser action under cw operation possible.

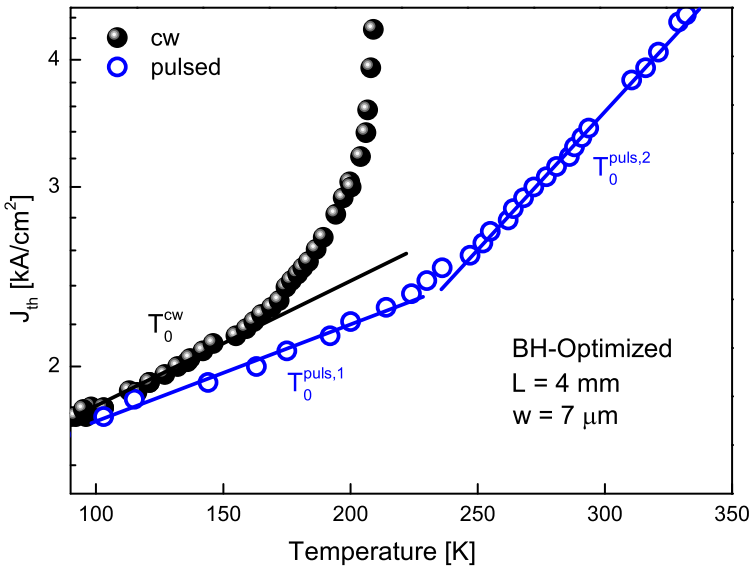

Figure 4.13: Measured threshold current density as a function of temperature for the optimized BH-QCL in cw (solid dots) and pulsed (circles) operation modes. Solid lines represent exponential fits to the data, resulting in threshold current characteristic temperatures of $T_0^{cw} = 282$ K, $T_0^{puls,1} = 452$ K, and $T_0^{puls,2} = 153$ K.

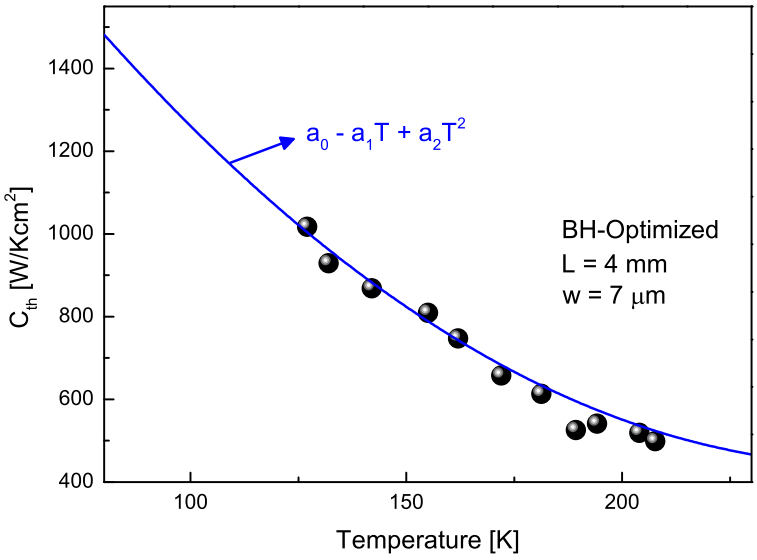

Figure 4.14: Measured thermal conductance as a function of temperature for the optimized BH-QCL. The solid line is the best fit to the data using the expression $C_{th}(T) = a_0 - a_1T + a_2T^2$ [135], resulting in the fit parameters $a_0 = 2630$, $a_1 = 17$, and $a_2 = 0.033$.

We approximate the measured temperature-dependence of C_{th} using a polynomial function of the form $a_0 - a_1 T + a_2 T^2$ with positive coefficients a_0, a_1, and a_2. Following heat transfer simulations on semiconductor heterostructures, H. K. Lee *et. al.* [135] demonstrated that this expression provides a good agreement between calculated and experimental data for the thermal conductance of QCLs. We include the fit of $C_{th}(T)$ using this formula in Fig. 4.14.

As next, we want to know how good the obtained C_{th} is with respect to literature values. Figure 4.15a shows collected MIR QCL data from the literature for C_{th} as a function of reciprocal cavity width. The different symbols used in this picture distinguish between the used submount materials. Due to the better heat dissipation capabilities of narrower laser stripes [131, 136], we observe that C_{th} follows an approximately linear dependence on the reciprocal cavity width (dashed line). Solid blue circles represent measured C_{th} values for devices grown by our research group and using the optimized InP:Fe regrowth sequence. We observe that these values incorporate well into the general statistics shown in this figure, which indicates that heat extraction capabilities are obtained using GSMBE-overgrown BH-QCLs, which are comparable to other approaches as, for example, those who use MOVPE.

To conclude, we want to analyze the improvement of the thermal conductance in BH-QCLs using the InAlAs spacer layer with respect to reference devices (without the InAlAs spacer layer). Reference BH-QCL devices do not show cw operation. However, values of C_{th} are estimated fitting the optical power as a function of duty cycle (section 3.3), a method which is specially accurate at low temperatures. Figure 4.15b shows low-temperature values for C_{th} as a function of reciprocal cavity length for the optimized BH-QCL and for reference devices. A value of C_{th} = 1480 W/Kcm^2 for the optimized BH-QCL is extrapolated using Fig. 4.14. The presence of void-like defects in the reference devices (Fig. 4.10a) results in lower C_{th} values (334 W/Kcm^2 for a $w = 10.4$ μm-wide QCL ridge and 185 W/Kcm^2 for a $w = 27$ μm-wide QCL ridge). Figure 4.15b includes data for a plasma-etched QCL using SiN dielectric insulation [48], which resulted in a C_{th} of 720 W/Kcm^2 for a $w = 6$ μm-wide stripe.

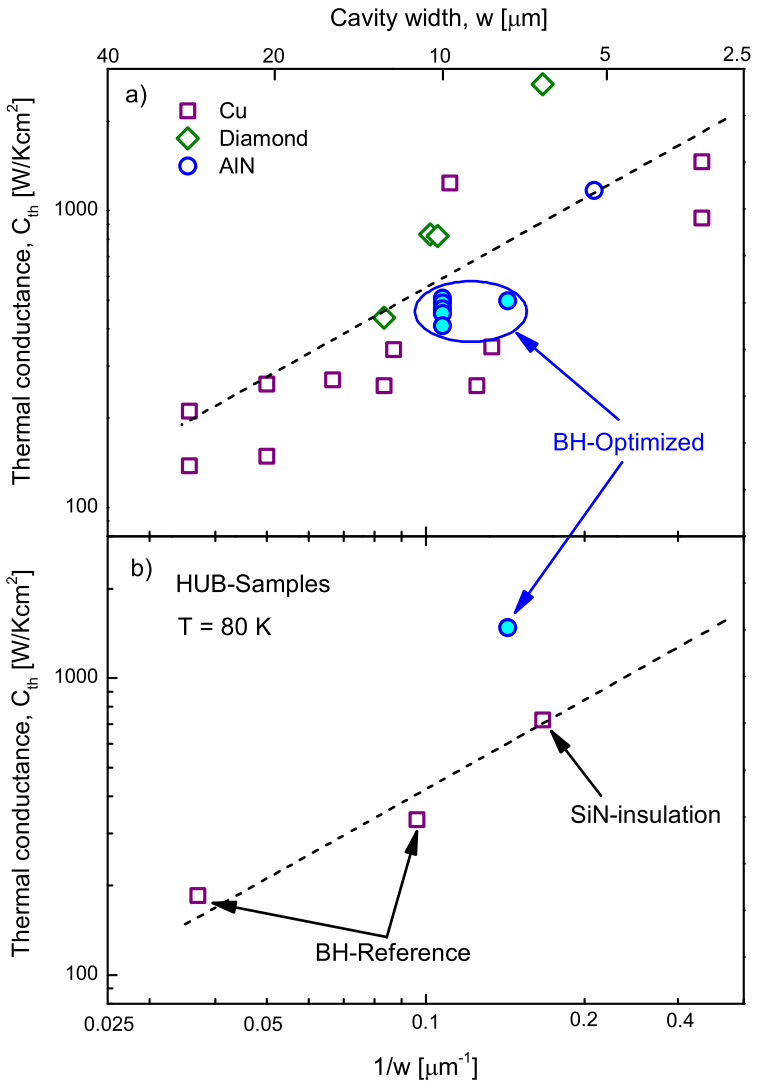

Figure 4.15: Thermal conductance as a function of reciprocal cavity width for several reported MIR QCLs. Squares (diamonds, circles) correspond to devices mounted on Cu (diamond, AlN) submounts. The upper panel (a) shows high-temperature ($\sim$ 300 K) data collected from the literature [111, 112, 115, 116, 117, 119, 131, 134, 137, 138, 139, 140, 141, 142, 143, 144] and also data corresponding to BH-QCLs using the optimized InP:Fe regrowth sequence (solid blue circles). The lower panel (b) shows low-temperature (80 K) data for QCL devices grown by our research group (see text for references). The dashed line illustrates the approximate linear scaling of the C_{th} with $1/w$.

Values for the thermal conductance C_{th} of our two reference BH-QCLs [61, 64] and the C_{th} value of the thin dielectrically insulated QCL show the same trend vs. $1/w$,

indicating that the reference BH-QCLs are not any better than the dielectrically insulated device in terms of heat dissipation. However, the measured C_{th} for the optimized BH-QCL (regrown with the 20 nm-thick $In_{0.52}Al_{0.48}As$ spacer layer) clearly pins off this trend showing at least a two-fold improvement with respect to the reference BH-QCLs and the dielectrically insulated QCL. This demonstrates the high impact of the void-like defects we obtained before (Fig. 4.9 and Fig. 4.10a) on the heat dissipation capabilities of buried-heterostructure devices.

4.5 Summary

Realization of QCL devices requires the careful execution of several experimental steps. This starts with the epitaxial growth of the laser wafer and continues with the processing of laser ridges. The simplest waveguide geometry is the Fabry-Pérot resonator, where the gain medium is placed within a cavity terminated at the ends with partially reflecting mirrors. (A typical value for the (uncoated) mirror reflectivity is $R_f = 0.26$.) Vertical and lateral confinement is achieved by index-guiding, i.e., trapping the light in the highest refractive index region. A combination of high and low doped InGaAs layers is used for the vertical confinement of the laser mode in MIR QCLs, resulting in vertical confinement factors $\Gamma_c = 0.5 - 0.9$. Application of a dielectric (e.g. SiO_2) material for the lateral cladding results in high lateral confinement of the laser mode (lateral confinement factor near unity for ridge widths of $\sim 20\,\mu$m).

The heat extraction capabilities of MIR QCLs are considerably increased through the fabrication of a buried-heterostructure (BH). Here, the etched lateral ridge is overgrown by a semi-insulating, highly thermally conductive, semiconductor material. An ideal candidate here is iron doped indium-phosphide (InP:Fe). The thermal conductivity of BH-QCL devices using InP:Fe regrown by GSMBE is further improved using a thin (~ 20 nm-thick) $In_{0.52}Al_{0.48}As$ spacer layer between the laser ridge sidewalls and the InP:Fe layers. This improves also the crystal quality of the interface and preserves the high electrical resistivity of the overgrown material. The optimized regrowth sequence

led to cw operation up to 210 K of a 7 μm-wide BH-QCL with an emission wavelength of 5.4 μm. The measured thermal conductance is $C_{th} = 500$ W/Kcm^2 at 210 K and 1020 W/Kcm^2 at 127 K, which is comparable to the state of the art BH-QCLs using InP:Fe regrown by MOVPE.

5 Carriers leakage and hot electron effects

Optimization of QCL performance depends not only of aspects as heat management and chip-packaging, but also on improving active region designs to reduce several leakage channels of charge carriers [57, 58, 59, 92, 99, 102, 103, 107, 145]. This is crucial for example to achieve high-power cw operation, where an increment of the cw power efficiency by a factor of ~ 2 is predicted for complete suppression of carriers leakage [103]. However, mechanisms through which leakage of charge carriers affects QCLs performance have not been thoroughly researched.

In this chapter we analyze elastic and inelastic scattering in MIR QCLs. We focus here on temperature driven scattering from quantum well confined states into higher states. We present methods for the experimental determination of the correspondent leakage current at and above laser threshold. We further demonstrate the need of considering the effect of hot electrons (i.e. electrons characterized by a temperature larger than the lattice temperature) when analyzing transport characteristics of QCLs. We demonstrate that even at temperatures low enough to neglect inelastic scattering, carriers leakage due to elastic scattering becomes significant for devices operating at high electron temperatures, leading to important consequences for QCL performance.

5.1 Non-radiative scattering

5.1.1 Electron-phonon interaction

The importance of electron-phonon interaction for electron transport in semiconductor heterostructures is widely addressed in the literature. In particular, electron-longitudinal-optical-phonon (ELO) interactions plays a key role in QCLs: it allows a fast depopulation of the lower laser state and favors electron relaxation in the injector region through the emission of phonons[1]. We start our analysis writing the ELO-interaction hamiltonian and then we calculate several scattering rates for LO-phonon absorption and emission. The impact of ELO scattering on QCL performance is discussed in sections 5.2.1 and 5.2.2.

For our discussion we adopt a formalism which has been first proposed by P. J. Price (IBM Thomas J. Watson Research Center) in the year of 1980 [148]. This formalism has been then further developed by P. Harrison (University of Leeds) in his popular book first published in the year of 1999 [88]. The mainline of the relations used in this thesis can be considered a synthesis of ideas from these two references and from the works of M. Stroscio *et. al.* [149] and X. Gao *et. al.* [150] on the issue.

Consider the wavefunction for the phonon-induced potential in a bulk material with propagation vector $\vec{q}$:

$$\phi(\vec{r}) = \rho(q)\exp\left(-i\vec{q}\cdot\vec{r}\right) . \tag{5.1}$$

The normalization coefficient $\rho(q)$ can be determined from the orthonormality and completeness conditions imposed on the phonon wavefunctions, resulting in:

$$|\rho(q)|^2 = \frac{\hbar}{\varepsilon_0 V_{\mathrm{ol}} |\vec{q}|^2 \partial\varepsilon(\omega)/\partial\omega} , \tag{5.2}$$

with the crystal volume $V_{\mathrm{ol}} = S \cdot L$ and the dielectric function $\varepsilon(\omega)$. Altogether, the normalized wave function of a simple phonon mode can be written as:

[1] Acoustic phonons are only weakly coupled to electrons; the correspondent scattering rates and small and are usually omitted in calculations [146, 147].

$$\phi = \left[\frac{\hbar}{\varepsilon_0 |\vec{q}|^2 \partial\varepsilon(\omega)/\partial\omega}\right]^{1/2} \frac{\exp(-i\vec{q}\cdot\vec{r})}{V_{\mathrm{ol}}^{1/2}} \,. \tag{5.3}$$

The total phonon interaction hamiltonian is obtained by summing equation over all phonon wavevectors:

$$\widetilde{H}^{LO} = e\sum_{\vec{q}}\phi = e\sum_{\vec{q}}\left[\frac{\hbar}{\varepsilon_0 |\vec{q}|^2 \partial\varepsilon(\omega)/\partial\omega}\right]^{1/2} \frac{\exp(-i\vec{q}\cdot\vec{r})}{V_{\mathrm{ol}}^{1/2}} \,. \tag{5.4}$$

With equation 5.4 and using Fermi's golden rule, we calculate the scattering rate $1/\tau_{ij}^{LO}$ between states i and j due to ELO interaction. Assuming parabolic subbands and making use of the heterostrcture's symmetry, i.e., splitting the electron wavefunction and the phonon momentum in components along and perpendicular to the direction of growth, the scattering rate is written as:

$$\frac{1}{\tau_{ij}^{LO}} = \frac{2\pi}{\hbar} |\langle j|\widetilde{H}^{LO}|i\rangle|^2 \delta(E_j - E_i) \tag{5.5a}$$

$$= \frac{2\pi e^2 (n_{LO} + 1/2 \mp 1/2)}{\varepsilon_0 S \partial\varepsilon(\omega)/\partial\omega} \sum_{\vec{k}_{\perp_j}} \Big| \sum_{q_z} \frac{1}{L^{1/2}} G_{ij}(q_z) \times \sum_{\vec{q}_\perp} \frac{1}{(|\vec{q}_\perp|^2 + |q_z|^2)^{1/2}} \frac{1}{S} \int \exp\left(-i(\vec{k}_{\perp_i} - \vec{k}_{\perp_j} + \vec{q}_\perp)\cdot\vec{r}_\perp\right) \mathrm{d}\vec{r}_\perp \Big|^2 \delta(E_j - E_i) \,, \tag{5.5b}$$

where z is the direction of growth, $\perp$ is the direction parallel to the layer's plane, $\vec{k}_{\perp_{(i,j)}}$ is the two-dimensional wave vector parallel to the layers plane for state i or j, and $r_\perp = (x, y)$ is the component of the position vector in this direction.

We introduced the temperature-dependence in the scattering rate via the phonon occupation probability $(n_{LO} + 1/2 \mp 1/2)$. The upper sign $(-)$ represents absorption, which reduces the phonon population from $(n_{LO} + 1)$ to n_{LO}, and the lower sign $(+)$ represents phonon emission, which increases the number of phonons from n_{LO} to $(n_{LO} + 1)$.

The quantity G_{if} in Eq. 5.5b is known as the electron-phonon coupling function or the form factor for ELO scattering [68, 151]. The electron-phonon coupling function is

the analogous quantity to the dipole matrix element $\langle z_{ij} \rangle = \int \xi_j^*(z) z \xi_i(z) \mathrm{d}z$ for the case of intersubband radiative transitions [74]. It depends on the envelope functions $\xi_{i,j}$ of the initial and final electron states and on the z-component of the phonon wave vector q_z:

$$G_{ij}(q_z) = \int \xi_j^*(z) \exp(-iq_z z) \xi_i(z) \mathrm{d}z \,. \tag{5.6}$$

Figure 5.1 shows calculated values for G_{if} for two conduction band states of a QCL structure.

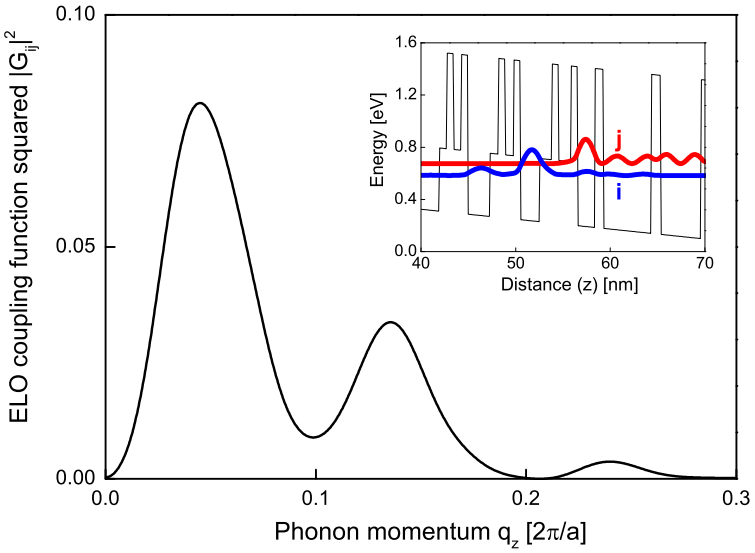

Figure 5.1: Calculated electron-phonon coupling function squared for two QCL conduction band states as a function of phonon momentum in the direction of confinement. A mean lattice constant of $a = 5.94$ Å is used for graphical representation purposes.

Figure 5.2 shows calculated ELO scattering rates as a function of total (potential and kinetic) energy. The same states pair (i, j) as in Fig. 5.1 is considered. This figure distinguishes furthermore between the initial state being either state i or j. For each case, the calculated scattering rate for phonon absorption and emission is shown. A lattice temperature of 300 K is used for calculations.

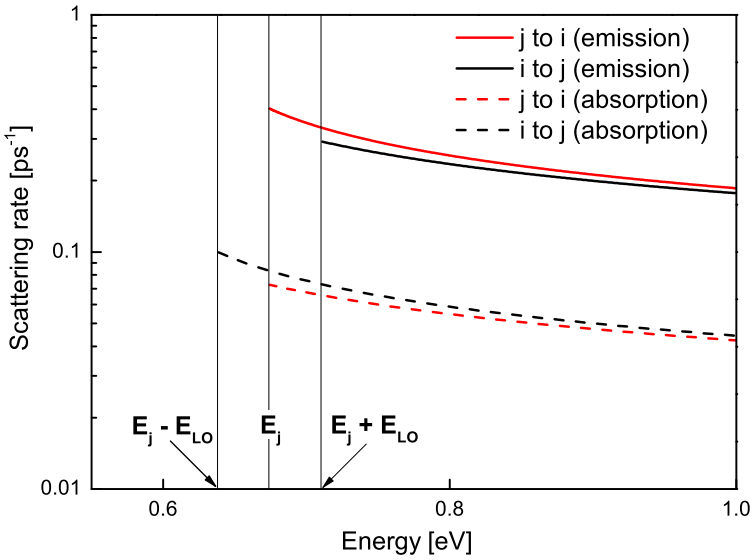

Figure 5.2: Calculated electron-LO-phonon scattering rates as a function of total (potential and kinetic) energy for a lattice temperature of 300 K. The states pair (i, j) of Fig. 5.1 is considered.

Threshold energy values for the scattering rate can be clearly recognized in Fig. 5.2. Electrons initially in state i and scattering up into state j need at least the energy $E_j \mp E_{LO}$ (E_{LO} is here the LO-phonon energy) in order to meet energy conservation. A different situation stands for electrons initially in state j: each one of these electrons is able to scatter down to state i either via phonon-absorption or through phonon-emission. We see furthermore that larger values are obtained for LO-phonon emission than for phonon-absorption. Reason for that is the phonon occupation probability. The ratio of the scattering rates for phonon-emission to phonon-absorption is given by $(n_{LO}+1)/n_{LO}$ and is temperature-dependent. This ratio is $\sim$4 for a temperature of 300 K.

For a fixed energy, calculated scattering rates for phonon emission and absorption differ slightly depending on which state (i or j) is chosen as the initial one (Fig. 5.2). Reason for that is the different phonon momenta required for the different cases, as Fig. 5.3 illustrates[2]. These differences in the scattering rates reduce with increasing energy due to the

[2]Consider for example an electron initially in state i (black dot in Fig. 5.3) and scattering via LO-phonon absorption up into state j (black dashed arrow in Fig. 5.3). An electron of the same energy yet initially in state j (red dot in Fig. 5.3) would need a larger phonon momentum to scatter to state i absorbing a phonon (red dashed arrow in Fig. 5.3). As a result, a smaller scattering rate is calculated for the second

near parabolicity of the subbands. As the energy increases the magnitudes of the needed phonon momenta for the different scattering paths become similar (Fig. 5.4).

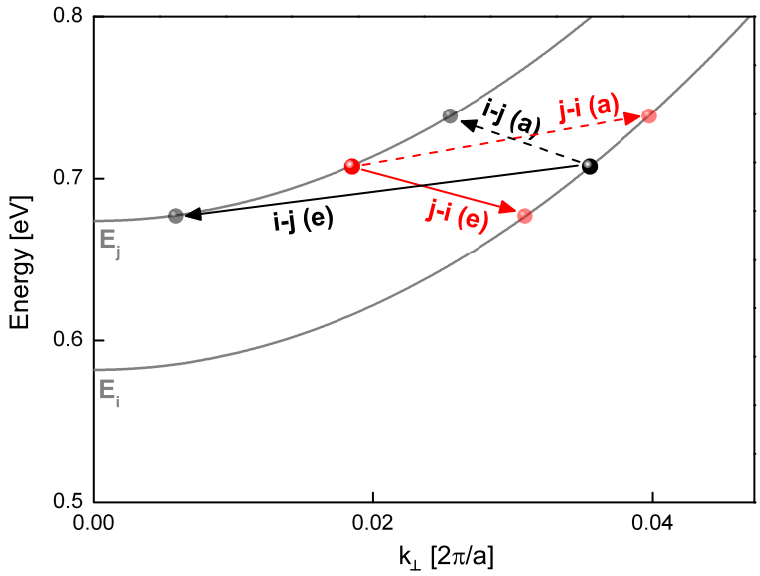

Figure 5.3: Calculated subband dispersion and several electron-LO-phonon scattering paths. For a fixed energy, an electron initially in state i (black dot) may scatter into state j via LO-phonon emission (black solid arrow) or absorption (black dashed arrow). Analogous applies for an electron initially in state j (red dot). States i and j and correspondent arrows are labeled and colored in analogy to Fig. 5.2. (a) denotes here LO-phonon absorption, and (e) denotes LO-phonon emission. A mean lattice constant of $a = 5.94$ Å has been used for graphical representation purposes.

case. Similarly, a larger scattering rate is obtained for an electron scattering via LO-phonon emission from state i to j (solid black arrow in Fig. 5.3) than in the opposite case (solid red arrow in Fig. 5.3).

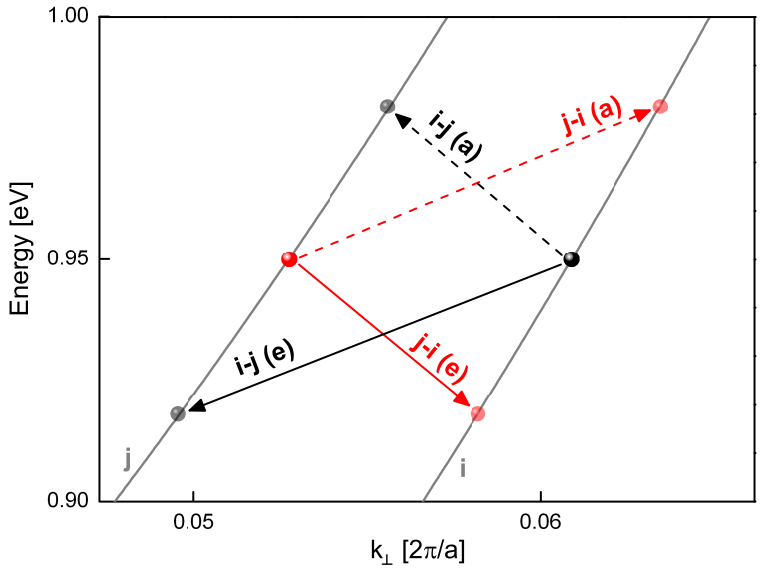

Figure 5.4: Calculated subband dispersion and different electron-LO-phonon scattering paths. States i and j and correspondent arrows are labeled and colored in analogy to Fig. 5.2. (a) denotes here LO-phonon absorption, and (e) denotes LO-phonon emission. A mean lattice constant of $a = 5.94$ Å is used for graphical representation purposes.

5.1.2 Interface roughness

Interface roughness-induced (IFR) scattering has attracted attention in the last years and its effects on QCLs transport characteristics are being increasingly researched. We review here important aspects of IFR scattering for MIR QCLs, including a discussion on the temperature dependence of the scattering rate.

IFR scattering is described parameterizing the random roughness profile of the interface in terms of the average rms height Δ and the characteristic roughness lateral size Λ [55, 152]. The intersubband IFR scattering rate depends furthermore on the amplitude of the conduction band offset $\delta U(z_l)$ at the individual interface l and the wavefunction amplitudes of the involved states. (For more details see for example the work of Chiu *et. al.* [153] and references therein.) The IFR scattering rate from the bottom of a subband i into a subband j is given by:

$$\frac{1}{\tau_{ij}^0} = \frac{\pi m^*}{\hbar^3}\Delta^2\Lambda^2 \sum_l [\delta U(z_l)\xi_i(z_l)\xi_j(z_l)]^2 \exp\left(\Lambda^2 q_{ij}^2/4\right), \tag{5.7}$$

where m^* is the conduction band effective mass, $\xi_{i,j}(z_l)$ are the envelope function amplitudes at the lth interface, and $q_{ij} = \sqrt{2m^*E_{ij}}/\hbar$ represents the absolute value of the two-dimensional energy-dependent scattering vector involved in the scattering process[3].

Figure 5.5a shows the calculated portion of a conduction band diagram of a strain-compensated MIR QCL. Envelope functions for the upper (i) and lower (j) laser levels are shown. The calculated energy separation between these states is $E_i - E_j = 0.27$ eV, which corresponds to an emission wavelength of $\lambda = 4.6\ \mu$m. The $In_{0.73}Ga_{0.27}As$ ternary is used to define the deep quantum wells, and the binary AlAs material is used for the barriers. The calculated values for the conduction band discontinuity between two layers, $\delta U(z_l)$, lie within the $0.73 - 1.21$ eV range. The factor $[\delta U(z_l)\xi_i(z_l)\xi_j(z_l)]^2$ of Eq. 5.7 is shown. The right panel (b) shows the calculated energy-dispersion for the involved states. A value of $q_{ij}^0 = 0.49\ \text{nm}^{-1}$ is calculated at the subband bottom.

[3] Similarly as in the case of ELO scattering we assume here band-parabolicity. This is done in order to avoid long expressions and because it leads to simple and elegant expressions.

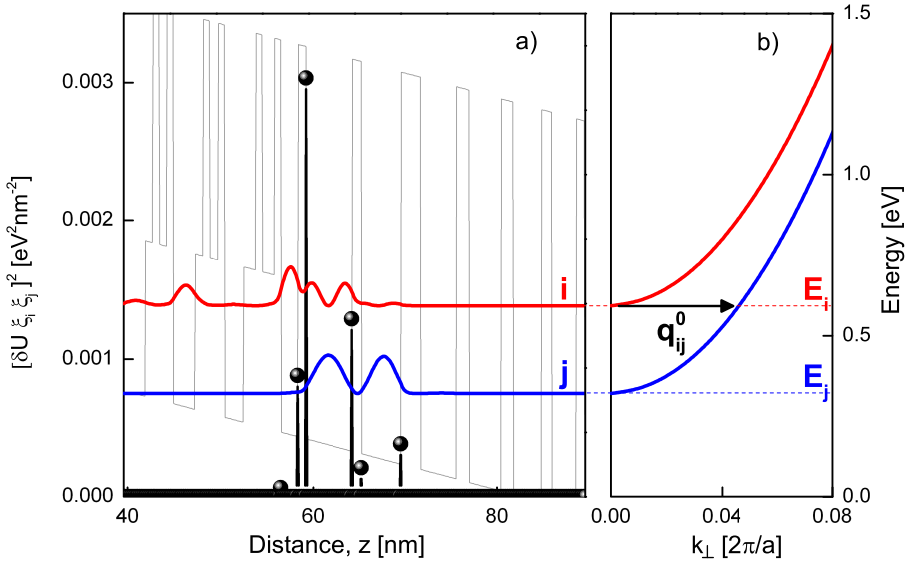

Figure 5.5: Calculated portion of a conduction band diagram (a) of a strain-compensated MIR QCL ($\lambda = 4.6\ \mu$m). Envelope functions of the upper (i) and lower (j) laser states are shown. Black dots indicate values for the calculated factor $[\delta U(z_l)\xi_i(z_l)\xi_j(z_l)]^2$ involved in scattering rate calculations (Eq. 5.7). The right panel (b) shows the correspondent energy dispersion as a function of wavevector perpendicular to the direction of growth. An energy difference between subband minima of $E_{ij} = 0.27$ eV, corresponding to a two-dimensional wavevector $q^0_{ij} = 0.49$ nm^{-1}, is calculated. A mean lattice constant of $a = 5.94$ Å is used for graphical representation purposes.

Using Eq. 5.7 we calculate the IFR scattering rate for the states in Fig. 5.5. We use the values of $m^* = 0.034 m_e$, as calculated for the quantum-well material, $\Lambda = 0.6$ nm, as typically used devices grown by molecular-beam epitaxy [153], and $\Delta = 0.1$ nm, which is extracted from the measured quantity $\Lambda\Delta = 0.6$ nm^2 [55]. Calculation results in a value of $1/\tau^0_{ij} \sim 0.5$ ps^{-1}, corresponding to a scattering time of $\tau^0_{ij} \sim 2$ ps. Note that this scattering time lies within typical orders of magnitude for ELO scattering.

For an illustration of the IFR scattering lifetimes with respect to ELO scattering consider Fig. 5.6. We show here calculated lifetimes for IFR and ELO scattering from the upper laser state (3) into the lower laser state (2) for a number of MIR QCLs, as reported by Chiu *et. al.* [106, 153]. The emission wavelength of devices covers the range $4.7 - 14.96\ \mu$m. We see that the contributions of interface roughness and electron-phonon

interaction to τ_3 are similar for short emission wavelengths ($< 6\ \mu$m). As the emission wavelength increases, the two-dimensional wavevector q_{32} reduces and IFR scattering becomes the dominant depopulation path of the upper laser level.

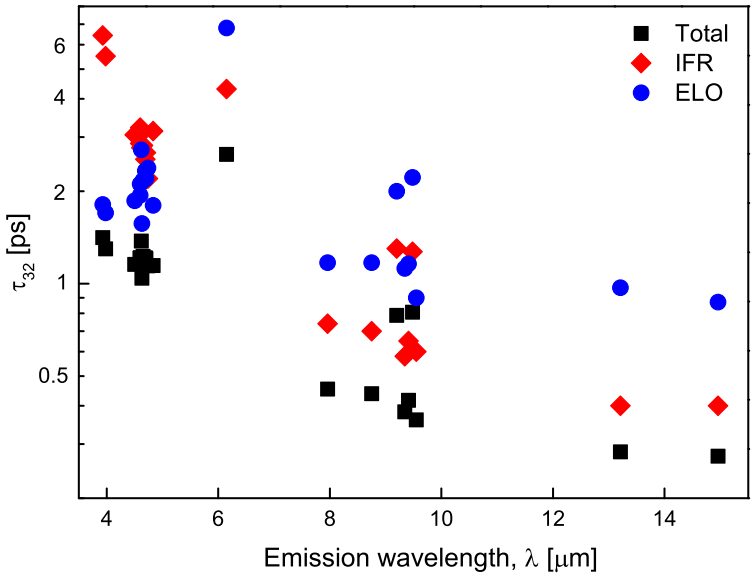

Figure 5.6: Calculated lifetimes for scattering from the upper into the lower laser state as a function of emission wavelength for several MIR QCLs. Data points correspond to values reported by Chiu *et. al.* [106, 153]. Solid squares represent the total scattering time. Diamonds (circles) represent the interface roughness (electron-phonon) scattering contribution to the total scattering time.

So far we have considered IFR scattering for an electron initially at the subband bottom. To include temperature-dependence we need to generalize Eq. 5.7 in order to include electrons with higher kinetic energy. We do this extending Eq. 5.7 to include energy (E)-dependence via the two dimensional vector $q_{ij}^2(E)$:

$$\frac{1}{\tau_{ij}^{IFR}(E)} = \frac{\pi m_c}{\hbar^3}\Delta^2\Lambda^2\sum_l \left[\delta U(z_l)\xi_i(z_l)\xi_j(z_l)\right]^2 \exp\left(\Lambda^2 q_{ij}^2(E)/4\right), \tag{5.8}$$

Using the variable substitution $\Delta E = E - E_i$ and $E_{ij} = E_i - E_j$, the wavevectors squared for electrons in band i and j are written as $q_i^2 = 2m^*/\hbar^2\Delta E$ and $q_j^2 = 2m^*/\hbar(\Delta E + E_{ij})$, respectively. The energy-dependent IFR scattering rate is then rewritten as:

$$\frac{1}{\tau_{ij}^{IFR}(\Delta E)} = (\tau_{ij}^{0})^{-1}\left[\exp\left(\left[\left(\frac{\Delta E}{E_{ij}}\right)^{2}+\frac{\Delta E}{E_{ij}}\right]^{1/2}-\frac{\Delta E}{E_{ij}}\right)\right]^{\frac{m^{*}\Lambda^{2}E_{ij}}{\hbar^{2}}} . \qquad (5.9)$$

For $\Delta E = 0$, this expression collapses to the energy-independent expression (Eq. 5.7).

As the electron temperature increases and higher electronic states are populated, the scattering rate $1/\tau_{ij}^{IFR}(\Delta E)$ increases by the virtue of a reduced $q_{ji}(E)$ (compare with Fig. 5.5). The values of $q_{ji}(E)$ converge as $E \to \infty$, leading to a temperature dependence of $1/\tau_{ij}^{IFR}(\Delta E)$. This effect can be estimated evaluating the limit $\tau_{ij}^{0}/\tau_{ij}^{IFR}(\Delta E \to \infty)$, which is shown in Fig. 5.7 for different values of E_{ij}. For the states pair (i, j) of Fig. 5.5, the ratio $\tau_{ij}^{0}/\tau_{ij}^{IFR}$ converges to a value of ~ 8.0 for $E \to \infty$.

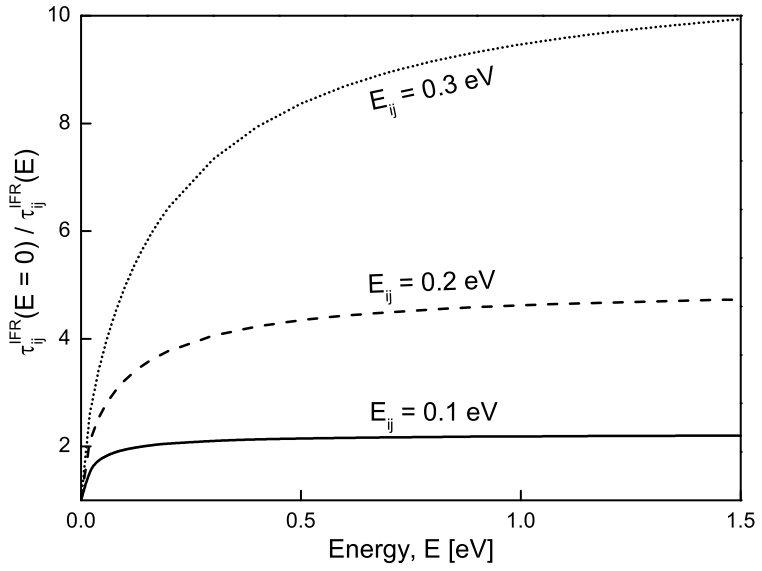

Figure 5.7: Calculated ratio of the energy-dependent IFR scattering rate to the energy-independent case for several intersubband energy separations E_{ij}.

5.1.3 Other scattering mechanisms

Electron-electron interaction

Electron-electron interaction is a many-body effect and represents the dominant contribution to intrasubband scattering, with scattering rates at least two orders of magnitude larger than intersubband scattering rate. The fast redistribution of electrons within a subband by means of electron-electron scattering justifies furthermore the assumption of thermalized electron subbands [154].

Intersubband (Auger-type) scattering processes are possible via carrier-carrier scattering. Furthermore, close examination of typical lifetimes shows that intersubband electron-electron scattering is relevant only for subband energy separations below the LO-phonon energy, for example between injector miniband states or in electron states in a THz QCL [68, 146, 154, 155]. We ignore therefore in the following electron-electron scattering in our analysis of intersubband scattering rates, as we focus on states with relatively large intersubband spacings (> 100 meV).

Impurity scattering

This scattering mechanism originates from the dopants in the laser structure. QCL injector regions are usually n-doped with Si in order to control electron density and avoid conduction band bending. Ionized donor atoms represent potential Coulomb scatterers. This background ions charge density is located in the injector regions, far away from the active region in order to prevent impurities from influencing the optical transition between upper and lower laser state [156]. The net result of ionized impurity scattering is a reduction of the lifetime of the injector states and an increased radiative transition broadening [155, 156, 157].

5.2 Temperature activated leakage current

In this section we analyze in more detail the temperature-driven leakage current (defined in Eq. 3.10) in MIR QCLs. We presents methods for the experimental determination of J_{leak} at and above threshold. This current is then modeled considering the temperature-dependent carrier distribution in the subbands, the LO-phonon probability, and interface roughness-induced scattering. As a result we find out that the main component of J_{leak} is due to carriers leakage from the injector states miniband into the excited states miniband. We discuss also impact of J_{leak} on QCLs performance.

5.2.1 Leakage current at laser threshold

Investigated QCL structures

The investigated QCL designs (structures S1 and S2) in this section are devices emitting in the MIR range. A portion of the conduction band profile of the first design, referred in the following as structure S1, is shown in Fig. 5.8. Layers composition and thickness are indicated. In order to reduce the temperature-driven carriers leakage, large energy separations between the injector miniband states and higher states are achieved in this structure (Tab. 5.1).

The active region of structure S1 exploits the dependence of the interface roughness-induced (IFR) scattering rate on the barrier height ($\delta U(z_l)$ in Eq. 5.7) in order to enhance population inversion. The IFR scattering component of the lifetime of specific states is engineered by using different barrier heights within a strain-compensated InGaAs/InAlAs-AlAs QCL. In particular, low barriers are used where the upper laser state has its highest probability, maximizing the lifetime of the upper laser state. Similarly, higher barriers are used where the lower laser state and the few subsequent confined states have their highest probabilities, minimizing the lifetime of the lower laser state. By combining differing barrier heights in this way, the lifetime of the upper laser state is increased, while simultaneously the lifetime of the lower laser state is decreased; thus, the population inversion is significantly enhanced.

Structure	$E_3 - E_2$	$E_3 - E_{g_1}$	$E_{m_1} - E_3$	$E_{m_2} - E_3$
S1	300	14	120	176
S2	271	11	80	139

Table 5.1: Energy differences of subband minima for structures S1 and S2 (in meV) obtained following intersubband spacing calculations. For a schematic representation of the energy levels see Fig. 5.8 and 5.11.

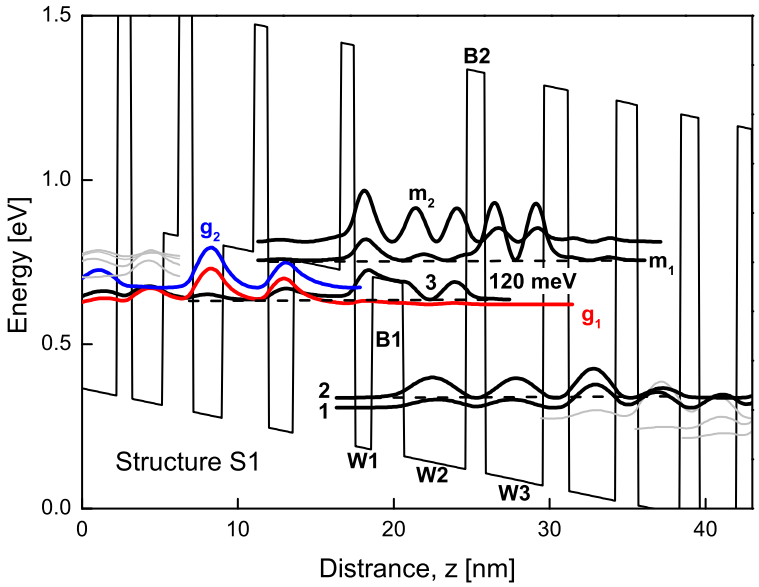

Figure 5.8: Calculated portion of the conduction band profile of the structure S1 under a 100 kV/cm electric field. The layer thickness in nm starting from the thinnest well, W1: 1.1/**2.0**/4.0/**1.2**/3.7/**1.6**/3.0/**1.4**/2.7/**1.2**/2.4/**1.0**/2.3/**0.9**/2.0/**1.9**/1.9/**2.9**/1.6/**3.9**. The strained $In_{0.73}Ga_{0.27}As$ well layers are in roman, and the strained digital-alloy InAlAs layers (composed of $In_{0.52}Al_{0.48}As$ and AlAs) layers are in bold. Underlined layers are doped to 1.0×10^{18} cm^{-3}. Solid lines represent the moduli-squared of relevant conduction band states. Relevant states are labeled in analogy to Fig. 3.3.

In order to investigate the effect of the reduced IFR scattering between upper and lower laser states we compare the luminescence spectra of structure S1 with a reference design [76]. The transition broadening due to IFR scattering between upper and lower laser states, described by the envelope wave functions ξ_3 and ξ_2, respectively, is given by

[152, 158, 159]:

$$\Gamma^{IFR} = \frac{\pi m^*}{\hbar^3}\Delta^2\Lambda^2\sum_l \delta U^2(z_l)\left[\xi_3^2(z_l) - \xi_2^2(z_l)\right]^2 , \tag{5.10}$$

where the sum is calculated across all the interfaces, l. The different variables in this equation were already defined in Eq. 5.7.

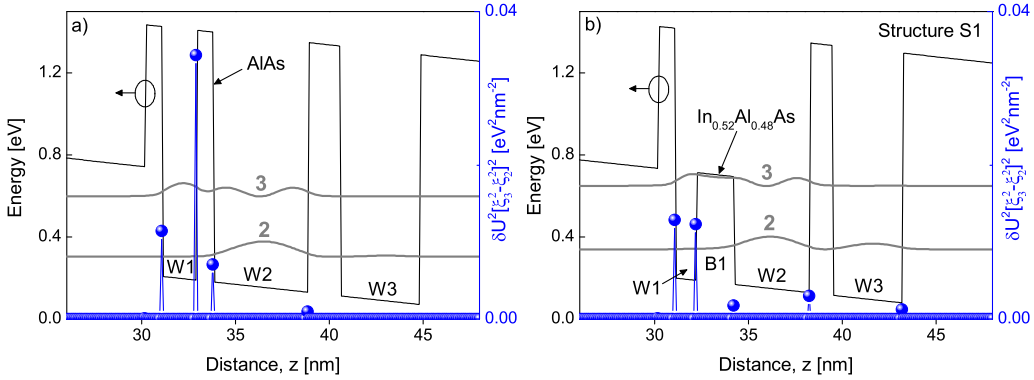

Figure 5.9: Illustration of the impact of individual interfaces on the interface roughness transition broadening between upper (3) and lower (2) laser states for a reference design (a) and for structure S1 (b). The term $\delta U^2(z_l)[\xi_3^2(z_l) - \xi_2^2(z_l)]^2$ of Eq. 5.10 is represented with blue dots.

Figure 5.9 plots the term $\delta U^2(z_l)[\xi_3^2(z_l) - \xi_2^2(z_l)]^2$, calculated for the scattering between upper (3) and the lower (2) laser states for structure S1 and for the reference design. We see that the impact of the barrier width B1 on the total scattering rate. In structure S1 (Fig. 5.9b), this impact is very modest, while the same calculation made for the reference design (Fig. 5.9a) indicates that the largest contribution to the interface scattering comes from the scattering on the thin and high AlAs barrier between W1 and W2 that is in place of B1. The term $\sum_l \delta U^2(z_l)[\xi_i^2(z_l) - \xi_j^2(z_l)]^2$ in Eq. 5.10 is calculated to 0.031 $\text{eV}^2\text{nm}^{-2}$ for structure S1 and 0.054 $\text{eV}^2\text{nm}^{-2}$ for the reference design, predicting an improvement in the transition width of the order of 43%.

Figure 5.10 shows the emission spectrum for a 25 μm $\times$ 3 mm laser stripe at various drive currents. The laser and electroluminescence emission is peaked at 2575 cm^{-1} (3.9 μm). The inset shows the half-width of the emission spectrum as a function of drive

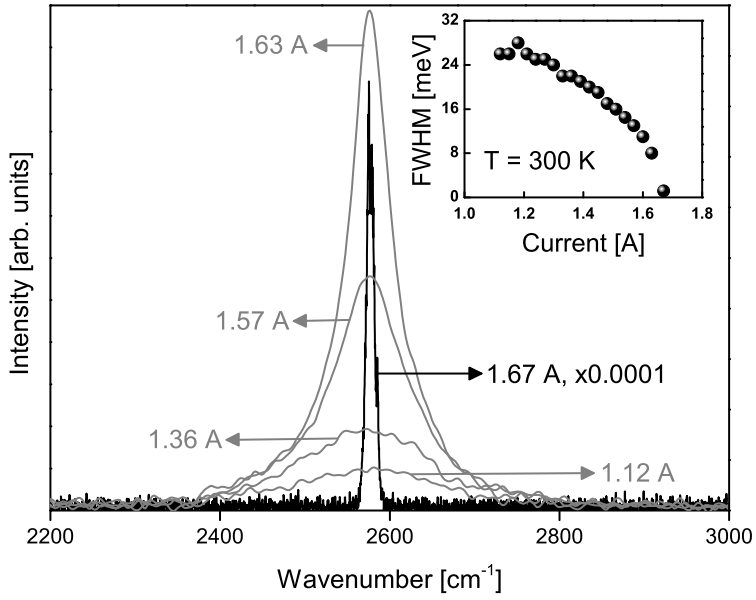

Figure 5.10: Measured emission spectrum as a function of the drive current for a 25 μm $\times$ 3 mm laser stripe at room temperature measured with 100 ns current pulses at a repetition rate of 10 kHz. The inset shows the half-width of the emission spectrum as a function of drive current, saturating at 26 meV as the current is reduced. Measured in the same way electroluminescence half-width at 80 K saturates at approximately 20 meV.

current. The half-width of the electroluminescence saturates for low drive current at $\sim$26 meV, so we consider it to be a fair approximation of the true width of the spontaneous emission free from the impact of stimulated emission. Measured in the same way, the electroluminescence half-width measured at 80 K saturates at $\sim$20 meV for the current design and $\sim$42 meV for the reference design. The $\sim$50% narrowing of the low-temperature electroluminescence spectrum in current design is mainly due to reduced interface scattering of the upper laser state at the B1 barrier, which is in good agreement with the calculated value of 43%. A rough estimate of the $\Delta\Lambda$ product in Eq. 5.10 from the low-temperature linewidth of 20 meV is [55]

$$\Delta\Lambda \approx 0.6\ \mathrm{nm}^2\ , \tag{5.11}$$

a value that is close to reported values for solid source epitaxial systems [158, 159]. This

value for $\Delta\Lambda$ is in the following used for our analysis of IFR scattering.

Structure S2 (Fig. 5.11) is similar to structure S1, though especially designed to enhance the thermal escape current by means of a reduced activation energy. For this purpose, energy separations $E_{3m_1} = 80$ meV and $E_{3m_2} = 139$ meV are achieved in structure S2, representing reduced values with respect to structure S1 (Tab. 5.1). This results in an increased carriers leakage from the injector into higher states via LO-phonon absorption and IFR scattering. Furthermore, other leakage mechanisms are simultaneously increased in structure S2. The direct injection of charge carriers from the injector ground state into lower laser states via LO-phonon emission, for example, will be in the longer-wavelength structure S2 (4.6 μm) larger with respect to the shorter wavelength structure S1 (3.9 μm).

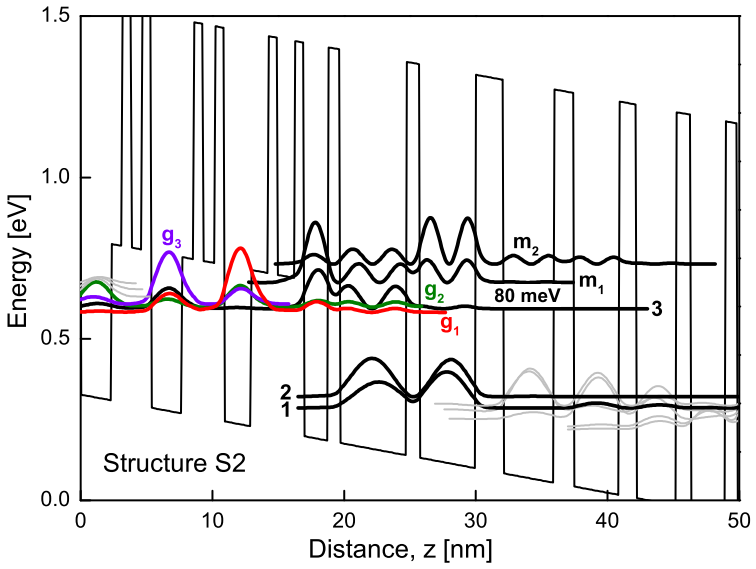

Figure 5.11: Calculated conduction band profile of the structure S2 under a 76 kV/cm electric field. The layer thickness in nm from left to right starting from the widest active region quantum well are 5.0/**1.0**/4.2/**2.1**/3.8/**1.5**/3.4/**1.3**/3.0/**1.1**/2.6/**0.9**/2.3/*0.8*/**0.7**/*0.8*/**0.7**/2.3/*0.9*/**0.7**/*0.9*/**0.7**/2.0/*1.3*/**0.7**/*1.3*/**0.7**/1.8/**0.9**. AlAs layers are in bold, $In_{0.73}Ga_{0.27}As$ layers are in roman, and $In_{0.55}Al_{0.45}As$ layers are in italics. Underlined layers are doped to 1.0×10^{18} cm^{-3}. Solid lines represent the moduli-squared of relevant conduction band states. Relevant states are labeled in analogy to Fig. 3.3.

Measurement of the leakage current

To experimentally determine $J_{leak}(T)$, the leakage current at laser threshold as a function of temperature, we measure the threshold current density J_{th} as a function of cavity length L and temperature. We use for simplicity laser bars with uncoated facets, resulting in a mirror loss $\alpha_m = -\ln(R_f)/L$, with R_f the facet reflectivity. From a plot of $J_{th}(1/L)$ and using Eq. 3.12, we determine the slope $-\ln(R_f)/g_c$. The mirror reflectivity $R_f \approx 0.26$ is determined by the mode spacing [57], so g_c is also known. The y-axis intercept of the $J_{th}(1/L)$ plot, $J_{th}(1/L=0) = (J_{leak} + \alpha_w/g_c)$, is the extrapolated threshold current density for perfectly reflecting mirrors. Furthermore, the waveguide loss α_w can be calculated for the emission wavelength, doping, temperature, and refractive index [129]. Then, the leakage current is written as

$$J_{leak}(T) = J_{th}(T, 1/L=0) - \alpha_w(T)/g_c(T) \tag{5.12}$$

for each temperature. Figure 5.12 shows the measured $1/L$-dependence of J_{th} for structures S1 and S2 at different temperatures. The correspondent values for g_c and for $g_c \cdot J_{th}(T, 1/L=0) = \alpha_w + J_{leak} \cdot g_c$ are plotted in Fig. 5.13.

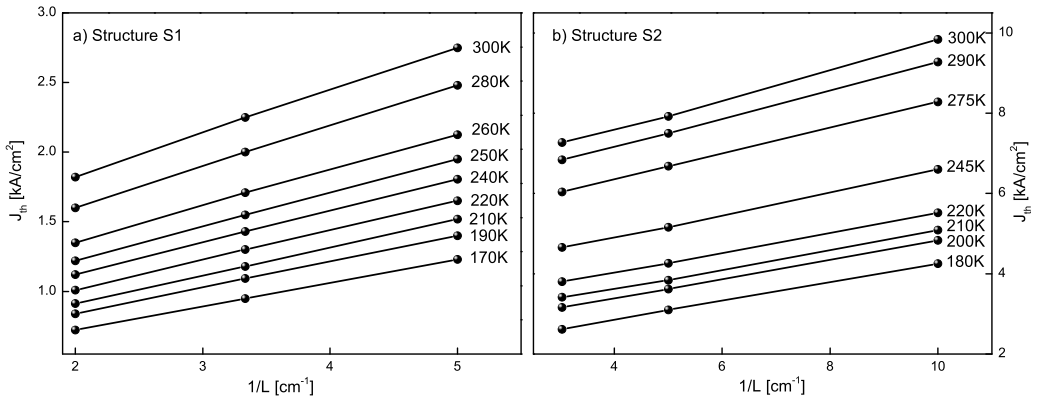

Figure 5.12: Measured threshold current density for structures S1 (a) and S2 (b) as a function of reciprocal resonator length at different heat sink temperatures. The devices were operated with 100 ns current pulses at 100 Hz repetition rate (0.001% d.c.). The solid lines illustrate the expected linear $1/L$-dependence of J_{th}.

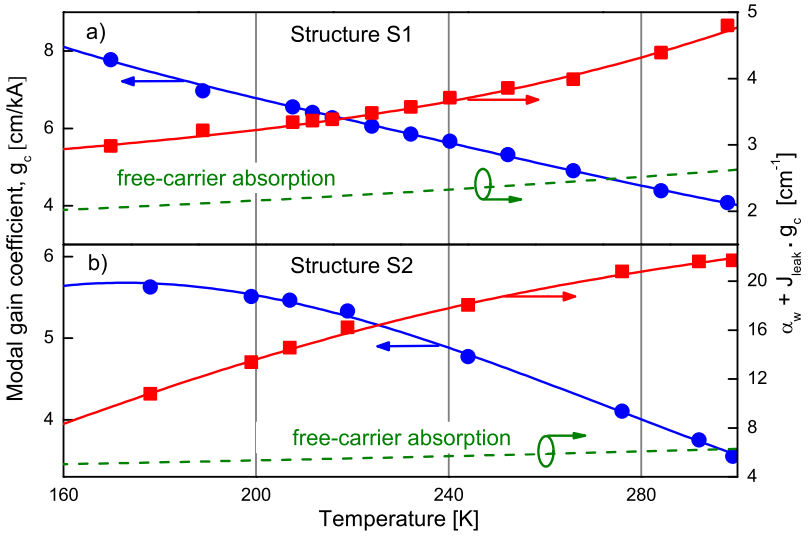

Figure 5.13: Measured modal gain coefficient g_c (blue circles) and $\alpha_w + J_{th}^{esc}(T) \cdot g_c$ (red squares) for structures S1 (a) and S2 (b) as a function of heat sink temperature. The solid lines represent polynomial fits to the data. The calculated waveguide loss α_w due to free-carrier absorption is also shown (dashed lines).

The leakage current can also be written as $J_{leak} = J_{th} - J_{th}^0$, where J_{th}^0 represents the threshold current density for zero-leakage, i.e., $J_{th}^0 = (\alpha_m + \alpha_w)/g_c$. The temperature dependence of J_{th}^0 is shown in Fig. 5.14. For structure S1 the ratio J_{leak}/J_{th} reaches small values $J_{leak}/J_{th} \approx 0.24$ for a 25 μm $\times$ 3.0 mm sample at 300 (Fig. 5.14a). A value of $J_{leak}/J_{th} \approx 0.15$ at 300 K was estimated for conventional three quantum well QCL structures [92, 103]. In the case of structure S2 J_{leak} achieves higher values over the temperature scale (Fig. 5.14b). A ratio $J_{leak}/J_{th} \approx 0.6$ is measured for a 25 μm $\times$ 3.3 mm sample at 300 K.

The correspondent values for the leakage current are shown in Fig. 5.15. Here we include also best fits to the data for J_{leak} as a function of temperature (solid black lines). These data were obtained using the correspondent expressions for ELO and IFR scattering (sections 5.1.2 and 5.1.1) and using the sheet concentrations of the injector states, n_{g_i}, as fitting parameters. For this purpose we write the leakage current as

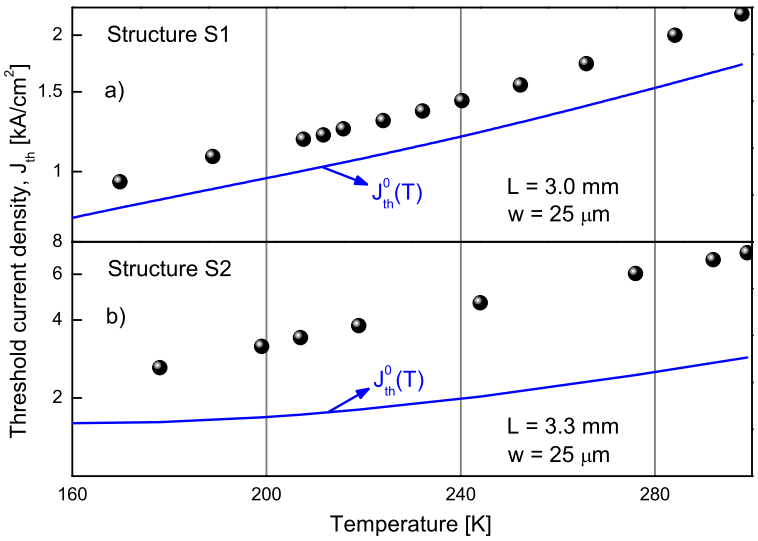

Figure 5.14: Measured threshold current density (solid dots) for QCL structures S1 and S2 as a function of heat sink temperature. The devices were operated with 100 ns current pulses at 100 Hz repetition rate (0.001% d.c.). The solid lines represent the expected threshold current density without the thermally activated leakage current.

$$J_{leak} = J_{leak}^{IFR} + J_{leak}^{ELO} \,, \tag{5.13}$$

where each contribution (due to electron-phonon and interface roughness-induced stattering) is the sum of individual components

$$J_{leak}^{IFR/ELO} = \sum_{g_i} J_{g_i}^{IFR/ELO} \,, \tag{5.14}$$

which include in turn two types of contributions (see also Eq. 3.10): carriers leakage from the injector states g_i into excited states miniband m_j, and carriers leakage from injector states g_i into the lower laser state 2:

$$J_{g_i}^{IFR/ELO} = e n_{g_i} \times \left(\sum_{m_j} \langle 1/\tau_{g_i m_j}^{IFR/ELO} \rangle (T) + \langle 1/\tau_{g_i 2}^{IFR/ELO} \rangle (T) \right) \,. \tag{5.15}$$

The temperature dependence of the scattering rates arises when averaging over the subband distribution using Fermi-Dirac statistics. The electron temperature, determined

from the measured current densities (Eq. 2.23) is considered for calculations.

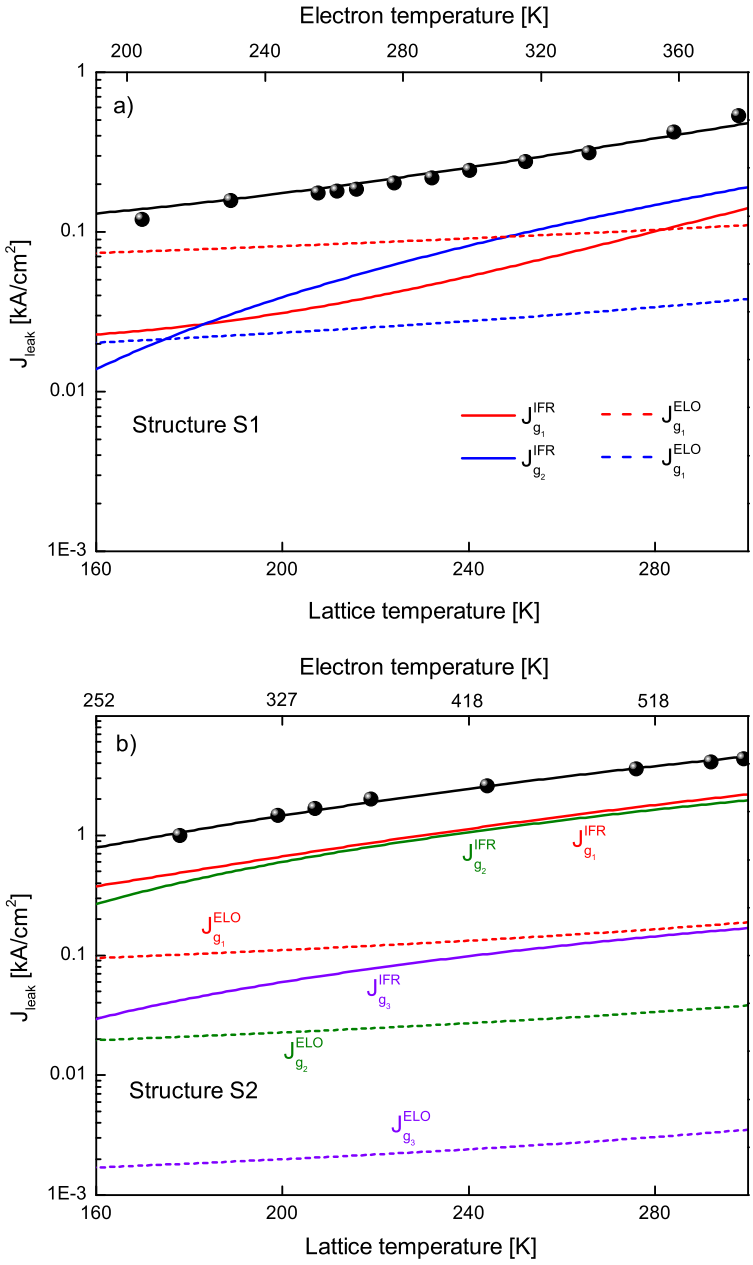

Figure 5.15: Measured leakage current density at threshold (solid dots) for structures S1 (a) and S2 (b). Solid (dashed) lines represent calculated components of the leakage current density due to interface-roughness (electron-phonon) scattering. The index g_i labels injector miniband states in analogy to Fig. 3.3. J_{g_i} represents the leakage current component for electrons scattering out from state g_i.

The best fit to the data results in the sheet concentrations

$$n_{g_1} = 5.5 \pm 0.4 \times 10^{10}\ \mathrm{cm}^{-2}\ , \quad n_{g_2} = 1.9 \pm 0.2 \times 10^{10}\ \mathrm{cm}^{-2} \tag{5.16}$$

for structure S1, and

$$n_{g_1} = 1.2 \pm 0.15 \times 10^{10}\ \mathrm{cm}^{-2}\ , \quad n_{g_2} = 2.0 \pm 0.2 \times 10^{9}\ \mathrm{cm}^{-2}\ , \quad n_{g_3} = 1.0 \pm 0.1 \times 10^{9}\ \mathrm{cm}^{-2}\ , \tag{5.17}$$

for structure S2.

We learn from Fig. 5.15 that IFR scattering from the injector states into the excited states miniband represents the most significant contribution to carriers leakage for small (< 90) meV escape barriers. An example here is structure S2, where carriers leakage due to IFR scattering is, for high temperatures, by far larger than the ELO scattering component. In the case of structure S1, on the other hand, IFR and ELO scattering components of J_{leak} are similar. Reason for that is principally the larger energy spacing between the injector and the excited states miniband.

Leakage from the injector states g_i into the lower laser level represents a minor contribution to the leakage current J_{leak}. Consider Fig. 5.16, which shows several leakage paths for an electron in the injector ground state g_1 of structure S2, scattering either to the ground state of the excited states miniband, m_1, or to the lower laser state, 2. The individual components of the correspondent current densities are shown in Fig. 5.17. We see that each component of the leakage current increases with temperature. This general trend is related to the increasing phonon number, which affects directly ELO scattering, and to the widening of the subband distribution broadening, which has an impact on both ELO- and IFR scattering. Furthermore, IFR scattering remains larger than ELO scattering and this holds for both transitions (from state g_1 into state m_1, labeled with e, and from state g_1 into 2, labeled with b). ELO scattering is dominated by phonon emission into state 2.

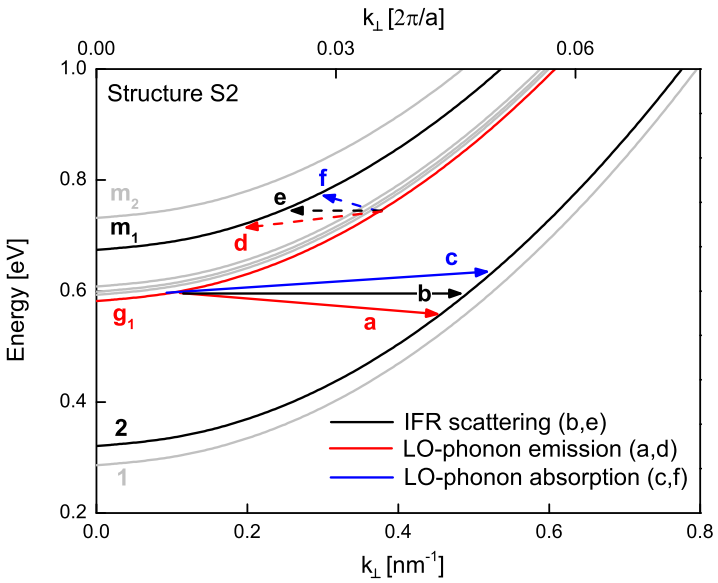

Figure 5.16: Calculated energy dispersion for the electronic states of Fig. 5.11. Arrows represent leakage current paths from state g_1 into states m_1 and 2. States are labeled in analogy to Fig. 5.11.

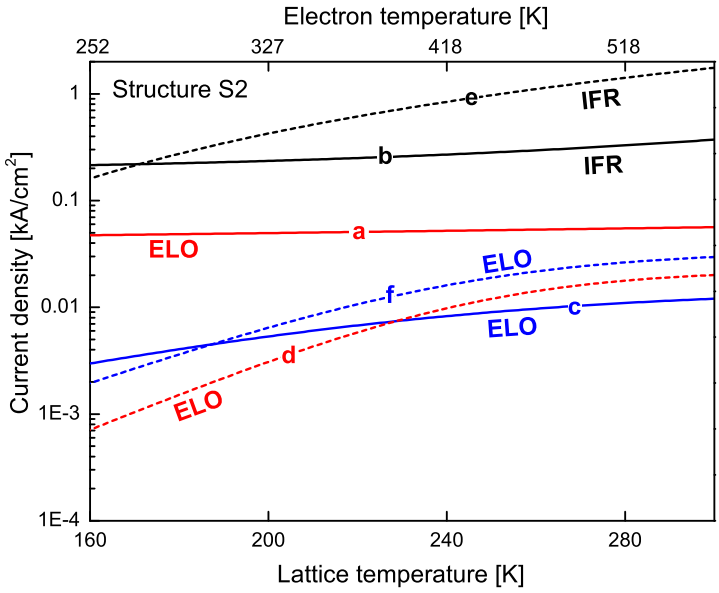

Figure 5.17: Calculated current density for non-radiative scattering from state g_1 into states m_1 (dashed lines) and 2 (solid lines) for the QCL structure of Fig. 5.11. Current paths are labeled as in Fig. 5.16.

Impact of temperature activated leakage current on T_0

An effective method to reduce carriers leakage into higher states is to increase the energy separation ΔE between the injector and the excited states miniband. This arises from the inverse exponential dependence of the leakage current $\sim \exp(-\Delta E/k_B T)$ on ΔE, which is characteristic for scattering due to LO-phonons and for IFR scattering as well [57, 92, 99, 100, 107, 160]. ΔE can be therefore used as a reference magnitude to qualitative estimate the significance of temperature activated carriers leakage in QCLs.

Figure 5.18 shows measured values for the threshold current characteristic temperature T_0 as a function of calculated ΔE for structures S1, S2, and variations. An approximately linear scaling of T_0 with ΔE is observed.

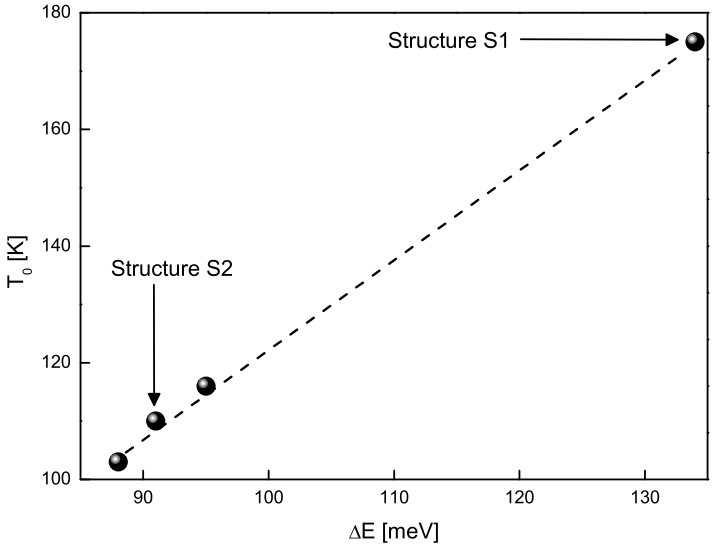

Figure 5.18: Measured threshold current characteristic temperature T_0 as a function of calculated ΔE for structures S1, S2, and variations. ΔE is the energy separation between the lowest injector miniband state and the lowest excited miniband state. The dashed line is a guide for the eye.

Similarly, as the photon energy of QCL devices increases the upper laser state energy level is pushed up in energy. The net effect is a reduction of ΔE and, therefore, an increase of temperature-driven leakage. Fig. 5.19 shows collected literature data for T_0 as a function of emission photon energy for a number of MIR QCLs using the In-

GaAs/InAlAs heterosystem. The reduction of T_0 with increasing photon energy can be clearly recognized.

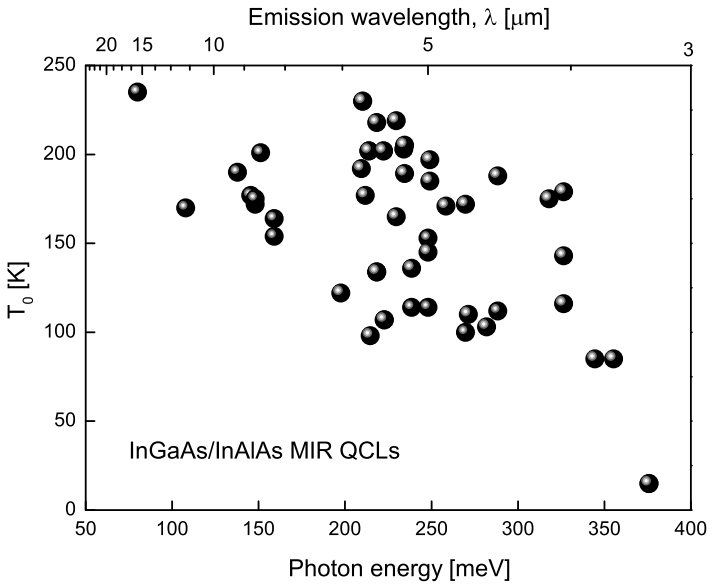

Figure 5.19: Measured threshold current characteristic temperature T_0 as a function of photon energy for several MIR QCLs. Data correspond to devices grown by our research group and from Ref. [36, 44, 46, 76, 110, 111, 112, 113, 114, 118, 119, 122, 131, 132, 138, 161, 162, 163, 164, 165, 166].

5.2.2 Leakage current above laser threshold

Investigated QCL structure

For our study of the temperature activated leakage current above threshold we use a MIR QCL design realized on the InGaAs/InAlAs-AlAs material system strain compensated to an InP substrate. This structure uses AlAs exit barriers in order to increase the energy difference between the injector ground state and the excited states miniband, which is calculated to $\Delta E = 106$ meV (Fig. 5.20). The AlAs barriers reduce also the spacial overlap between the excited states miniband and the quasi-continuum states, reducing carriers leakage further [55, 103, 120, 132, 133]. The intersubband energy difference between upper and lower laser states is 229 meV ($\lambda = 5.4\ \mu$m).

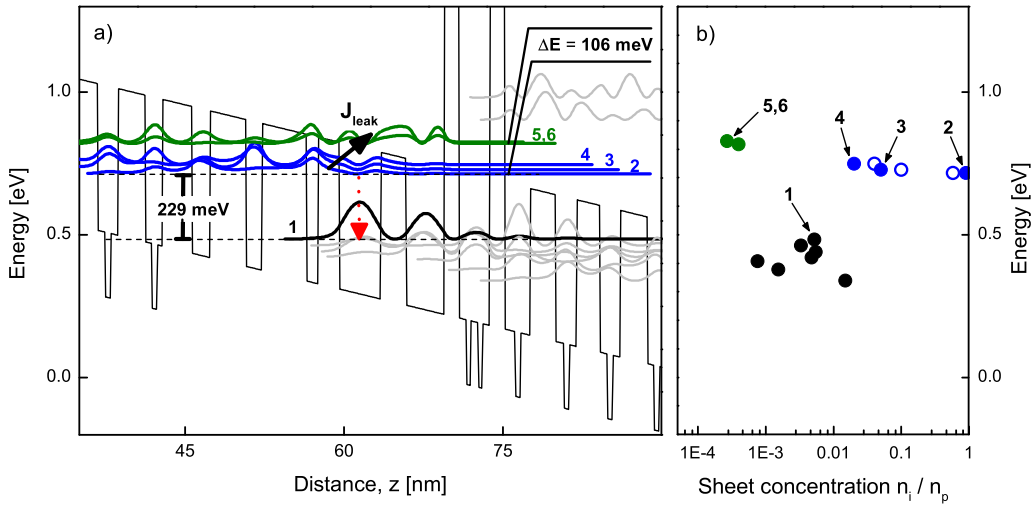

Figure 5.20: Calculated portion of the conduction band profile of the studied QCL structure under a 90 kV/cm electric field (a). Layer composition and thickness are indicated in the original publication [59]. Solid lines represent the modulisquared of relevant conduction band states. The dashed red arrow represents the radiative transition, corresponding to an emission wavelength of 5.4 μm. The solid arrow in (a) represents the leakage current from the upper laser state miniband into excited states. The right panel (b) shows the calculated two-dimensional sheet densities n_i for a heat sink temperature of 80 K and an electron temperature of $T_e = 130$ K (solid circles). These data are given in terms of the doping per period $n_p = 3.2 \times 10^{11}$ cm^{-2}. The open circles in the right panel (b) are the sheet densities for the states $i = 2$, 3, and 4 as determined by fitting the leakage current for higher electron temperatures.

The calculated two-dimensional sheet densities for active region confined states are shown in Fig. 5.20b. These data are obtained through a self-consistent calculation of the rate equations using a phenomenological model for scattering rates calculation. This model consists on writing the total intersubband scattering rate between two states i and j as the product of an energy-dependent part and the exchange integral of the wavefunctions squared of the involved states:

$$\frac{1}{\tau_{ij}} = \rho(E_{ij}) \int \xi_i^2(z)\xi_j^2(z)\mathrm{d}z \,. \tag{5.18}$$

E_{ij} is here the energy separation between the involved subbands and the energy dependent factor $\rho(E_{ij})$ collects contributions arising from several scattering mechanisms.

Within this approach, the part of the scattering rate that depends on the details of the wavefunctions, electric field, and specific structure is contained within $\int \xi_i^2(z)\xi_j^2(z)\mathrm{d}z$. The exchange integral in Eq. 5.18, multiplied by the energy-dependent factor $\rho(E_{ij})$, gives then the total non-radiative scattering rate. The factor $\rho(E_{ij})$ is reconstructed using experimental data[4]. The state of the art of this approach is that it allows the efficient calculation of several characteristics of MIR QCLs operating at a heat sink temperature of 80 K and electron temperatures up to $T_e = 130$ K. An extension to higher electron temperatures is being currently explored.

The QCL wafer containing 40 cascades was grown by GSMBE, processed into uncoated laser ridges of 25 μm width, and soldered epi-up onto Cu heat sinks. The heat sink temperature was kept constant to 80 K using a nitrogen-flow cryostat. Devices were operated with current pulses of 100 ns-width and a low (10 kHz, 1% d.c.) repetition rate in order to avoid self heating. Under these conditions, the threshold current density ranged from $J_{th} = 1.2$ kA/cm^2 for a $L = 10$ mm stripe to $J_{th} = 5.2$ kA/cm^2 for $L = 1$ mm. The high operation current densities of this device are particularly advantageous in this case in order to illustrate the role of the electron temperature on the leakage current.

Measurement of the leakage current and its impact on the quantum efficiency

For our analysis of the leakage current above threshold we want to take advantage of the resonator length L-dependence of the quantum efficiency η_d. Recalling section 3.2.3, we write this quantity as

$$\frac{1}{\eta_d} = \left(1 - \frac{\alpha_w}{\ln(R_f)\cdot L}\right)\frac{1}{\eta_t \eta_{inj}}\,. \tag{5.19}$$

For a fixed heat sink temperature, and neglecting the L-dependence of the injection efficiency, η_{inj}, this equation predicts a linear dependence of the reciprocal quantum efficiency $1/\eta_d$ on the the resonator length L. Such a dependence has been experimentally

[4]Details of this model are being prepared for publication.

verified for QCLs operating at low current densities and strong (~ 2.5 nm) dipole matrix elements. In those cases, the effect of carrier leakage can be neglected and $\eta_{inj} \approx 1$ can be used [107, 167]. Furthermore, the inclusion of the injection efficiency η_{inj} in the expression for η_d is necessary for QCLs operating at high current densities, as the QCL structure investigated in this section. As we will see next, this is necessary in order to guarantee an appropriate analysis of experimental data.

Measured values for $1/\eta_d$ as a function of L for the investigated QCL structure are shown in Fig. 5.21. Because the threshold current varies with L, the electron temperature T_e is also varied (Eq. 2.23). We see that for values of L between $5-10$ mm the measured $1/\eta_d$ follows a linear L-dependence, achieving a minimum value of $(1/\eta_d)_{\min} = 2.6$. For smaller values of L, $1/\eta_d$ increases considerably, achieving a value of $(1/\eta_d)_{\max} = 10.2$ for $L = 1$ mm.

The increasing $1/\eta_d$ with decreasing resonator length seen Fig. 5.21 is due to the effect of electron temperature on the leakage current (and, thus, on the injection efficiency η_{inj}). As noted above, shorter resonator lengths led to larger threshold currents and increased electron temperatures. Taking η_{inj} as the ratio of the fitted curve (solid line in Fig. 5.21) to the measured $1/\eta_d$, the leakage current can be found as function of T_e. Results are shown in Fig. 5.22.

As the heat sink temperature is maintained at cryogenic values during measurements, and the duty cycle is maintained low enough to neglect heating effects, there is practically no ELO scattering contribution to the leakage current. The measured leakage current is then driven by intersubband IFR scattering. For the studied QCL structure (Fig. 5.20), the total leakage current due to IFR roughness from the injector miniband states into higher states is given by

$$J_{leak}^{IFR} = J_2 + J_3 + J_4 \,, \quad \text{with } J_i = e \times \sum_{j\in\{5,6\}} n_i \langle 1/\tau_{ij}^{IFR}(E)\rangle(T_e) \,, \tag{5.20}$$

where e is the electronic charge and n_i is the two-dimensional sheet concentration in

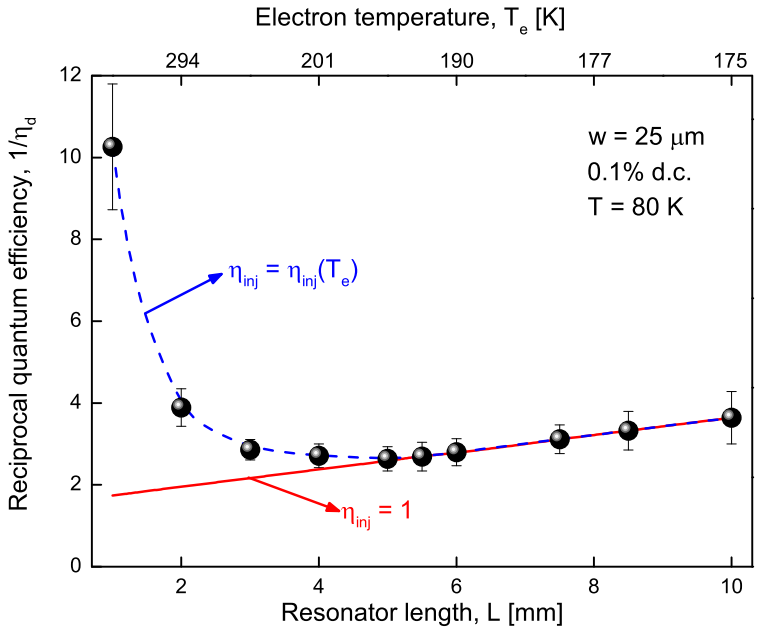

Figure 5.21: Measured reciprocal quantum efficiency per cascade $1/\eta_d$ (solid dots) as a function of resonator length L. The data are collected in pulsed mode (1% d.c.) at the heat sink temperature of 80 K. The solid red line represents the expected $1/\eta_d$ without the leakage current ($\eta_{inj} = 1$). The dashed line represents the calculated $1/\eta_d$ assuming an electron temperature-dependent injection efficiency $\eta_{inj} = \eta_{inj}(T_e)$. The upper axis shows the correspondent values for the electron temperature.

subband i.

The measured leakage current can be modeled using Eq. 5.20 with n_i as fitting parameters. Averaging over energy is done using Fermi-Dirac statistics. The best fit to the data results in the curves included in Fig. 5.22, which lead to the values $n_2 = (0.58 \pm 0.03)n_p$, $n_3 = (0.1 \pm 0.01)n_p$, and $n_4 = (0.04 \pm 0.0002)n_p$, with n_p the doping per period. Comparison of these values with respect to the calculated ones for a lower electron temperature (Fig. 5.20b) reveals an increment of $\sim 100\%$ for the sheet concentration of levels 3 and 4. This effect, as well as the reduction of the upper laser state population by $\sim 46\%$, is a directly consequence of the increased electron temperature.

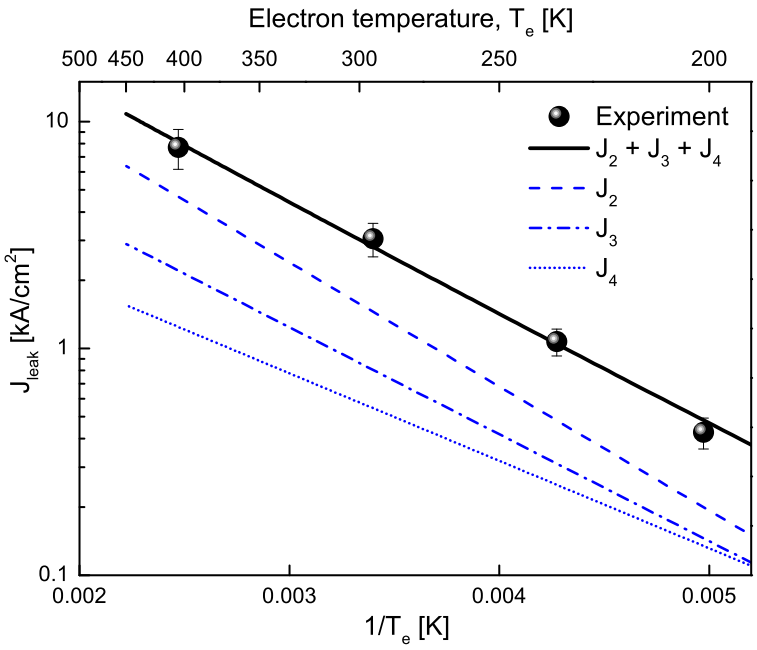

Figure 5.22: Measured leakage current density J_{leak} as a function of reciprocal electron temperature (solid dots). Resonator lengths between $L = 1.0 - 4.0$ mm, where the values of J_{leak} are significant (Fig. 5.21), are considered. The solid line is the current density as calculated using Eq. 5.20 for carriers leaving the injector miniband (states 2, 3, and 4 in Fig. 5.20) via interface roughness-induced (IFR) scattering. Individual components of this current are shown.

5.3 Summary

Temperature activated leakage of charge carriers affects QCL performance significantly. The main non-radiative scattering mechanisms in MIR QCLs are electron-longitudinal-optical-phonon (ELO) scattering and interface roughness-induced (IFR) scattering. The rate for both of them increases with temperature due to the increased phonon number and the broadening of the subband distribution. Carriers leakage from the injector ground states into the excited miniband is dominated by IFR scattering by intersubband energy spacings < 90 meV. Similarly, scattering from the upper laser state into the lower laser state is dominated by IFR scattering for emission wavelengths > 10 μm. We are able to measure the leakage current at and above laser threshold. This allows us to estimate the sheet distribution of conduction band states and better understand the impact of temper-

ature activated leakage on QCL characteristics. Our approach offers a straightforward method to analyze and troubleshoot thermally activated leakage in new QCL active region designs.

6 Outlook and conclusions

In this thesis we illustrated the key role of quantum-cascade lasers (QCLs) as coherent light sources for the mid- and far-infrared portion of the electromagnetic spectrum. Important aspects of two-dimensional charge carriers in semiconductor heterostructures were reviewed including the numerical calculation of steady state solutions and carrier statistics.

We discussed the general architecture and operation principle of mid-infrared QCLs. We presented expressions for the threshold current density and the differential quantum efficiency with consideration of the leakage current. We found out that the injection efficiency has a major impact in both the threshold current density and the quantum efficiency.

Fabrication steps, processing, mounting, and standard QCLs characterization methods were discussed. We presented a method for the fabrication of buried-heterostructure (BH) devices with high thermal conductivity using iron-doped indium-phosphide (InP:Fe) lateral cladding. The typical growth temperature of 650 °C required for metal-organic vapor-phase epitaxy (MOVPE) limits the suitability of this technique for regrowing InP:Fe in QCLs with a locally large internal strain. This is the case of a variety of short wavelength (3-5 μm) QCL designs based on strain-compensation of $In_xGa_{1-x}As$ wells and 12 nm-thick AlAs barriers on an InP-substrate. In our research, we used the gas-source molecular-beam epitaxy (GSMBE) technique to fabricate BH-QCLs using InP:Fe overgrown at temperatures < 600 °C. First realizations led to cw-operation up to 210 K of a 7 μm-wide BH-QCL with an emission wavelength of 5.4 μm. The measured thermal conductance was $C_{th} = 500$ W/Kcm^2 at 210 K and 1020 W/Kcm^2 at 127 K, which is

comparable to the state of the art BH-QCLs regrown using MOVPE.

We proposed a method for estimation of the thermal resistance as a function of temperature, which is based on fitting the measured light output power as a function of duty cycle and using the thermal conductance as a fitting parameter. This method allows the prediction of additional laser performance parameters as the maximum duty cycle and the maximum light output power. Such a straightforward method should prove very useful for rapid analysis strategies for laser performance optimization, particularly for maximizing the average power and for troubleshooting thermal management.

Carriers leakage from QCL quantum-well confined states into higher and lower states were discussed. The two main mechanisms for non-radiative intersubband scattering in MIR QCLs are electron-longitudinal-optical-phonon (ELO) scattering and interface roughness-induced (IFR) scattering. The rate for non-radiative intersubband scattering increases with temperature due to the increased phonon number and the broadening of the subband distribution. Carriers leakage from the injector ground states into the excited miniband is dominated by IFR scattering by intersubband energy spacings < 90 meV. We presented methods for the experimental determination of the leakage current in QCLs at and above laser threshold, which allowed us to estimate the sheet distributions of conduction band states and better understand the impact of temperature activated leakage on QCLs characteristics. In particular, we found that even at temperatures low enough to neglect ELO scattering, carriers leakage due to IFR becomes significant for devices operating at high electron temperatures. Altogether, this approach offers a straightforward method to analyze and troubleshoot new QCL active region designs and optimize their performance.

Bibliography

[1] H. Welker, *"Über neue halbleitende Verbundungen"*. Zeitschrift für Naturforschung 7a, 744 (1952).

[2] H. Welker, *"Über neue halbleitende Verbundungen II"*. Zeitschrift für Naturforschung 8a, 248 (1953).

[3] E. F. Schubert, *"Light emitting diodes"*. Cambridge University Press (2003).

[4] H. Rupprecht, M. Pilkuhn, and J. M. Woodall, *"Continuous stimulated emission from GaAs diodes at 77K"*. Proc. IEEE 51, 1243 (1963).

[5] J. I. Pankove and J. E. Berkeyheiser, *"A light source modulated at microwave frequencies"*. Proc. IRE 50, 1976 (1962).

[6] J. I. Pankove and M. J. Massoulie, *"Injection luminescence from GaAs"*. Bull. Am. Phys. Soc. 7, 88 (1962).

[7] R. N. Hall, G. E. Fenner, J. D. Kingsley, T. J. Soltyd, and R. O. Carlson, *"Coherent light emission from GaAs junctions"*. Phys. Rev. Lett. 9, 36 (1962).

[8] F. Capasso, *"Band-Gap Engineering: From Physics and Materials to New Semiconductor Devices"*. Science 235, 172 (1987).

[9] H. T. Grahn, *"Introduction to Semiconductor Physics"*. World Scientific (1999).

[10] I. Vurgaftman, J. R. Meyer, and L. R. Ram-Mohan, *"Band parameters for III-V compound semiconductors and their alloys"*. J. Appl. Phys. 89, 5815 (2001).

[11] S. Adachi, *"Handbook on Physical Properties of Semiconductors"*. Vol. 2, Springer US (2004).

[12] N. Jr. Holonyak. S. F. Bevacqua, C. V. Bielan, F. A. Carranti, B. G. Hess, and S. J. Lubovski, *"Electrical properties of Ga(AsP) p-n junctions"*. Proc. IEEE 51, 364 (1963).

[13] N. Jr. Holonyak. S. F. Bevacqua, C. V. Bielan, and S. J. Lubowski, *"The direct-indirect transition in Ga($As_{1-x}P_x$) p-n junctions"*. Appl. Phys. Lett. 3, 47 (1963).

[14] H. Rupprecht, J. M. Woodall, and G. D. Pettit, *"Efficient visible electroluminescence at 300K from AlGaAs pn junctions grown by liquid phase epitaxy"*. Appl. Phys. Lett. 11, 81 (1967).

[15] H. Rupprecht, J. M. Woodall, G. D. Pettit, J. W. Crowe, and H. F. Quinn, *"Stimulated emission from AlGaAs diodes at 77K"*. Quant. Elect. 4, 35 (1968).

[16] R. A. Loganm H. G. White, F. A. Trumbore, *"P-n junctions in GaP with external electroluminescence efficiencies $\sim$2% at 300K"*. Appl. Phys. Lett. 10, 206 (1967).

[17] J. I. Pankove, E. A. Miller, D. Richman, and J. E. Berkeyheiser, *"Electroluminescence in GaN"*. J. Luminescence 4, 63 (1971).

[18] I. Akasaki, H. Amano, K. Itoh, N. Koide, and K. Manabe, *"GaN based UV/blue light-emitting devices"*. Inst. Phys. Conf. Ser. 129, 851 (1992).

[19] S. Nakamura and M. Senoh, *"The blue laser diode"*. Springer, Berlin (1997).

[20] R. R. LaPierre, A. C. E. Chia, S. J. Gibson, C. M. Haapamaki, R. Yee, P. Kuyanov, J. Zhang, N. Tajik, N. Jewell, and K. M. A. Rahman, *"III-V nanowire photovoltaics: Review of design for high efficiency"*. Phys. Stat. Solidi RRL 7, 815 (2013).

[21] A. M. Munshi and H. Weman, *"Advances in semiconductor nanowire growth on graphene"*. Phys. Stat. Solidi RRL 7, 713 (2013).

[22] A. A. Kosterev, G. Wysocki, Y. A. Bakhirkin, S. So, R. Lewicki, F. K. Tittel, and R. F. Curl, *"Application of quantum cascade lasers to trace gas analysis"*. Appl. Phys. B 90, 165 (2008).

[23] M. Troccoli, L. Diehl, D. P. Bour, S. W. Corzine, N. Yu, C. H. Wang, M. A. Belkin, G. Höfler, R. Lewicki, G. Wysocki, F. K. Tittel, and F. Capasso, *"High-Performance Quantum Cascade Lasers Grown by Metal-Organic Vapor Phase Epitaxy and Their Applications to Trace Gas Sensing"*. J. of Light. Tech. 26, 3534 (2008).

[24] C. L. Schiller, H. Bozem, C. Gurk, U. Parchatka, R. Königstedt, G. W. Harris, J. Lelieveld, and H. Fischer, *"Applications of quantum cascade lasers for sensitive trace gas measurements of CO, CH_4, N_2O and HCHO"*. Appl. Phys. B 93, 419 (2008).

[25] F. K. Tittel, G. Wysocki, A. A. Kosterev, and Y. A. Bakhirkin, *"Semiconductor Laser Based Trace Gas Sensor Technology: Recent Advances and Applications"*. Springer NATO Science Series (2008).

[26] F. K. Tittel and R. Lewicki, *"Tunable mid-infrared laser absorption spectroscopy"*. Woodhead Publishing Ltd. (2013).

[27] F. K. Tittel, R. Lewicki, R. Lascola, and S. McWhorter, *"Emerging infrared laser absorption spectroscopic techniques for gas analysis"*. John Wiley & Sons, New York (2013).

[28] R. Lewicki, M. Jahjah, Y. Ma, P. Stefanski, J. Tarka, M. Razeghi, and F. K. Tittel, *"Current Status of Mid-Infrared Semiconductor Laser Based Sensor Technologies for Trace Gas Sensing Applications"*. SPIE Press (2013).

[29] R. Martini and E. A. Whittaker, *"Quantum cascade laser-based free space optical communications"*. J. Opt. Fib. Commun. Rep. 2, 279 (2005).

[30] Z. Bielecki, W. Kolosowski, and J. Mikolajczyk, *"Free-space optical data link using quantum cascade laser"*. PIERS Proceedings, Cambridge (US) (2008).

[31] M. Razegui, S. Slivken, Y. Bai, and S. R. Darvish, *"The quantum cascade laser: A versatile and powerful tool"*. OSA-OPN (2008).

[32] M. Gutowska, D. Pierscinska, M. Nowakowski, K. Pierscinski, D. Szabra, J. Mikolajczyk, J. Wojtas, and Z. Bielecki, *"Transmitter with quantum cascade laser for free space optics communications systems"*. Bull. of. Pol. Ac. of Sc. 59-4, 419 (2011).

[33] C. Gmachl, F. Capasso, D. L. Sivco, and A. Y. Cho, *"Recent progress in quantum cascade lasers and applications"*. Rep. Prog. Phys. 64, 1533 (2001).

[34] M. P. Semtsiv, G. G. Tarasov, W. T. Masselink, H. Kissel, and M. Woerner, *"Midinfrared intersubband absorption in strain compensated InGaP/InGaAs superlattices on (001) GaAs"*. Appl. Phys. Lett. 82, 3418 (2003).

[35] N. Georgiev, T. Dekorsy, F. Eichhorn, M. Heml, M. P. Semtsiv, and W. T. Masselink, *"Short-wavelength intersubband absorption in strain compensated InGaAs/AlAs quantum well structures grown on InP"*. Appl. Phys. Lett. 83, 210 (2003).

[36] M. P. Semtsiv, M. Ziegler, S. Dressler, W. T. Masselink, N. Georgiev, T. Dekorsy, and M. Helm, *"Above room temperature operation of short wavelength ($\lambda = 3.8\,\mu m$) strain-compensated $In_{0.73}Ga_{0.27}As$-AlAs quantum-cascade lasers"*. Appl. Phys. Lett. 85, 1478 (2004).

[37] W. T. Masselink, M. P. Semtsiv, S. Dressler, M. Ziegler, N. Georgiev, T. Dekorsy, and M. Helm, *"High-power short-wavelength quantum cascade lasers"*. Proc. SPIE Int. Soc. Opt. Eng. 5738, 13 (2005).

[38] M. P. Semtsiv, M. Ziegler, S. Dressler, W. T. Masselink, N. Georgiev, T. Dekorsy, and M. Helm, *"Strain-compensated AlAs/(In,Ga)As heterostructures for short-wavelength intersubband absorption and laser emission"*. J. Cryst. Growth 278, 526 (2005).

[39] M. P. Semtsiv, M. Ziegler, W. T. Masselink, N. Georgiev, T. Dekorsy, and M. Helm, *"Near infrared intersubband transitions in InGaAs-AlAs-InAlAs double quantum wells"*. J. Appl. Phys. 97, 113538 (2005).

[40] O. Drachenko, J. Galibert, J. Léotin, J. W. Tomm, M. P. Semtsiv, M. Ziegler, S. Dressler, U. Müller, and W. T. Masselink, *"Electron-optical-phonon interaction in the $In_{0.73}Ga_{0.27}As$ intersubband laser"*. Appl. Phys. Lett. 87, 072104 (2005).

[41] M. P. Semtsiv, S. Dressler, U. Müller, S. Knigge, M. Ziegler, and W. T. Masselink, *"Proton-implanted shallow-ridge quantum-cascade laser"*. IEEE J. Quantum Electron. 42, 490 (2006).

[42] M. P. Semtsiv, S. Dressler, W. T. Masselink, G. Fedorov, and D. Smirnov, *"Probing the population inversion in intersubband laser by magnetic field spectroscopy"*. Appl. Phys. Lett. 89, 171105 (2006).

[43] M. P. Semtsiv, U. Müller, W. T. Masselink, N. Georgiev, T. Dekorsy, and M. Helm, *"Intersubband transitions in GaP-AlP heterostructures"*. Appl. Phys. Lett. 89, 184102 (2006).

[44] M. P. Semtsiv, M. Wienold, S. Dressler, and W. T. Masselink, *"Short-wavelength ($\lambda \approx 3.3\mu m$) InP-based strain-compensated quantum-cascade laser"*. Appl. Phys. Lett. 89, 211124 (2006).

[45] M. P. Semtsiv, S. Dressler, and W. T. Masselink, *"Short-wavelength ($\lambda \approx 3.6\mu m$) $In_{0.73}Ga_{0.27}As$-AlAs/InP quantum-cascade laser"*. IEEE J. Quantum Electron. 43, 42 (2007).

[46] M. P. Semtsiv, M. Wienold, S. Dressler, and W. T. Masselink, *"Short-wavelength ($\lambda \approx 3.05\mu m$) InP-based strain-compensated quantum-cascade laser"*. Appl. Phys. Lett. 90, 051111 (2007).

[47] W. T. Masselink, M. P. Semtsiv, S. Dressler, M. Ziegler, and M. Wienold, *"Physics, growth, and performance of (In,Ga)As-AlAs/InP quantum-cascade lasers emitting at* $\lambda < 4\mu m$*"*. Phys. Stat. Sol. B 244, 2906 (2007).

[48] M. Wienold, M. P. Semtsiv, I. Bayrakli, W. T. Masselink, M. Ziegler, K. Kennedy, and R. Hogg, *"Optical and thermal characteristics of narrow-ridge quantum-cascade lasers"*. J. of Appl. Phys. 103, 083113 (2008).

[49] M. Wienold, M. P. Semtsiv, S. Dressler, W. T. Masselink, K. Potzger, S. Winnerl, and M. Heml, *"Fe-implantation for rear-facet coatings of InP-based quantum cascade lasers"*. Electron. Lett. 44, 293 (2008)

[50] M. P. Semtsiv, M. Wienold, S. Dressler, W. T. Masselink, G. Fedorov, and D. Smirnov, *"Intervalley carrier transfer in short-wavelength InP-based quantum-cascade laser"*. Appl. Phys. Lett. 93, 071109 (2008).

[51] L. K. Hoffmann, M. Klinkmüller, E. Mujagić, M. P. Semtsiv, W. Schrenk, W. T. Masselink, and G. Strasser, *"Three array quantum cascade laser"*. Opt. Express 17, 649 (2009).

[52] O. Fedosenko, M. Chashnikova, S. Machulik, J. Kischkat, M. Klinkmüller, A. Aleksandrova, G. Monastyrskyi, M. P. Semtsiv, and W. T. Masselink, *"InP-based mid-infrared quantum-cascade laser grown on pre-patterned wafer"*. J. Crys. Growth 323, 488 (2011).

[53] O. Fedosenko, M. Chashnikova, S. Machulik, J. Kischkat, M. Klinkmüller, A. Aleksandrova, G. Monastyrskyi, M. P. Semtsiv, and W. T. Masselink, *"Scalling the output power of quantum-cascade lasers with a number of cascades"*. J. Crys. Growth 323, 484 (2011).

[54] M. Chashnikova, G. Monastyrskyi, A. Aleksandrova, M. Klinkmüller, M. P. Semtsiv, and W. T. Masselink, *"Buried-heterostructure quantum-cascade laser overgrown by gas-source molecular-beam epitaxy"*. Appl. Phys. Lett. 100, 213504 (2012).

[55] M. P. Semtsiv, Y. Flores, M. Chashnikova, G. Monastyrskyi, and W. T. Masselink, *"Low-threshold intersubband laser based on interface-scattering-rate engineering"*. Appl. Phys. Lett. 100, 163502 (2012).

[56] J. Kischkat, S. Peters, B. Gruska, M. Semtsiv, M. Chashnikova, M. KlinkmL̈ler, O. Fedosenko, S. Machulik, A. Aleksandrova, G. Monastyrskyi, Y. Flores, and W. T. Masselink, *"Mid-infrared optical properties of thin films of aluminum oxide, titanium oxide, silicon oxide, aluminum nitride, and silicon nitride"*. J. of Appl. Opt. 51, 6789 (2012).

[57] Y. V. Flores, M. P. Semtsiv, M. Elagin, G. Monastyrskyi, S. Kurlov, A. Aleksandrova, J. Kischkat, and W. T. Masselink, *"Thermally activated leakage current in high-performance short-wavelength quantum cascade lasers"*. J. of Appl. Phys. 113, 134506 (2013).

[58] Y. V. Flores, G. Monastyrskyi, M. Elagin, M. P. Semtsiv, and W. T. Masselink, *"Analysis of thermally activated leakage current in a low-threshold-current quantum-cascade laser emitting at* 3.9 μm*"*. Proc SPIE 8640, 86401S (2013).

[59] Y. V. Flores, S. Kurlov, M. Elagin, M. P. Semtsiv, and W. T. Masselink, *"Leakage current in quantum-cascade lasers through interface roughness scattering"*. Appl. Phys. Lett. 103, 161102 (2013).

[60] Y. V. Flores, M. P. Semtsiv, M. Elagin, G. Monastyrskyi, S. Kurlov, A. Aleksandrova, J. Kischkat, and W. T. Masselink, *"Continuous-wave operation of a buried-heterostructure strain-compensated quantum-cascade laser overgrown by gas-source molecular beam epitaxy"*. J. of Cr. Growth 398, 40 (2014).

[61] G. Monastyrskyi, M. Elagin, M. Klinkmüller, A. Aleksandrova, S. Kurlov, Y. V. Flores, J. Kischkat, M. P. Semtsiv, and W. T. Masselink, *"Impact of heat dissipation on quantum cascade laser performance"*. J. of Appl. Phys. 113, 134509 (2013).

[62] W. T. Masselink, M. P. Semtsiv, M. Elagin, Y. V. Flores, G. Monastyrskyi, S. Kurlov, and J. Kischkat, *"Designs issues and physics for high-performance quantum-cascade lasers"*. Proc. SPIE 8898, 889805 (2013).

[63] J. Kischkat, M. P. Semtsiv, T. Wegner, M. Elagin, G. Monastyrskyi, Y. Flores, S. Kurlov, and W. T. Masselink, *"Design, fabrication, and applications of ultra-narrow infrared bandpass interference filters"*. Proc. SPIE 8896, 889614 (2013).

[64] M. P. Semtsiv, A. Aleksandrova, M. Elagi, G. Monastyrskyi, J.-F. Kischkat, Y. V. Flores, and W. T. Masselink, *"Semi-insulating InP:Fe for buried-heterostructure strain-compensated quantum-cascade lasers grown by gas-source molecular-beam epitaxy*. J. of Crys. Gr. 378, 125 (2013).

[65] S. S. Kurlov, Y. V. Flores, M. Elagin, M. P. Semtsiv, and W. T. Masselink, *"Phenomenological self-consistent scattering-rate model for simulation of mid-infrared quantum-cascade lasers"* J. of Appl. Phys. (in preparation).

[66] W. T. Masselink, M. P. Semtsiv, Y. V. Flores, S. Kurlov, M. Elagin, G. Monastyrskyi, J.-F. Kischkat, and A. Aleksandrova, *"AlAs/InAlAs-InGaAs QCLs grown by gas-source molecular-beam epitaxy"*. Proc. SPIE 9002, 90021A (2014).

[67] Y. V. Flores, S. Kurlov, M. Elagin, M. P. Semtsiv, and W. T. Masselink, *"The role of electron temperature in the leakage current in QCLs and its impact on the quantum efficiency"*. Proc. SPIE 9002, 90021R (2014).

[68] P. Harrison, *"Quantum Wells, Wires and Dots"*. 3rd Edition, Wiley, Chichester (2009).

[69] D. F. Nelson, R. C. Miller, and D. A. Kleinman, *"Band nonparabolicity effects in semiconductor quantum wells"*. Phys. Rev. B 35, 7770 (1987).

[70] S. Adachi, *"GaAs and Related Materials: Bulk Semiconducting and Supperlattice Properties"*. World Scientific, Singapore (1994).

[71] H. Asai and Y. Kawamura, *"Intersubband absorption in $In_{0.55}Ga_{0.47}As/In_{0.52}Al_{0.48}As$ multiple quantum-wells"*. Phys. Rev. B. 43, 4748 (1991).

[72] J. L. Robert and C. Bernard, *"The electron effective mass in heavily doped GaAs"*. J. Phys. C. 12, 2289 (1979).

[73] G. Bastard, *"Superlattice band structure in the envelope function approximation"*. Phys. Rev. B 24, 5693 (1981).

[74] G. Bastard, *"Wave Mechanics Applied to Semiconductor Heterostructures"*. Les Editions de Physique, Paris (1988).

[75] M. G. Burt, *"Fundamentals of envelope function theory for electronic states and photonic modes in nanostructures"*. J. Phys. Cond. Matt. 9, R53 (1999).

[76] M. P. Semtsiv, *"InGaAs-AlAs and InGaAs-InGaP strain-compensated heterostructures for short-compensated heterostructures for short-wavelength intersubband transitions and lasers"*. Ph. D. thesis, Humboldt-Universität zu Berlin (2004).

[77] C. G. Van de Walle, *"Bands lineups and deformation potentials in the model-solid theory"*. Phys. Rev. B. 39, 1871 (1989).

[78] M. P. Krijn, *"Heterojunction band offsets and effective masses in III-V quaternary alloys"*. Sem. Sci. Tech. 6, 27 (1991).

[79] F. H. Pollak and M. Cardona, *"Piezo-Electroreflectance in Ge, GaAs and Si"*. Phys. Rev. 172, 816 (1968).

[80] M. G. Burt, *"The justification for applying the effective-mass approximation to microstructures"*. J. Phys. Cond. Matt. 4, 6651 (1992).

[81] G. T. Einevoll and L. J. Sham, *"Boundary conditions for envelope functions at interfaces between dissimilar materials"*. Phys. Rev. B 49, 10533 (1994).

[82] I. Galbraith and G. Duggan, *"Envelope-function matching conditions for GaAs/(Al,Ga)As heterojunctions"*. Phys. Rev. 38, 10057 (1988).

[83] D. J. BenDaniel and C. B. Duke, *"Space-charge effects on electron tunneling"*. Phys. Rev. 152, 683 (1966).

[84] C. T. Kelley, *"Solving nonlinear equations with Newton's method"*. Fundamentals of Algorithms, SIAM (2003).

[85] T. J. Ypma, *"Historical development of the Newton-Raphson method"*. SIAM Rev. 37, 531 (1995).

[86] J. Spanier and K. B. Oldham, *"The unit-step u(x-a) and related functions"*. An Atlas of Functions 63, Washington DC (1987).

[87] J. Shah, *"Hot Carriers in Semiconductor Heterostructures"*, Academic Press, San Diego (1992).

[88] P. Harrison, *"The nature of electron distribution functions in quantum cascade lasers"*. Appl. Phys. Lett. 75, 2800 (1999).

[89] V. Spagnolo, G. Scamarcio, H. Page, and C. Sirtori, *"Simulataneous measurement of the elctronic and lattice temperatures in GaAs/$Al_{0.45}Ga_{0.55}As$ quantum-cascade lasers: Influence on the optical performance"*. Appl. Phys. Lett. 84, 3690 (2004).

[90] V. Spagnolo, G. Scamarcio, W. Schrenk, and G. Strasser, *"Influence of the band-offset on the electronic temperature of GaAs/Al(Ga)As superlattice quantum cascade lasers"*. Semicond. Sci. Technol. 19, 110 (2004).

[91] M. S. Vitiello, T. Gresch, A. Lops, V. Spagnolo, G. Scamarcio, N. Hoyler, M. Giovannini, and J. Faist, *"Influence of InAs, AlAs δ layers on the optical, electronic, and thermal characteristics of strain-compensated GaInAs/AlInAs quantum-cascade lasers"*. Appl. Phys. Lett. 91, 161111 (2007).

[92] D. Botez, S. Kumar, J. C. Shin, L. J. Mawst, I. Vurgaftman, and J. R. Meyer, *"Temperature dependence of the key electro-optical characteristics for midinfrared emitting quantum cascade lasers"*. Appl. Phys. Lett. 97, 071101 (2010).

[93] J. Faist, F. Capasso, D. L. Sivco, C. Sirtori, A. L. Hutchinson, and A. Y. Cho, *"Quantum cascade laser"*. Science 264, 553 (1994).

[94] R. F. Kazarinov, and R. A. Suris, Sov. Phys. Semicond. 5, 207 (1971); Fizika i Tekhnika Poluprovodnikov 5, 797 (1971).

[95] C. Gmachl, F. Capasso, A. Tredicucci, D. L. Sivco, A. L. Hutchinson, S. N. G. Chu, and A. Y. Cho, *"Noncascaded intersubband injection lasers at* $\lambda \approx 7.7$ *μm"*. Appl. Phys. Lett. 73, 3830 (1998).

[96] Y. Yao, A. J. Hoffman, and C. F. Gmachl, *"Mid-infrared quantum cascade lasers"*. Nat. Phot. 6, 432 (2012).

[97] C. Sirtori and R. Teissier, contribution in *"Intersubband transitions in quantum structures"*, McGraw-Hill (2006).

[98] Y. Flores, *"Thermally activated leakage current in high-performance short-wavelength quantum cascade lasers"*. M. Sc. thesis, Humboldt-Universität zu Berlin (2013).

[99] D. Botez, J. C. Shin, S. Kumar, L. J. Mawst, I. Vurgaftman, and J. R. Meyer, *"Electron leakage and its suppression via deep-well structures in 4.5- to 5.0-μm-emitting quantum cascade lasers"*. Opt. Eng. 49-11, 111108 (2010).

[100] C. Pflügl, L. Diehl, A. Lyakh, Q. J. Wang, R. Maulini, A. Tsekoun, C. Kumar N. Patel, X. Wang, and F. Capasso, *"Activation energy study of electron transport in high performance short wavelengths quantum cascade lasers"*. Optics Express 18, 746 (2010).

[101] D. Botez, J. C. Shin, S. Kumar, J. Kirch, C. Chang, L. J. Mawst, I. Vurgaftman, J. R. Meyer, A. Bismuto, B. Hinkov, and J. Faist, *"Temperature dependence of the key*

electro-optical characteristics for mid-infrared emitting quantum cascade lasers". Proc. SPIE 9753, 79530N (2011).

[102] Q. K. Yang, C. Schilling, R. Ostendorf, S. Hugger, F. Fuchs, and J. Wagner, *"Wall-plug efficiency of mid-infrared quantum cascade lasers"*. J. Appl. Phys. 111, 053111 (2012).

[103] D. Botez, J. C. Shin, J. Kirch, C. Chang, L. Mawst, and T. Earles, *"Multidimensional conduction-band engineering for maximizing the continuous-wave (cw) wallplug efficiencies of mid-infrared quantum cascade lasers"*. IEEE J. Sel. Top. Quantum Electron. 19-4, 1200312 (2013).

[104] P. Harrison and R. W. Kelsall, *"Population inversion in optically pumped asymmetric quantum well terahertz lasers"*. J. Appl. Phys. 81, 7135 (1997).

[105] J. Faist, *"Wallplug efficiency of quantum cascade lasers: Critical parameters and fundamental limits"*. Appl. Phys. Lett. 90, 253512 (2007).

[106] Y. T. Chiu, *"III-V semiconductor quantum well systems: Physics of GaAs two-dimensional hole systems and engineering of mid-infrared quantum cascade lasers"*. Ph. D. thesis, Princeton University (2013).

[107] A. Lyakh, R. Maulini, A. Tsekoun, R. Go, and C. Kumar N. Patel, *"Multiwatt long wavelength quantum cascade lasers based on high strain composition with* 70% *injection efficiency"*. Opt. Exp. 20, 24272 (2013).

[108] L. Schrottke, M. Giehler, M. Wienold, R. Hey, and H. T. Grahn, *"Compact model for the efficient simulation of the optical gain and transport properties in THz quantum-cascade lasers"*. Semicond. Sci. Technol. 25, 045025 (2013).

[109] P. M. Smowton and P. Blood, *"The differential efficiency of quantum-well lasers"*. IEEE J. Sel. Top. Quantum Electron. 3, 491 (1997).

[110] D. Hofstetter, M. Beck, T. Aellen, and J. Faist, *"High-power operation of distributed feedback quantum-cascade lasers at 5.3 μm"*. Appl. Phys. Lett. 78, 396 (2001).

[111] S. Blaser, D. A. Yarekha, L Hvozdara, Y. Bonetti, A. Muller, M. Giovannini, and J. Faist, *"Room-temperature, continuous wave, single-mode quantum-cascade lasers at* $\lambda \sim 5.4$ *μm"*. Appl. Phys. Lett. 86, 041109 (2005).

[112] J. S. Yu, A. Evans, S. Slivken, S. R. Darvish, and M. Razeghi, *"Temperature dependent characteristics of* $\lambda \sim 3.8$ *μm room-temperature continuous-wave quantum-cascade lasers"*. Appl. Phys. Lett. 88, 251118 (2006).

[113] L. Diehl, D. Bour, S. Corzine, J. Zhu, G. Höfler, M. Lončar, M. Troccoli, and F. Capasso, *"High-temperature continuous wave operation of strain-balanced quantum cascade lasers grown by metal organic vapor-phase epitaxy"*. Appl. Phys. Lett. 89, 081101 (2006).

[114] L. Diehl, D. Bour, S. Corzine, J. Zhu, G. Höfler, B. G. Lee, C. Y. Wang, M. Troccoli, and F. Capasso, *"Pulsed-and continuous-mode operation at high temperature of strained quantum-cascade lasers grown by metalorganic vapor phase epitaxy"*. Appl. Phys. Lett. 88, 041102 (2006).

[115] A. Evans, J. Nguyen, S. Slivken, J. S. Yu, S. R. Darvish, and M. Razeghi, *"Quantum-cascade lasers operating in continuous-wave mode above* $90\ ^{\circ}C$ *at* $\lambda \sim 5.25$ *μm"*. Appl. Phys. Lett. 88, 051105 (2006).

[116] A. Evans, S. R. Darvish, S. Slivken, J. Nguyen, Y. Bai, and M. Razeghi, *"Buried heterostructure quantum cascade lasers with high continuous-wave wall plug efficiency"*. Appl. Phys. Lett. 91, 071101 (2007).

[117] A. Lyakh, C. Pflügl, L. Diehl, Q. J. Wang, F. Capasso, X. J. Wang, J. Y. Fan, T. Tanbun-Ek, R. Maulini, A. Tsekoun, R. Go, and C. Kumar N. Patel, *"1.6 W high wall plug efficiency, continuous-wave room temperature quantum cascade laser emitting at 4.6 μm"*. Appl. Phys. Lett. 92, 111110 (2008).

[118] Y. Bai, S. Slivken, S. R. Darvish, and M. Razeghi, *"Room temperature continuous wave operation of quantum cascade lasers with* 12.5% *wall plug efficiency"*. Appl. Phys. Lett. 93, 021103 (2008).

[119] A. Wittmann, T. Gresch, E. Gini, L. Hvozdara, N. Hoyler, M. Giovannini, and J. Faist, *"High-performance bound-to-continuum quantum-cascade lasers for broad-gain applications"*. IEEE J. of Quantum Elect. 44-1, 36 (2008).

[120] J. C. Shin, M. D'Souza, Z. Liu, J. Kirch, L. J. Mawst, D. Botez, I. Vurgaftman, and J. R. Meyer, *"Highly temperature insensitive, deep-well 4.8 μm emitting quantum cascade semiconductor lasers"*. Appl. Phys. Lett. 94, 201103 (2009).

[121] A. Lyakh, R. Maulini, A. Tsekoun, R. Go, C. Pflügl, L. Diehl, Q. J. Wang, F. Capasso, and C. Kumar N. Patel, *"3 W continuous-wave room temperature single-facet emission from quantum cascade lasers based on nonresonant extraction design approach"*. Appl. Phys. Lett. 95, 141113 (2009).

[122] T. Gresch, J. Faist, and M. Giovannini, *"Gain measurements in strain-compensated quantum cascade laser"*. Appl. Phys. Lett. 94, 161114 (2009).

[123] Y. Bai, S. Slivken, S. Kuboya, S. R. Darvish, and M. Razeghi, *"Quantum cascade lasers that emit more light than heat"*. Nature 4, 99 (2010).

[124] Y. Bai, N. Bandyopadhyay, S. Tsao, S. Slivken, and M. Razeghi, *"Room temperature quantm cascade lasrs with* 27% *wall plug efficiency"*. Appl. Phys. Lett. 98, 181102 (2011).

[125] E. Träger (Ed.), *"Handbook of Lasers and Optics"*. Springer Verlag, (2007).

[126] D. Meschede, *"Optik, Licht und Laser"*. Vieweg + Teubner, Wiesbaden (2008).

[127] C. Sirtori, P. Kruck, S. Barbieri, P. Collot, J. Nagle, M. Beck, J. Faist, and U. Oesterle, *"GaAs/$Al_xGa_{1-x}As$ quantum cascade lasers"*. Appl. Phys. Lett. 73, 3486 (1998).

[128] C. Sirtori, P. Kruck, S. Barbieri, H. Page, J. Nagle, M. Beck, J. Faist, and U. Oesterle, *"Low-loss Al-free waveguides for unipolar semiconductor lasers"*. Appl. Phys. Lett. 75, 3911 (1999).

[129] C. A. Evans, contribution in *"Quantum Wells, Wires and Dots"*. 3rd Edition, Wiley, Chichester (2009).

[130] B. E. A. Saleh and M. C. Teich, *"Fundamentals of Photonics"*. John Wiley & Sons, New York (1991).

[131] L. Diehl, D. Bour, S. Corzine, J. Zhu, G. Höfler, M. Lončar, M. Troccoli, and F. Capasso, *"High-power quantum cascade lasers grown by low-pressure metal organic vapor-phase epitaxy operating in continuous wave above 400 K*. Appl. Phys. Lett. 88, 201115 (2006).

[132] Q. K. Yang, C. Mann, F. Fuchs, R. Kiefer, K. Köhler, N. Rollbühler, H. Schneider, and J. Wagner, *"Improvement of* $\lambda \approx 5$ *μm quantum cascade lasers by blocking barriers in the active regions"*. Appl. Phys. Lett. 80, 2048 (2002).

[133] Y. Bai, N. Bandyopadhyay, S. Tsao, E. Selcuk, S. Slivken, and M. Razeghi, *"Highly temperature insensitive quantum cascade lasers"*. Appl. Phys. Lett. 97, 251104 (2010).

[134] M. Beck, D. Hofstetter, T. Aellen, J. Faist, U. Oesterle, M. Ilegems, E. Gini, and H. Melchior, *"Continuous wave operation of a mid-infrared semiconductor laser at room temperature"*. Science 295, 301 (2002).

[135] H. K. Lee and J. S. Yu, *"Thermal analysis of short wavelength InGaAs/InAlAs quantum cascade lasers"*. Sol. Stat. Elect. 54, 769 (2010).

[136] S. Slivken, J. S. Yu, A. Evans, J. David, L. Doris, and M. Razeghi, *"Ridge-width dependence on high-temperature continuous-wave quantum-cascade laser operation"*. IEEE Photon. Technol. Lett. 16, 744 (2004).

[137] D. Hofstetter, M. Beck, T. Aellen, J. Faist, U. Oesterle, M. Ilegems, E. Gini, and H. Melchior, *"Continuous wave operation of a 9.3 μm quantum cascade laser on a Peltier cooler"*. Appl. Phys. Lett. 78, 1964 (2001).

[138] B. Ishaug, W.-Y. Hwang, J. Um, B. Guo, H. Lee, abd C.-H. Lin, *"Continuous-wave operation of a 5.2 μm quantum-cascade laser up to 210 K*. Appl. Phys. Lett. 79, 1745 (2001).

[139] J. S. Yu, S. Slivken, A. Evans, J. David, and M. Razeghi, *"Very high average power at room temperature for* $\lambda \approx 3.9$*-μm quantum-cascade lasers"*. Appl. Phys. Lett. 82, 3397 (2003).

[140] J. S. Yu, S. Slivken, A. Evans, L. Doris, and M. Razeghi, *"High-power continuous-wave operation of a 6 μm quantum-cascade laser at room temperature"*. Appl. Phys. Lett. 82, 3397 (2003).

[141] A. Evans, J. S. Yu, J. David, L. Doris, M. Mi, S. Slivken, and M. Razeghi, *"High-temperature, high-power, continuous-wave operation of buried heterostructure quantum-cascade lasers"*. Appl. Phys. Lett. 84, 314 (2004).

[142] A. Evans, J. S. Yu, S. Slivken, and M. Razeghi, *"Continuous-wave operation of* $\lambda \sim 4.8$ *μm quantum-cascade lasers at room temperature"*. Appl. Phys. Lett. 85, 2166 (2004).

[143] Z. Liu, D. Wasserman, S. S: Howard, A. J. Hoffman, C. F. Gmachl, X. Wang, T. Tanbun-Ek, L. Cheng, and F.-S. Choa, *"Room-temperature continuous-wave quantum cascade lasers grown by MOCVD without lateral regrowth"*. IEEE Phot. Tech. Lett. 18, 1347 (2006).

[144] Y. Bai, S. R. Darvish, S. Slivken, W. Zhang, A. Evans, J. Nguyen, and M. Razeghi, *"Room temperature continuous wave operation of quantum cascade lasers with watt-level optical power"*. Appl. Phys. Lett. 92, 101105 (2008).

[145] D. Botez, *"Comment on "Highly temperature insensitive quantum cascade lasers"*. Appl. Phys. Lett. 98, 216101 (2011).

[146] J. H. Smet, C. G. Fonstad, and Q. Hu, *"Intrawell and interwell intersubband transitions in multiple quantum wells for far-infrared sources"*. J. of Appl. Phys. 79, 9305 (1996).

[147] R. Ferreira and G. Bastard, *"Evaluation of some scattering times for electrons in unbiased and biased single- and multiple-quantum-well structures"*. Phys. Rev. B 40, 1074 (1989).

[148] P. J. Price, *"Two-dimensional electron transport in semiconductor layers: Phonon scattering"*. Ann. of Phys. 133, 217 (1981).

[149] M. Stroscio and M. Dutte, *"Phonons in Nanostructures"*. Cambridge University Press, UK (2001).

[150] X. Gao, D. Botez, and I. Knezevic, *"Phonon confinement and electron transport in GaAs-based quantum cascade structures"*. J. Appl. Phys. 103, 073101 (2008).

[151] M. Lundstrom, *"Fundamentals of Carrier Transport"*. Addison-Wesley, Wokingham (1990).

[152] J. B. Khurgin, Y. Dikmelik, P. Q. Liu, A. J. Hoffman, M. D. Escarra, K. J. Franz, and C. F. Gmachl, *"Role of interface roughness in the transport and lasing characteristics of quantum-cascade lasers"*. Appl. Phys. Lett. 94, 091101 (2009).

[153] Y. T. Chiu, Y. Dikmelik, P. Q. Liu, N. L. Aung, J. B. Khurgin, and C. F. Gmachl, *"Importance of interface roughness induced intersubband scattering in mid-infrared quantum cascade lasers"*. Appl. Phys. Lett. 101, 171117 (2012).

[154] P. Harrison and R. W. Kelsall, *"The relative importance of electron-electron and electron-phonon scattering in terahertz quantum cascade lasers"*. Sol. Stat. Elect. 42, 1449 (1998).

[155] R. Nelander, *"Lineshape in quantum cascade lasers: Temperature, screening and broadening"*. Ph. D. Thesis, Lund University (2009).

[156] J. Faist, F. Capasso, C. Sirtori, D. L. Sivco, A. L. Hutchinson, S. N. G. Chu, and A. Y. Cho, *"Narrowing of the intersubband electroluminescent spectrum in coupled-quantum-well heterostructures"*. Appl. Phys. Lett. 65, 94 (1994).

[157] R. Nelander and A. Wacker, *"Temperature dependence and screening models in quantum cascade structures"*. J. Appl. Phys. 106, 063115 (2009).

[158] S. Tsujino, A. Borak, E. Müller, M. Scheinert, C. V. Falub, H. Sigg, D. Grützmacher, M. Giovannini, and J. Faist, *"Interface-roughness-induced broadening of intersubband electroluminescence in p-SiGe and n-GaInAs/AlInAs quantum-cascade structures"*. Appl. Phys. Lett. 86, 062113 (2005).

[159] A. Wittmann, Y. Bonetti, J. Faist, E. Gini, and M. Giovannini, *"Intersubband linewidths in quantum cascade laser designs"*, Appl. Phys. Lett. 93, 141103 (2008).

[160] H.C. Liu, A. G. Steele, M. Buchanan, and Z. R. Wasilewski, *"Dark current in quantum well infrared photodetectors"*. J. Appl. Phys. 73, 2029 (1993).

[161] M. Ziegler, *"Charakterisierung und Eigenschaften von $In_xGa_{1-x}As - In_yAl_{1-y}As$ Quantenkaskadenlasern"*. Diplom thesis. Humboldt-Universität zu Berlin, (2004).

[162] J. Faist, *"Quantum Cascade Lasers"*. Oxford University Press (2013).

[163] J. Faist, F. Capasso, D. L. Sivco, A. L. Hutchinson, C. Sirtori, S. N. G. Chu, and A. Y. Cho, *"Quantum cascade laser: Temperature dependence of the performance characteristics and high T_0 operation*. Appl. Phys. Lett. 65, 2901 (1994).

[164] J. Faist, F. Capasso, C. Sirtori, D. L. Sivco, A. L. Hutchinson and A. Y. Cho, *"Vertical transition quantum cascade laser with Bragg confined excited state"*. Appl. Phys. Lett. 66, 538 (1995).

[165] J. Faist, F. Capasso, C. Sirtori, D. L. Sivco, J. N. Baillargeon, A. L. Hutchinson, S.-N. G. Chu, and A. Y. Cho, *"High power mid-infrared ($\lambda \sim 5$ μm) quantum cascade lasers operating above room temperature"*. Appl. Phys. Lett. 68, 3680 (1996).

[166] J. Faist, F. Capasso, D. L. Sivco, A. L. Hutchinson, S-N. G. Chu, and A. Y. Cho, *"Short wavelength ($\lambda \sim 3.4$ μm) quantum cascade laser based on strained compensated InGaAs/AlInAs"*. Appl. Phys. Lett. 72, 680 (1998).

[167] L. Schrottke, M. Wienold, M. Giehler, R. Hey, and H. T. Grahn, *"Analysis of the slope efficiency for terahertz quantum-cascade lasers"*, J. of Appl. Phys. 108, 103108 (2010).

List of Figures